

RHODIUM(0) NANOPARTICLES SUPPORTED ON NANO OXIDE
CRYSTALLINE MATERIALS: PREPARATION, CHARACTERIZATION AND
CATALYTIC USE IN HYDROGEN GENERATION FROM THE
METHANOLYSIS OF AMMONIA BORANE

A THESIS SUBMITTED TO
THE GRADUATE SCHOOL OF NATURAL AND APPLIED SCIENCES
OF
MIDDLE EAST TECHNICAL UNIVERSITY

BY

DERYA ÖZHAVA

IN PARTIAL FULFILLMENT OF THE REQUIREMENTS
FOR
THE DEGREE OF DOCTOR OF PHILOSOPHY
IN
CHEMISTRY

JULY 2018

Approval of the thesis:

**RHODIUM(0) NANOPARTICLES SUPPORTED ON NANO OXIDE
CRYSTALLINE MATERIALS: PREPARATION, CHARACTERIZATION
AND CATALYTIC USE IN HYDROGEN GENERATION FROM THE
METHANOLYSIS OF AMMONIA BORANE**

submitted by **DERYA ÖZHAVA** in partial fulfillment of the requirements for the degree of **Doctor of Philosophy in Chemistry Department, Middle East Technical University** by,

Prof. Dr. Halil Kalıpçılar
Dean, Graduate School of **Natural and Applied Sciences**

Prof. Dr. Cihangir Tanyeli
Head of Department, **Chemistry**

Prof. Dr. Saim Özkar
Supervisor, **Chemistry Dept., METU**

Examining Committee Members:

Prof. Dr. Ahmet M. Önal
Chemistry Dept., METU

Prof. Dr. Saim Özkar
Chemistry Dept., METU

Prof. Dr. Birgül Zümreoğlu Karan
Chemistry Dept., Hacettepe University

Assoc. Prof. Dr. Emren Nalbant Esentürk
Chemistry Dept., METU

Assoc. Prof. Dr. Önder Metin
Chemistry Dept., Atatürk University

Date: 09.07.2018

I hereby declare that all information in this document has been obtained and presented in accordance with academic rules and ethical conduct. I also declare that, as required by these rules and conduct, I have fully cited and referenced all material and results that are not original to this work.

Name, Last name: Derya Özhava

Signature:

ABSTRACT

RHODIUM(0) NANOPARTICLES SUPPORTED ON NANO OXIDE CRYSTALLINE MATERIALS: PREPARATION, CHARACTERIZATION AND CATALYTIC USE IN HYDROGEN GENERATION FROM THE METHANOLYSIS OF AMMONIA BORANE

Özhava, Derya
Ph.D., Department of Chemistry
Supervisor: Prof. Dr. Saim Özkar

July 2018, 144 pages

Ammonia borane (AB) has been considered as a chemical hydrogen storage materials, because of its high hydrogen storage capacity (19.6 wt%), nontoxicity, and stability under ordinary conditions. Hydrogen stored in AB can be liberated by thermolysis or solvolysis. Hydrolysis and methanolysis are the two solvolysis reactions producing hydrogen gas from AB. Although the hydrolysis of AB has been investigated for years extensively, the methanolysis of AB has been considered as an alternative way of releasing hydrogen gas due to many advantages over hydrolysis. As for the hydrolysis, the hydrogen liberation from the methanolysis of AB also realized in the presence of a suitable catalyst. This dissertation covers the preparation and characterization of rhodium(0) nanoparticles supported on the surface of nanooxide materials (Rh(0)/nanooxides), namely hydroxyapatite, silica, alumina and ceria, as well as the examination of their catalytic activities in hydrogen generation from the methanolysis of AB. Firstly, Rh(0)/nanooxides were prepared in a simple and reproducible way by impregnating rhodium(III) or (II) ions on the surface of nanooxide followed by their reduction during the methanolysis of AB. They were then isolated from the reaction medium and characterized by using a combination of advance analytical techniques including ATR-IR, PXRD, TEM, HR-TEM, TEM – EDX, STEM-EDS, XPS, SEM, SEM-EDX, ICP-OES and N₂ adsorption/desorption. Then, the kinetics of methanolysis of AB in the presence of Rh(0)/nanooxides were examined depending on catalyst concentration and temperature as well as catalytic lifetime, and heterogeneity tests were performed. Furthermore, the formation kinetics

of rhodium(0) nanoparticles supported on nanosilica, nanoalumina or nanocerium during hydrogen generation from methanolysis of AB were investigated by using the hydrogen generation as reporter reaction.

Keywords: Rhodium(0) nanoparticles; Oxide supports; Methanolysis; Ammonia borane; Hydrogen generation.

ÖZ

NANO OKSİT KRİSTAL MALZEMELER ÜZERİNDE DESTEKLENDİRİLMİŞ RODYUM(0) NANOPARÇACIKLARI; HAZIRLANMASI, TANIMLANMASI VE AMONYAK BORANIN METANOLİZİNDEN HİDROJEN ÜRETİMİNDE KATALİTİK KULLANIMI

Özhava, Derya
Doktora, Kimya Bölümü
Tez Yöneticisi: Prof. Dr. Saim Özkar

Temmuz 2018, 144 sayfa

Amonyak boran, yüksek hidrojen depolama kapasitesi (%19.6), toksik olmaması ve normal koşullar altında yüksek kararlılığa sahip olması nedeniyle kimyasal hidrojen depolama malzemesi olarak düşünülmektedir. AB'in içerdiği hidrojen termoliz ve solvoliz yöntemleri ile salınabilir. Hidroliz ve metanoliz AB'dan hidrojen gazı üreten iki solvoliz tepkimesidir. AB'in hidrolizi yıllardır yoğun olarak araştırılmasına rağmen, AB'in metanolizi, hidrolizden daha fazla avantajlara sahip olması sebebiyle hidrojen gazı salınımı için alternatif bir yol olarak düşünülebilir. Hidroliz de olduğu gibi, AB'in metanolizinden hidrojen üretimi de ancak uygun bir katalizör varlığında gerçekleşebilir. Bu tez, nano boyutta oksit malzemelerin, örneğin hidroksiapatit, silika, alumina ve serya, yüzeyinde desteklendirilmiş rodyum(0) nanoparçacıklarının (Rh(0)/nanooksit) hazırlanmasını, tanımlanmasını ve ayrıca AB'in metanolizinden hidrojen üretiminde katalitik aktifliklerinin sınanmasını kapsamaktadır. İlk olarak, Rh(0)/nanooksitler basit ve tekrar üretilebilir yolla rodyum (III) ya da (II) iyonlarının nanooksitlerin yüzeyine tutturulmasını takiben AB'in metanolizinden hidrojen üretimi sırasında indirgenerek hazırlandı. Daha sonra, tepkime ortamından izole edildiler ve ATR-IR, PXRD, TEM, HR-TEM, TEM – EDX, STEM-EDS, XPS, SEM, SEM-EDX, ICP-OES ve N₂ adsorplama-desorplama gibi ileri analitik teknikler ile tanımlandılar. Sonrasında, Rh(0)/nanooksit varlığında AB'in metanoliz kinetiği katalizör derişimine ve sıcaklığa bağlı olarak incelendi, yanı sıra katalizör ömrü ve heterojenlik testleri çalışıldı. Ayrıca, AB'in

metanolizinden hidrojen üretimi sırasında nanosilika, nanoalumina ya da nanoserya yüzeyinde desteklendirilmiş rodyum(0) nanoparçacıklarının oluşum kinetiği hidrojen üretim tepkimesi kullanılarak incelendi.

Anahtar kelimeler: Rodyum(0) nanoparçacıkları; Oksit destekler; Metanoliz; Amonyak boran; Hidrojen Üretimi

To my family,

ACKNOWLEDGEMENT

I would like to express my sincere thanks to Prof. Dr. Saim Özkar for his priceless support, guidance and encouragement during my graduate studies and in the completion of this dissertation. I am deeply honored to have a chance to work with him, and to be alumni of his highly respected research group.

I would like to thank to my thesis monitoring committee members; Prof. Dr. Birgül Karan and Assoc. Prof. Dr. Emren Nalbant Esentürk for their valuable advices and comments.

I would like to also thank to Cemile Bektaş, Asude Çetin, Duygu Tan, Eda Durkan for their valuable friendship, comprehension, advice, and supports.

I would like to thank to my friends Pınar Mercan and Tuğba Lekesiz for their valuable friendship, advice, supports during my PhD adventure.

I would like to express my thanks to my labmate Serdar .Akbayrak for his friendship.

I would like to thank to Prof. Dr. Ayşen Yılmaz and her research group members, Assoc. Prof. Dr. Önder Metin and Central Laboratory of METU for their helps and comments during characterization period of my samples.

I would like to thank to TUBITAK for 2211- National Scholarship Programme for PhD Students and METU for BAP projects.

The last but not the least, my special appreciation and great gratitude is devoted to my dear family for their endless moral support and my husband Güven and my little angel Deren for their love, patience, moral support, joy and encouragement in every moment of my life. Without their help these all would not be possible.

TABLE OF CONTENTS

ABSTRACT	v
ÖZ	vii
ACKNOWLEDGEMENT	x
TABLE OF CONTENTS	xi
LIST OF TABLES	xvi
LIST OF FIGURES	xviii
LIST OF ABBREVIATIONS	xxiv
CHAPTERS	
1. INTRODUCTION	1
2. CATALYSIS	9
2.1. General Principles of Catalysis	9
2.2. What is nano-catalysis?	13
3. TRANSITION METAL(0) NANOPARTICLES IN CATALYSIS	15
3.1. General Introduction	15
3.2. Stabilization Modes for Metal(0) Nanoparticles	17
3.2.1. Electrostatic / DLVO-type Stabilization	18
3.2.2. Steric Stabilization	19
3.2.3. Electrosteric / Combination of DLVO Type Electrostatic and Steric Stabilization	20
3.3. Synthesis Methods of Transition Metal(0) Nanoparticles	21
3.4. Characterization of Transition Metal(0) Nanoparticles	22
3.5. Scope of the Dissertation	23
4. EXPERIMENTAL	25
4.1. Materials	25
4.2. Instrumentation	25
4.3. <i>In-situ</i> Preparation and Catalytic Activity of Rhodium(0) Nanoparticles Supported on Hydroxyapatite Nanospheres	26

4.3.1. Preparation of Rh(III)–exchanged hydroxyapatite nanospheres (Rh(III)/nanoHAP)	26
4.3.2. <i>In situ</i> Formation of Rhodium(0) Nanoparticles Supported on Hydroxyapatite Nanospheres and Concomitant Catalytic Methanolysis of Ammonia Borane	27
4.3.3. Effect of Tetrabutylammonium Dihydrogen Phosphate Concentration on Catalytic Activity of Rhodium(0) Nanoparticles Supported on Hydroxyapatite Nanospheres	29
4.3.4. Kinetic Experiments and Determination of Activation Parameters for Methanolysis of Ammonia Borane Catalyzed by Rhodium(0) Nanoparticles Supported on Hydroxyapatite Nanospheres	29
4.3.5. Recyclability Test of Rhodium(0) Nanoparticles Supported on Hydroxyapatite Nanospheres in the Methanolysis of Ammonia Borane.	30
4.3.6. Leaching Test of Rhodium(0) Nanoparticles Supported on Hydroxyapatite Nanospheres in the Methanolysis of Ammonia Borane.	30
4.3.7. Heterogeneity Test for Rhodium(0) Nanoparticles Supported on Hydroxyapatite Nanospheres by Carbon Disulfide Poisoning in the Methanolysis of Ammonia Borane.	30
4.4. <i>In situ</i> Preparation and Catalytic Activity of Rhodium(0) Nanoparticles Stabilized on Nanosilica or Nanoalumina or Nanoceria	31
4.4.1. <i>In Situ</i> Preparation of Rh(II)–Ion Impregnated on Nanosilica or Nanoalumina or Nanoceria Surface	31
4.4.2. <i>In situ</i> Formation of Rhodium(0) Nanoparticles Stabilized on Nanosilica or Nanoalumina or Nanoceria and Catalytic Methanolysis of Ammonia Borane	31
4.4.3. Kinetic Experiments and Determination of Activation Parameters for Methanolysis of Ammonia Borane Catalyzed by Rhodium(0) Nanoparticles Stabilized on Nanosilica, Nanoalumina or Nanoceria	32
4.4.4. Catalytic Lifetime of Rhodium(0) Nanoparticles Stabilized on Nanosilica, Nanoalumina or Nanoceria in the Methanolysis of Ammonia Borane	32

4.4.5. Heterogeneity test for Rhodium(0) Nanoparticles Stabilized on Nanosilica or Nanoalumina by Carbon Disulfide Poisoning in the Methanolysis of Ammonia Borane	33
4.4.6. Leaching test for Rhodium(0) Nanoparticles Stabilized on Nanosilica, Nanoalumina or Nanoceria	33
5. RESULTS AND DISCUSSIONS	35
5.1. Preparation and Characterization of Rhodium(0) Nanoparticles Supported on Hydroxyapatite Nanospheres and Further Stabilized by Dihydrogen Phosphate Ion and Investigation of Their Catalytic Activities in Hydrogen Generation From the Methanolysis of Ammonia Borane	35
5.1.1. Preparation and Characterization of Rhodium(0) Nanoparticles Supported on Hydroxyapatite Nanospheres and Further Stabilized by Dihydrogen Phosphate Ion	36
5.1.2. The Catalytic Activities of Rhodium(0) Nanoparticles Supported on Hydroxyapatite Nanospheres and Further Stabilized by Dihydrogen Phosphate Ion in Hydrogen Generation From the Methanolysis of Ammonia Borane	44
5.1.2.1. Kinetic Studies and Determination of Activation Parameters for the Methanolysis of Ammonia Borane Catalyzed by Rhodium(0) Nanoparticles Supported on Hydroxyapatite Nanospheres and Further Stabilized by Dihydrogen Phosphate Ion	44
5.1.2.2. Catalytic Lifetime and Recyclability Test of Rhodium(0) Nanoparticles Supported on Hydroxyapatite Nanospheres and Further Stabilized by Dihydrogen Phosphate Ions in Hydrogen Generation From the Methanolysis of Ammonia Borane	51
5.1.2.3. Leaching Test for Rhodium(0) Nanoparticles Supported on Hydroxyapatite Nanospheres and Further Stabilized by Dihydrogen Phosphate Ions in the Methanolysis of Ammonia Borane	53
5.1.2.4. Carbon Disulfide (CS ₂) Poisoning Heterogeneity Test for Rhodium(0) Nanoparticles Supported on Hydroxyapatite Nanospheres and Further Stabilized by Dihydrogen Phosphate Ions in the Methanolysis of Ammonia Borane	54

5.2. Preparation and Characterization of Rhodium(0) Nanoparticles Supported on Nanosilica and Investigation of Their Catalytic Activities in Hydrogen Generation From the Methanolysis of Ammonia Borane	56
5.2.1. Preparation and Characterization of Rhodium(0) Nanoparticles Supported on Nanosilica.....	56
5.2.2. The Catalytic Activities of Rhodium(0) Nanoparticles Supported on Nanosilica in Hydrogen Generation From the Methanolysis of Ammonia Borane	62
5.2.2.1. Kinetic Studies and Determination of Activation Parameters for the Methanolysis of Ammonia Borane Catalyzed by Rhodium(0) Nanoparticles Supported on Nanosilica	62
5.2.2.2. Catalytic Lifetime of Rhodium(0) Nanoparticles Supported on Nanosilica in Hydrogen Generation From the Methanolysis of Ammonia Borane	76
5.2.2.3. Leaching Test for Rhodium(0) Nanoparticles Supported on Nanosilica in the Methanolysis of Ammonia Borane	77
5.2.2.4. Carbon Disulfide (CS ₂) Poisoning Heterogeneity Test for Rhodium(0) Nanoparticles Supported on Nanosilica in the Methanolysis of Ammonia Borane	78
5.2.2.5. Establishment of that Rhodium(0) Nanoparticles Supported on Nanosilica Catalyzed Methanolysis of Ammonia Borane is in the Kinetic Regime	79
5.3. Preparation and Characterization of Rhodium(0) Nanoparticles Supported on Nanoalumina and Investigation of Their Catalytic Activities in Hydrogen Generation from Methanolysis of Ammonia Borane.....	81
5.3.1. Preparation and Characterization of Rhodium(0) Nanoparticles Supported on Nanoalumina	81
5.3.2. The Catalytic Activities of Rhodium(0) Nanoparticles Supported on Nanoalumina in Hydrogen Generation from the Methanolysis of Ammonia Borane	90

5.3.2.1. Kinetic Studies and Determination of Activation Parameters for Methanolysis of Ammonia Borane Catalyzed by Rhodium(0) Nanoparticles Supported on Nanoalumina.....	90
5.3.2.2. Catalytic Lifetime of Rhodium(0) Nanoparticles Supported on Nanoalumina in Hydrogen Generation From the Methanolysis of Ammonia Borane	100
5.3.2.3. Leaching Test for Rhodium(0) Nanoparticles Supported on Nanoalumina in the Methanolysis of Ammonia Borane.....	101
5.3.2.4. Carbon Disulfide (CS ₂) Poisoning Heterogeneity Test for Rhodium(0) Nanoparticles Supported on Nanoalumina in the Methanolysis of Ammonia Borane	102
5.4. Preparation and Characterization of Rhodium(0) Nanoparticles Supported on Nanoceria and Investigation of Their Catalytic Activities in Hydrogen Generation From the Methanolysis of Ammonia Borane.....	104
5.4.1. Preparation and Characterization of Rhodium(0) Nanoparticles Supported on Nanoceria	104
5.4.2. The Catalytic Activities of Rhodium(0) Nanoparticles Supported on Nanoceria in Hydrogen Generation From the Methanolysis of Ammonia Borane	113
5.4.2.1. Kinetic Studies and Determination of Activation Parameters for the Methanolysis of Ammonia Borane Catalyzed by Rhodium(0) Nanoparticles Supported on Nanoceria.....	113
5.4.2.2. Catalytic Lifetime of Rhodium(0) Nanoparticles Supported on Nanoceria in Hydrogen Generation From the Methanolysis of Ammonia Borane	120
5.4.2.3. Leaching Test for Rhodium(0) Nanoparticles Supported on Nanoceria in the Methanolysis of Ammonia Borane	121
6. CONCLUSIONS.....	123
REFERENCES.....	130

LIST OF TABLES

TABLES

- Table 1.** The rate constants k_1 of the slow, continuous nucleation, $P \rightarrow Q$, and k_2 of the autocatalytic surface growth, $P + Q \rightarrow 2Q$, for the formation of rhodium(0) nanoparticles catalyst from the reduction of rhodium(II) ions during the methanolysis of AB (200 mM) starting with Rh(II)/nanoSiO₂ with different rhodium loading, rhodium concentrations, hydrogen generation rates, turnover frequency (TOF) values, and the TOF values corrected for the number of rhodium atoms on the surface of nanoparticles for the methanolysis of AB at 25.0 ± 0.5 °C..... 69
- Table 2.** The rate constants k_1 of the slow, continuous nucleation, $P \rightarrow Q$, and k_2 of the autocatalytic surface growth, $P + Q \rightarrow 2Q$, for the formation of rhodium(0) nanoparticles catalyst from the reduction of rhodium(II) ions during the methanolysis of AB, hydrogen generation rates, k_{obs} values, turnover frequency (TOF) values, and the TOF values corrected for the number of rhodium atoms on the surface of nanoparticles for the methanolysis of AB starting with [AB] = 200 mM and [Rh] = 0.49 mM at different temperatures..... 75
- Table 3.** The rate constants k_1 of the slow, continuous nucleation, $P \rightarrow Q$, and k_2 of the autocatalytic surface growth, $P + Q \rightarrow 2Q$, for the formation of rhodium(0) nanoparticles catalyst from the reduction of rhodium(II) ions during the methanolysis of AB (200 mM) starting with Rh(II)/nanoAl₂O₃ with different rhodium loading, rhodium concentrations, hydrogen generation rates, turnover frequency (TOF) values, and the TOF values corrected for the number of rhodium atoms on the surface of nanoparticles for the methanolysis of AB at 25.0 ± 0.5 °C..... 95
- Table 4.** The rate constants k_1 of the slow, continuous nucleation, $P \rightarrow Q$, and k_2 of the autocatalytic surface growth, $P + Q \rightarrow 2Q$, for the formation of rhodium(0) nanoparticles catalyst from the reduction of rhodium(II) ions during the methanolysis of AB, hydrogen generation rates, k_{obs} values, turnover frequency (TOF) values, and the TOF values corrected for the number of rhodium atoms on the surface of

nanoparticles for the methanolysis of AB starting with $[AB] = 200 \text{ mM}$ and $[Rh] = 0.24 \text{ mM}$ at different temperatures..... 99

Table 5. The rate constants k_1 of the slow, continuous nucleation, $P \rightarrow Q$, and k_2 of the autocatalytic surface growth, $P + Q \rightarrow 2Q$, for the formation of rhodium(0) nanoparticles catalyst from the reduction of rhodium(II) ions during the methanolysis of AB (200 mM) starting with Rh(II)/nanoCeO₂ having different rhodium loading, rhodium concentrations, hydrogen generation rates, turnover frequency (TOF) values at $25.0 \pm 0.5 \text{ }^\circ\text{C}$ 116

Table 6. The rate constants k_1 of the slow, continuous nucleation, $P \rightarrow Q$, and k_2 of the autocatalytic surface growth, $P + Q \rightarrow 2Q$, for the formation of rhodium(0) nanoparticles catalyst from the reduction of rhodium(II) ions during the methanolysis of AB, k_{obs} values for the catalytic methanolysis reaction, activation energies for the nucleation and autocatalytic surface growth steps as well as the methanolysis of AB catalyzed by Rh(0)/nanoCeO₂ having different rhodium concentrations. 119

Table 7. Catalytic activities in TOF and catalyst lifetime of metal(0) catalysts used for the catalytic methanolysis of AB and activation energies of catalytic methanolysis of AB..... 129

LIST OF FIGURES

FIGURES

Figure 1. Hydrogen economy as a network of primary energy sources linked to different end-uses through hydrogen as an energy carrier [2] .	3
Figure 2. Hydrogen mass density vs. Hydrogen volume density for hydrogen storage materials [10].	4
Figure 3. Bond polarizations in ammonia borane [19].	4
Figure 4. Ammonia borane regeneration cycle using the methanolysis product [35].	6
Figure 5. Classification of catalysts [55].	10
Figure 6. Mechanism of heterogeneous catalysis [57].	11
Figure 7. Potential energy diagram for both catalyzed and uncatalyzed reaction [57].	12
Figure 8. What is nanocatalyst?	14
Figure 9. Schematic representation of electronic levels in (a) mononuclear complex (b) large cluster (c) bulk metal.	16
Figure 10. Melting point vs. particle size graph for gold nanoparticles [69].	17
Figure 11. Electrostatic stabilization for transition metal nanoparticles and plot of energy versus distance between colloids [71].	19
Figure 12. Schematic image of steric stabilization by adsorption of polymer chains onto a nanoparticle [73].	20
Figure 13. Schematic illustration of electrosteric stabilization of transition metal nanoparticles [74].	21
Figure 14. <i>Top down</i> and <i>bottom up</i> approaches used to obtain nanoparticles	22
Figure 15. Experimental set-up used for determining hydrogen gas generation during reactions and also to study kinetic experiments.	28
Figure 16. ATR-IR spectrum of nanosized hydroxyapatite and Rh(III)/nanoHAP after drying process.	37
Figure 17. Powder X-ray diffraction (PXRD) patterns of (a) hydroxyapatite nanospheres ($[\text{Ca}_5(\text{OH})(\text{PO}_4)_3]_x$), (b) Rh(III)-exchanged hydroxyapatite nanospheres	

(Rh(III)/nanoHAP) and (c) rhodium(0) nanoparticles supported on hydroxyapatite nanospheres (Rh(0)/nanoHAP).	38
Figure 18. (a), (b), (c) TEM images of Rh(0)/nanoHAP in different magnifications (d) corresponding particle size histogram of Rh(0)/nanoHAP	39
Figure 19. TEM-EDX spectrum of rhodium(0) nanoparticles supported on hydroxyapatite nanospheres with a rhodium loading of 2.09 wt %.....	40
Figure 20. a)X-ray photoelectron (XPS) survey scan of Rh(0)/nanoHAP b) XPS high resolution spectra of Rh(0)/nanoHAP for Rh 3d after the methanolysis of AB.	41
Figure 21. High resolution Rh 3d XPS spectrum of Rh(0)/nanoHAP a) before sputtering and b) after sputtering by argon bombardment.	42
Figure 22. Nitrogen adsorption-desorption isotherms of nanoHAP and Rh(0)/nanoHAP.	43
Figure 23. Plots of mol of H ₂ evolved per mole of AB <i>versus</i> time for methanolysis of 200 mM AB starting with 0.609 mM Rh (30.0 mg Rh(III)/nanoHAP, 2.09 wt.%) and with (○) or without (□) [TBAP]/[Rh] ratio of 2.0 in 10.0 mL methanol at 25.0 ± 0.5 °C.	45
Figure 24. Plots of mol H ₂ evolved per mole of AB <i>versus</i> time for the methanolysis of AB starting with 10.0 mL solution containing 200 mM AB (64 mg), 0.609 mM Rh (30.0 mg Rh(III)/nanoHAP, 2.09 wt.%) and [TBAP] / [Rh] in different ratios at 25.0 ± 0.5°C. Inset: Plot of hydrogen generation rate <i>versus</i> [TBAP]/[Rh] ratio for the methanolysis of AB.....	47
Figure 25. Plots of mol H ₂ evolved per mole of AB <i>versus</i> time for the methanolysis of 10.0 mL solution of 200 mM AB in different metal concentrations ([Rh] = 0.203, 0.406, 0.609, 0.812, 1.015 mM) and 2.0 equivalent of TBAP stabilizer per mol of rhodium at 25.0 ± 0.5 °C. Inset: Plot of hydrogen generation rate <i>versus</i> the concentration of rhodium (both in logarithmic scale.).....	48
Figure 26. a) Plots of mol H ₂ evolved per mole of AB <i>versus</i> time for the catalytic methanolysis of AB at various temperatures in the range of 20 – 40 °C keeping the concentration of substrate at [AB] = 200 mM and rhodium at [Rh] = 0.406 mM (20.0 mg Rh(III)/nanoHAP, 2.09 wt.%) as well as the [TBAP] / [Rh] ratio at 2.0 constant in 10.0 mL methanol. b) Arrhenius Plot c) Eyring Plot.	50
Figure 27. Plot of total turnover number (TTO) or turnover frequency <i>versus</i> time for the methanolysis of AB with 10.0 mL solution of 5.5 mg Rh(III)/nanoHAP	

(rhodium loading of 2.09 wt. %, 1.1 $\mu\text{mol Rh}$), 400 mM AB (for each run) plus [TBAP]/[Rh] ratio at 2.0	52
Figure 28. Catalytic activity and conversion of AB <i>versus</i> number of catalytic runs for Rh(0)/nanoHAP catalyst (38.5 mg Rh(0)/nanoHAP, 2.09 wt.% , [Rh] = 0.782 mM, [AB] = 200 mM at 25.0 ± 0.5 °C.)	53
Figure 29. Plots of mol of H ₂ evolved per mole of AB <i>versus</i> time for the methanolysis of 200 mM AB catalyzed by 0.406 mM Rh (20.0 mg Rh(III)/nanoHAP, 2.09 wt.%) plus [TBAP] / [Rh] ratio of 2.0 with (square \square) or without (circle, \ominus) addition of CS ₂ in 10.0 mL methanol, and the filtrate solution obtained from the filtration of active catalyst after the methanolysis of AB at 25.0 ± 0.5 °C. (triangle Δ)	55
Figure 30. Powder X-ray diffraction (PXRD) patterns of a) silica nanopowder (nanoSiO ₂), b) rhodium(0) nanoparticles supported on nanosilica (Rh(0)/nanoSiO ₂) with rhodium loading of 3.0% wt. Rh.	57
Figure 31. TEM images of rhodium(0) nanoparticles supported on nanosilica with different rhodium loading a) 0.5, b) 1.0, c) 2.0, d) 3.0 and e) 5.0% wt. Rh after catalytic methanolysis reaction performed starting with 200 mM AB catalyzed by desired amount of of rhodium(0) nanoparticles supported on nanosilica at 25.0 ± 0.5 °C. f) the plot of percentage rhodium loading <i>versus</i> particle size.	59
Figure 32. TEM-EDX spectrum of Rh(0)/nanoSiO ₂ obtained after the catalytic methanolysis of AB.	60
Figure 33. a) X-ray photoelectron (XPS) survey scan spectrum, a) high resolution Rh 3d XPS spectrum of Rh(0)/nanoSiO ₂ with a rhodium loading of 5.0% wt. Rh....	61
Figure 34. Plot of mol H ₂ evolved per mole of AB <i>versus</i> time for the catalytic methanolysis of AB starting with 200 mM AB and 50 mg of Rh(II)/nanoSiO ₂ (1.0 wt.% Rh, [Rh]= 0.49 mM) in 10 mL methanol at 25.0 ± 0.5 °C.	63
Figure 35. Plots of mol H ₂ evolved per mole of AB <i>versus</i> time for the catalytic methanolysis of AB starting with 200 mM AB plus either (black squares, \square) 50 mg of Rh(II)/nanoSiO ₂ (1.0 wt.% Rh, [Rh] = 0.49 mM) or (red circles, \ominus) 1.9 mg of rhodium(II) octanoate (0.49 mM Rh) in 10 mL methanol at 25.0 ± 0.5 °C.	66
Figure 36. a) Plots of mol H ₂ evolved per mole of AB <i>versus</i> time for methanolysis of 200 mM AB in different metal concentrations ([Rh] = 0.24, 0.49, 0.99, 1.5, 2.5 mM, each prepared using metal loading of 0.50, 1.0, 2.0, 3.0, 5.0% wt. Rh, respectively) at 25.0 ± 0.5 °C. Inset: Plot of hydrogen generation rate <i>versus</i> the	

concentration of rhodium (both in logarithmic scale.). b) Inverse dependence of initial TOF value on the initial precatalyst Rh concentration..... 68

Figure 37. a) Plots of mol H₂ evolved per mole of AB *versus* time for the catalytic methanolysis of AB at various temperatures in the range of 20 – 40 °C keeping the concentration of substrate at [AB] = 200 mM and rhodium at [Rh] = 0.49 mM (1.0 wt. % Rh, 50 mg Rh(0)/nanoSiO₂), b) The Arrhenius plot for nucleation of rhodium(0) nanoparticles, c) The Arrhenius plot for the autocatalytic surface growth of rhodium(0) nanoparticles, d) The Arrhenius plot, e) The Eyring plot for Rh(0)/nanoSiO₂ catalyzed methanolysis of AB. [AB] = 200 mM, [Rh] = 0.49 mM (1.0 wt. % Rh, 50 mg Rh(0)/nanoSiO₂). 73

Figure 38. Plot of total turnover number (TTO) or turnover frequency *versus* time for the methanolysis of AB with 10 mL solution of 0.99 mM Rh (50.0 mg Rh(0)/nanoSiO₂, 2.0 wt.% Rh,) and 400 mM AB (for each run) at 25.0 ± 0.5 °C. ... 77

Figure 39. Plots of mol H₂ evolved per mole of AB *versus* time for the methanolysis of 200 mM AB catalyzed by Rh(0)/nanoSiO₂ (0.49 mM Rh, 1.0 wt. % Rh(0)/nanoSiO₂) with (square, □) and without (circle, ○) addition of 0.2 equiv. CS₂, and (triangle, Δ) the filtrate solution obtained from filtration of active catalyst after methanolysis of AB at 25.0 ± 0.5 °C. 79

Figure 40. Plots of mol H₂ evolved per mole of AB *versus* time for the catalytic methanolysis of AB starting with 200 mM AB and 0.49 mM Rh (50 mg Rh(II)/nanoSiO₂, 1.0 wt.% Rh) in 10 mL methanol at 25.0 ± 0.5 °C at different stirring rate. The inset shows the plot of hydrogen generation rate *versus* the stirring rate..... 80

Figure 41. ATR-IR spectrum of (a) nanoalumina (b) Rh(II)/nanoAl₂O₃ with a rhodium loading of 1.0% wt. Rh..... 83

Figure 42. Powder X-ray diffraction (PXRD) patterns of a) nanoAl₂O₃, b) Rh(0)/nanoAl₂O₃ with rhodium loading of 0.50 % wt. Rh..... 84

Figure 43. TEM images of Rh(0)/nanoAl₂O₃ with different rhodium loading a) 0.5, b) 1.0, c) 1.5, and d) 2.0 wt. % Rh after catalytic methanolysis reaction performed starting with 200 mM AB catalyzed by desired amount of Rh(0)/nanoAl₂O₃ at 25.0 ± 0.5 °C. e) HRTEM images of Rh(0)/nanoAl₂O₃ with rhodium loading of 1.0 wt. % f) the plot of percentage rhodium loading *versus* particle size. 85

Figure 44. a) X-ray photoelectron (XPS) survey scan spectrum, b) high resolution Rh 3d XPS spectrum of Rh(0)/nanoAl₂O₃ with a rhodium loading of 2.0% wt. Rh. 87

Figure 45. a) SEM image of Rh(0)/nanoAl ₂ O ₃ b) SEM-EDX spectrum of Rh(0)/nanoAl ₂ O ₃ with a rhodium loading of 2.0% wt. Rh.	89
Figure 46. Plots of mol H ₂ evolved per mole of AB <i>versus</i> time for the catalytic methanolysis of AB starting with 200 mM AB and 50 mg of Rh(II)/nanoAl ₂ O ₃ (0.50 wt.% Rh, [Rh]= 0.24 mM) in 10 mL methanol at 25.0 ± 0.5 °C. The red curve shows the fit of data to the F-W 2-step mechanism of nanoparticle formation.	91
Figure 47. Plots of mol H ₂ evolved per mole of AB <i>versus</i> time for the catalytic methanolysis of AB starting with 200 mM AB plus either (red circles, ⊙) 50 mg of Rh(II)/nanoAl ₂ O ₃ (1.0 wt.% Rh, [Rh] = 0.49 mM) or (black squares, ⊠) 1.9 mg of rhodium(II) octanoate (0.49 mM Rh) in 10 mL methanol at 25.0 ± 0.5°C.	92
Figure 48. a) Plots of mol H ₂ evolved per mole of AB <i>versus</i> time for methanolysis of 200 mM AB in different metal concentrations ([Rh] = 0.24, 0.49, 0.74 and 0.99 mM, each prepared using metal loading of 0.50, 1.0, 1.5, 2.0% wt. Rh, respectively) at 25.0 ± 0.5 °C. Inset: Plot of hydrogen generation rate <i>versus</i> the concentration of rhodium (both in logarithmic scale.). b) Inverse dependence of initial TOF value on the initial precatalyst Rh concentration.	96
Figure 49. (a) Plots of mol H ₂ evolved per mole of AB <i>versus</i> time for the catalytic methanolysis of AB at various temperatures in the range of 20 – 35 °C keeping the concentration of substrate at [AB] = 200 mM and rhodium at [Rh] = 0.24 mM (0.50 wt. % Rh, 50 mg Rh(0)/nanoAl ₂ O ₃), (b) The Arrhenius plot for nucleation of rhodium(0) nanoparticles, (c) The Arrhenius plot for the autocatalytic surface growth of rhodium(0) nanoparticles, (d) The Arrhenius plot e) The Eyring plot.	98
Figure 50. Plot of total turnover number (TTO) or turnover frequency <i>versus</i> time for the methanolysis of AB with 10 mL solution of 0.24 mM Rh (50.0 mg Rh(0)/nanoAl ₂ O ₃ , 0.50 wt.% Rh,) and 400 mM AB (for each run) at 25.0 ± 0.5 °C.	101
Figure 51. Plots of mol H ₂ evolved per mole of AB <i>versus</i> time for the methanolysis of 200 mM AB catalyzed by Rh(0)/nanoAl ₂ O ₃ (0.24 mM Rh, 0.50 wt. % Rh(0)/nanoAl ₂ O ₃) with (square, ⊠) and without (circle, ⊙) addition of 0.2 equiv. CS ₂ , and (triangle, Δ) the filtrate solution obtained from filtration of active catalyst after methanolysis of AB at 25.0 ± 0.5 °C.	103
Figure 52. Powder X-Ray diffraction patterns of a) nanoCeO ₂ b) Rh(0)/nanoCeO ₂ with rhodium loading of 1.0 % wt. Rh.	106

Figure 53. (a-b) TEM images of Rh(0)/nanoCeO ₂ with a rhodium loading 1.0 wt. % Rh after catalytic methanolysis of 200 mM AB at 25.0 ± 0.5 °C. c) The corresponding histogram of rhodium(0) nanoparticle size distribution. d) STEM-EDS mapping of O, Rh and Ce.....	107
Figure 54. a) X-ray photoelectron (XPS) survey scan spectrum, b) high resolution Rh 3d XPS spectrum of Rh(0)/nanoCeO ₂ with a rhodium loading of 1.0% wt. Rh.	109
Figure 55. High resolution Ce 3d XPS spectrum of a) bare nanoceria, b) nanoceria treated with AB in methanol, and Rh(0)/nanoCeO ₂ with a rhodium loading of c) 1.0% wt. Rh, and d) 4.0 % wt. Rh.wt.....	111
Figure 56. a) SEM image of Rh(0)/nanoCeO ₂ b) SEM-EDX spectrum of Rh(0)/nanoCeO ₂ with a rhodium loading of 1.0% wt. Rh.	112
Figure 57. Plot of mol H ₂ evolved per mole of AB <i>versus</i> time for the catalytic methanolysis of AB starting with 200 mM AB and 50 mg of Rh(II)/nanoCeO ₂ (1.0 wt.% Rh, [Rh]= 0.49 mM) in 10 mL methanol at 25.0 ± 0.5 °C. The red curve shows the fit of data to the F-W 2-step mechanism of nanoparticle formation.	114
Figure 58 . Plots of mol H ₂ evolved per mole of AB <i>versus</i> time for methanolysis of 200 mM AB in different metal concentrations ([Rh] = 0.49, 0.99, 1.5 and 2.0 mM, each prepared using metal loading of 1.0, 2.0, 3.0, 4.0% wt. Rh, respectively) at 25.0 ± 0.5 °C. Inset: Plot of hydrogen generation rate <i>versus</i> the concentration of rhodium (both in logarithmic scale.).	115
Figure 59. Plots of mol H ₂ evolved per mole of AB <i>versus</i> time for the catalytic methanolysis of AB at various temperatures in the range of 20 – 35 °C keeping the concentration of substrate at [AB] = 200 mM and varying the concentration of rhodium a) 1.0 wt. % Rh, [Rh] = 0.49 mM b) 2.0 wt. % Rh, [Rh] = 0.99 mM c) 3.0 wt. % Rh, [Rh]= 1.5 mM, respectively.	118
Figure 60. Plot of total turnover number (TTO) or turnover frequency <i>versus</i> time for the methanolysis of AB with 10 mL solution of 0.49 mM Rh (50.0 mg Rh(0)/nanoCeO ₂ , 1.0 wt.% Rh,) and 200 mM AB (for each run) at 25.0 ± 0.5 °C.	121
Figure 61. Comparison of catalytic activities of rhodium nanoparticles supported on nanooxide crystalline support materials in hydrogen generation from the methanolysis of ammonia borane at 25.0 ± 0.5 °C.....	125

LIST OF ABBREVIATIONS

ATR-IR: Attenuated Total Reflectance - Infrared Spectroscopy

ICP-OES: Inductively Coupled Plasma - Optical Emission Spectroscopy

TEM: Transmission Electron Microscopy

SEM: Scanning Electron Microscopy

EDX: Energy Dispersive X-Ray

XRD: X - Ray Diffraction

XPS: X - Ray Photoelectron Spectroscopy

Uv-vis: Ultraviolet Visible Spectroscopy

nanoHAP: Hydroxyapatite nanospheres

nanoSiO₂ : Nanosilica

nanoAl₂O₃: Nanoalumina

nanoCeO₂: Nanoceria

Rh(III)/nanoHAP: Rh(III) – ions impregnated on Hydroxyapatite Nanospheres

Rh(II)/nanoSiO₂: Rh(II) – ions impregnated on Nanosilica

Rh(II)/nanoAl₂O₃: Rh(II)– ions impregnated on Nanoalumina

Rh(II)/nanoCeO₂: Rh(II)– ions impregnated on Nanoceria

Rh(0)/nanoHAP: Rhodium(0) Nanoparticles Supported on Hydroxyapatite Nanospheres

Rh(0)/nanoSiO₂: Rhodium(0) Nanoparticles Supported on Nanosilica

Rh(0)/nanoAl₂O₃: Rhodium(0) Nanoparticles Supported on Nanoalumina

Rh(0)/nanoCeO₂: Rhodium(0) Nanoparticles Supported on Nanoceria

AB: Ammonia borane

TOF: Turnover Frequency

TON: Turnover Number

E_a^{app} : Apparent Activation Energy

$\Delta H^{\ddagger,app}$: Apparent Activation Enthalpy

$\Delta S^{\ddagger,app}$: Apparent Activation Entropy

ICE: Internal Combustion Engine

CHAPTER 1

INTRODUCTION

From time immemorial, human beings have used firing wood to keep warm and prepare food. Then, a new source of fuel having higher calorific value was discovered, that was coal. After the invention of steam engines in 1780s, coal gained great attention for the production of mechanical power. Late in the 19th century, the internal combustion engine was invented, thus gradual transition from coal to petroleum occurred due to greater efficiency and convenience of petroleum. In many countries, the use of coal decreased, while that of petroleum increased sharply. Briefly, if the chronological time order is drawn, humankind started with wood and has moved to fossil fuels -first to coal, then petroleum and lastly natural gas- in order to supply energy demand of society [1]. However, ongoing utilization of fossil fuels for power generation threatens our energy supply and causes detrimental effects on the environment such as pollution impeding human health and greenhouse gases causing global climate change [2]. In the face of a growing global population and economy, the energy demand is ever rising. In order to fulfil this energy demand while also reducing both consumption of fossil fuels and emission of greenhouse gases, there is an urgent need to supplement energy feed stocks with renewable sources [3,4]. The results obtained from sustained research, development and projects demonstrate that hydrogen as an energy carrier would be an excellent candidate for the new energy system and provide the mean of connection with sustainable energy economy [5]. The idea about the use of hydrogen to obtain everlasting source of energy was even mentioned in the novel of *The Mysterious Island* written by Jules Verne in 1874. In this novel, Cyrus Harding, a main character, says: *"I believe that water will one day be employed as a fuel, that hydrogen and oxygen which constitute it, used singly or together, will furnish an inexhaustible source of heat and light ... Someday the coal rooms of steamers and the tenders of locomotives will, instead of coal, be stored with these two condensed*

gases, which will burn in the furnaces with enormous calorific power. There is, therefore, nothing to fear. As long as the earth is inhabited it will supply the wants of its inhabitants (...) I believe, then, that when the deposits of coal are exhausted we shall heat and warm ourselves with water. Water will be the coal of the future.”

Hydrogen can be referred to as a future fuel and has many advantages making it applicable [6]: (i) Hydrogen is the most abundant and the lightest element in the universe. (ii) It can be generated from many primary energy resources (wind, geothermal, sun, hydropower etc.); one of which can be reachable from anywhere in the world. (iii) It is a renewable fuel. (iv) It can be stored in different forms such as gaseous, liquid or solid state. (v) It is environmentally friendly, nontoxic and clean. (vi) Combustion reaction of it with oxygen produces only water as a by-product. (vii) It can directly be used as a transportation fuel in internal combustion engine.

Unfortunately, although hydrogen appears to be an attractive candidate for the carbon based fuels; it does not occur in nature as the molecule H_2 . Besides, molecular H_2 is very rare in the Earth's atmosphere owing to its light weight and cannot naturally be produced from water, as Jules Verne's novel seems to suggest [7]. Energy and chemical transformations are necessary in order to generate hydrogen starting from hydrogen rich compounds. This is the reason why it is referred to as “energy carrier” [8]. Figure 1 depicts the connection of three basic points in “hydrogen economy” as a network of primary energy sources ended with multiple uses through hydrogen as energy carrier [2].

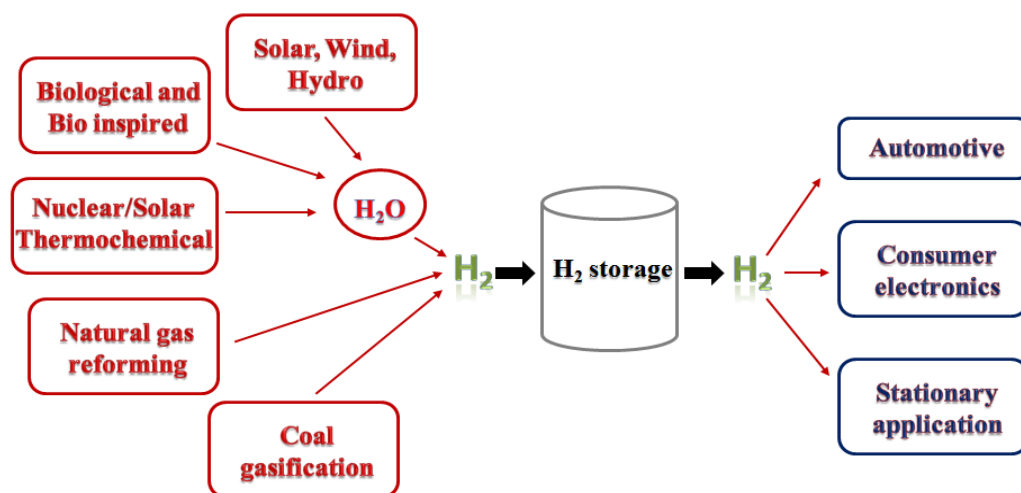


Figure 1. Hydrogen economy as a network of primary energy sources linked to different end-uses through hydrogen as an energy carrier [2] .

The main obstacle on the way to a hydrogen powered society is the efficient storage and release of hydrogen under ambient conditions [9]. Compression, liquefaction and solid state forms are possible ways of hydrogen storage. Compressed gas form and liquid hydrogen are the physical approaches which provides the only near term solutions because of the limitations with regard to very high pressures (about 700 bar) and cryogenic temperatures (20 K), respectively. Hence, the storage of hydrogen in solid state forms such as metal hydrides or chemical hydrides appears to be long term solution in which there is a chemical bonding between hydrogen and other elements [10]. Consequently, many efforts have been devoted to search for chemical materials possessing high gravimetric hydrogen density for both portable and stationary applications of hydrogen supply [11,12,13]. Among the several types of chemical hydrogen storage materials, boron-based hydrides have recently attracted great attention due to their high hydrogen content, safe storability, and easy hydrogen release under mild conditions [14]. Recent studies have shown that ammonia borane (AB) can be considered as a promising hydrogen storage material with high hydrogen content (19.6 wt. %) and low molecular weight ($30.7 \text{ g}\cdot\text{mol}^{-1}$) as well as high stability and nontoxicity [15].

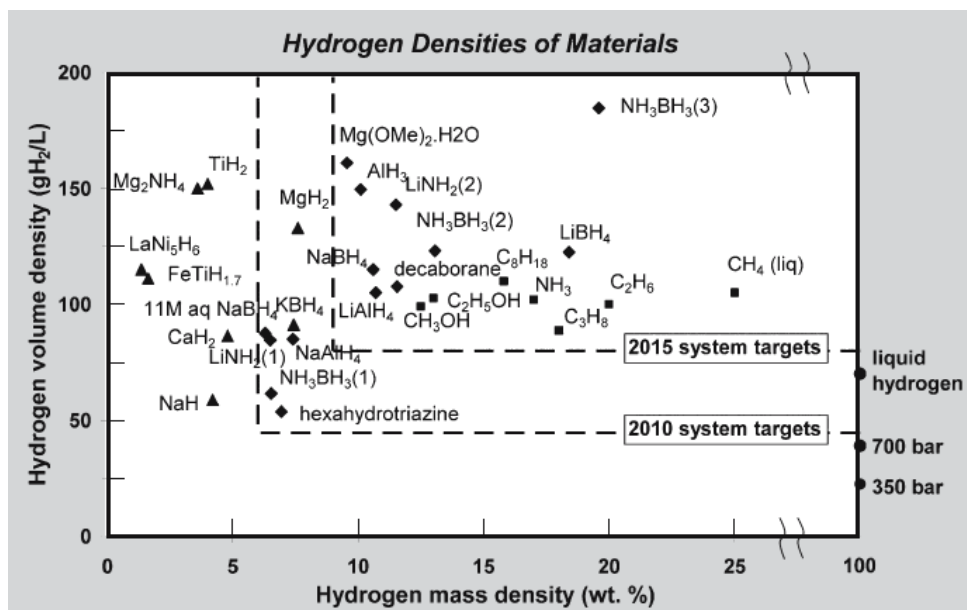


Figure 2. Hydrogen mass density vs. Hydrogen volume density for hydrogen storage materials [10].

In AB, the bond between B and N is a dative bond formed by the interaction of the nonbonding electron pair of NH_3 and empty orbital of boron in BH_3 [16] as an electron donor–acceptor complex. In solid AB structure, there is a short $\text{NH}\cdots\text{HB}$ intermolecular attraction which causes dihydrogen bond interaction [17] providing extra stability and formation of AB as a solid under standard conditions [18].

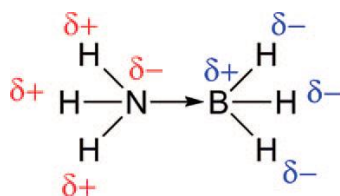


Figure 3. Bond polarizations in ammonia borane [19].

Hydrogen stored in AB can be released *via* different processes including thermal degradation in solid state [20,21,22], dehydrocoupling in non-aqueous medium [23,24], and solvolysis such as hydrolysis [25,26,27,28] and methanolysis [29]. In early years, hydrogen generation from AB was achieved by thermolysis, which has been widely studied because of the high amount of hydrogen released. However, high reaction temperature and difficulties in control of reaction are the main technical hindrance of thermal dehydrogenation of AB [30]. Hydrogen production from the dehydrogenation of AB in non protic solvents could also be achieved in the presence of homogeneous or heterogeneous catalysts. However, both the equivalent of H₂ per mole of AB and hydrogen generation rate of dehydrogenation of AB are lower than those of other hydrogen production methods. The other route for hydrogen generation from AB is solvolysis in protic solvents such as hydrolysis and methanolysis. In both hydrolysis and methanolysis, the hydridic hydrogen bound to B atom reacts with protonic hydrogen of the protic solvent, which can stoichiometrically liberate 3.0 equivalent H₂ gas [31]. Although the hydrolysis of AB has been extensively studied and widely accepted, the methanolysis of AB has a series of advantages: (i) the solubility of AB in methanol is high, 23 % wt. at 23 °C [32], (ii) the solution of AB in methanol is highly stable with respect to self-methanolysis at ambient conditions, (iii) pure H₂ gas can be produced from methanolysis of AB without ammonia contamination [29,33], (iv) methanolysis of AB can be initiated at temperatures below 0 °C in the presence of appropriate catalyst, which facilitates portable applications in cold weather [34], (v) the methanolysis product of AB, NH₄B(OCH₃)₄, can be converted back to AB by a room temperature reaction with LiAlH₄ plus NH₄Cl [29].

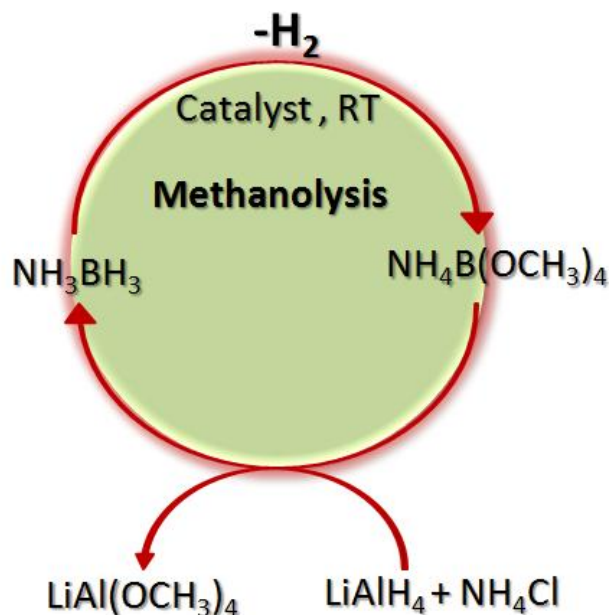
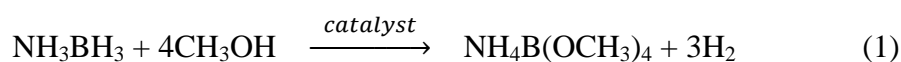


Figure 4. Ammonia borane regeneration cycle using the methanolysis product [35]

Methanolysis can release 3.0 equivalents of H_2 per mole of AB only in the presence of a suitable catalyst (Eqn. 1):



To date, a series of heterogeneous catalysts have been studied to speed up the methanolysis of AB, such as $RuCl_3$, $RhCl_3$, $PdCl_2$, $CoCl_2$, $NiCl_2$ [29], copper nanoparticles [36], polymer stabilized-nickel(0) [37], -palladium(0) [38] and -ruthenium(0) nanoparticles [39], Co- Co_2B , Ni- Ni_3B , Co-Ni-B [40], zeolite confined rhodium(0) nanoparticles [41], MMT-immobilized ruthenium(0) nanoparticles [42], cobalt-palladium nanoparticles [43], copper-palladium nanoparticles [44], mesoporous CuO nanostructures [45], Cu- Cu_2O -CuO/C [46], bunch-like CuO nanowire [47], graphene supported ruthenium(0) nanoparticles [48], AgPd nanoparticles [49] CuNi nanoparticles assembled on graphene [50], Rh/CC3-R-*hetero* and Rh/CC3-R-*homo* [51], Pd(0) NPs on graphene [52]. Among these catalysts, noble metal rhodium and ruthenium based catalysts provide the highest catalytic activity in hydrogen generation from the methanolysis of AB. However the

transition metal nanoparticles are prone to agglomerate to form their larger particles and ultimately bulk metal, thus their catalytic activities decline significantly in a certain reaction. Therefore, they need to be stabilized against agglomeration by supporting on materials with large surface area. Porous materials with large surface area have been used as support to obtain stable and catalytically active transition metal(0) nanoparticles [53]. The catalytic activity of nanoparticles also depends on the particle size of support. Reducing the particle size of support from the microcrystalline to the nanocrystalline regime (from $> 1 \mu\text{m}$ to $< 100 \text{ nm}$) can enhance the catalytic activity of the supported materials due to increase in the external surface area of support [54].

In the light of these information, this dissertation aims to study the hydrogen generation from the methanolysis of AB catalyzed by rhodium(0) nanoparticles, supported on the surface of nanopowders of oxide materials, namely hydroxyapatite, silica, alumina, and ceria. In the preparation method followed here, rhodium(II) or rhodium(III) ions were first impregnated on the surface of oxide nanopowders and, then *in situ* reduced by AB during the methanolysis reaction. The oxide supported rhodium(0) nanoparticles, hereafter referred to as Rh(0)/nanooxides, were isolated from the reaction medium and characterized by a combination of advanced analytical techniques. The rhodium(0) nanoparticles were found to be highly active and long-lived catalysts in hydrogen generation from the methanolysis of AB. The formation kinetics of rhodium(0) nanoparticles were studied by using the hydrogen generation as reporter reaction. Furthermore, kinetics of the methanolysis reaction of AB catalyzed by Rh(0)/nanooxides were investigated depending on the catalyst concentration, substrate concentration and temperature.

CHAPTER 2

CATALYSIS

2.1. General Principles of Catalysis

The term “catalysis” was first used by J.J. Berzelius in his research about catalytic decomposition of hydrogen peroxide in 1836. Berzelius defined a new entity capable of promoting the reaction of chemicals by a “catalytic contact”. He estimated that the role of such substance was to loosen the bonds which hold the atoms in the reacting molecules together. Thus, he used the term of “catalysis” (Greek *kata* = wholly, *lein* = to loosen). The modern definition of catalyst was made by Ostwald in 1894, thus; a catalyst is a substance that changes the rate of a chemical reaction, itself remaining chemically unchanged at the end of reaction. The process is called catalysis. Because the catalyst remains unchanged after chemical process, each catalyst molecule can join in many consecutive cycles, so even only small amount of catalyst relative to substrate is enough. Traditionally, catalysis can be divided into three main categories; homogeneous, heterogeneous and biocatalysis.

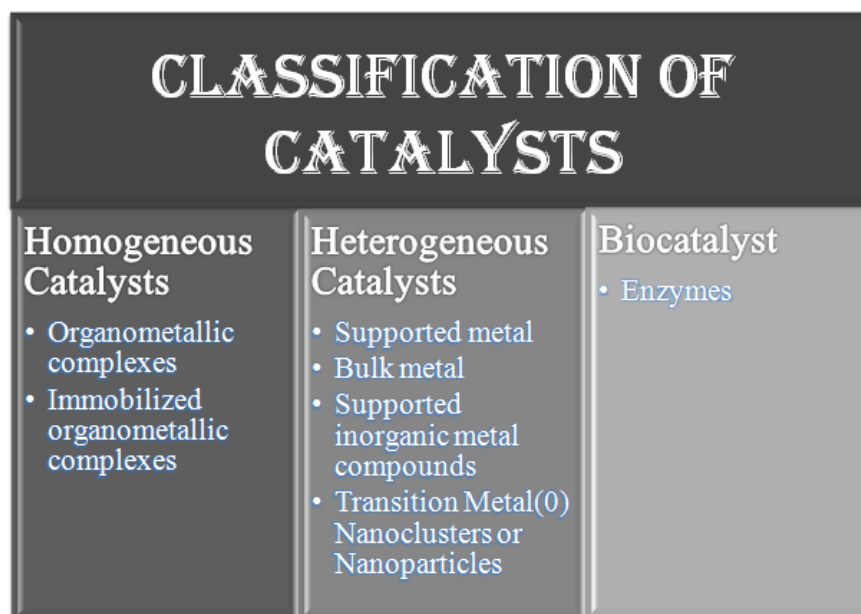


Figure 5. Classification of catalysts [55].

In homogeneous catalysis, the catalyst and reactant or their solution form a uniform phase. This type of catalysis can occur in the gas or liquid phase. The first industrial homogenous catalyzed reaction (1750) was the oxidation of sulphur dioxide (SO_2) to sulphur trioxide (SO_3) in the presence of nitric oxide (NO) as catalyst [56]. On the other hand, heterogeneous catalysis contains the system in which catalyst and reactants occur in different phases; besides, catalyst is generally in the solid form while reactants can be liquids or gases. Contact process is an example of heterogeneous catalysis to produce sulphuric acid, in which sulphur dioxide (SO_2) reacts with oxygen to generate sulphur trioxide (SO_3) on a solid vanadium(V) oxide (V_2O_5) catalyst. The main advantages of heterogeneous catalyst over the homogeneous one are easy separation of active catalyst from the reaction medium and reuse of heterogeneous catalyst in successive runs that provides continuous chemical processes. Moreover, heterogeneous catalysts have more tolerance to harsh reaction conditions than their homogeneous analogues. In heterogeneous catalytic reaction, reactants are adsorbed from fluid phase onto a catalyst surface *via* weak van der Waals forces (*Physical adsorption*) or partial

chemical bonds (*Chemisorption*). After the formation of activated complex, the products are formed and released from the catalyst surface.

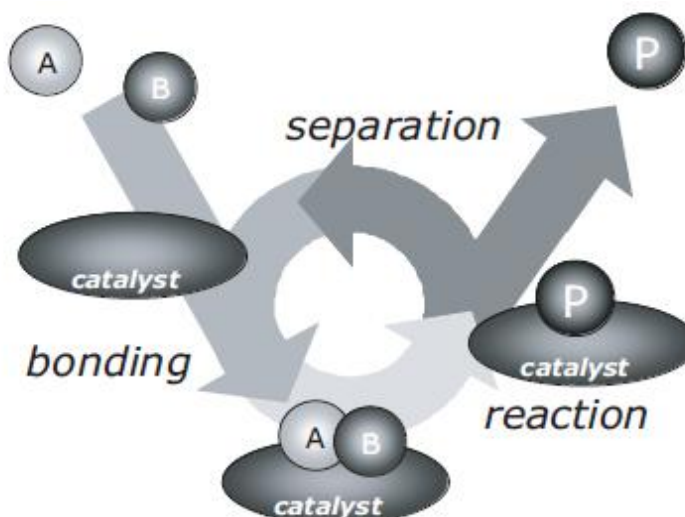


Figure 6. Mechanism of heterogeneous catalysis [57].

In catalytic reaction, catalysts enhance the rate of reaction by offering an alternative path that is more complex, but energetically more preferable. The activation energy of catalyzed reaction is lower than that of uncatalyzed reaction; hence, the effective molecular collisions having lower energies can surpass the new activation energy barriers, thus the reaction rate improves significantly. It is noteworthy that the extent of reaction remains same for both catalyzed and uncatalyzed reaction because the catalyst accelerates both forward and reverse reaction to the same extent; thereby the equilibrium constant for the reaction is not affected. It means that catalyst have an influence on the kinetic of the reaction but not on thermodynamics.

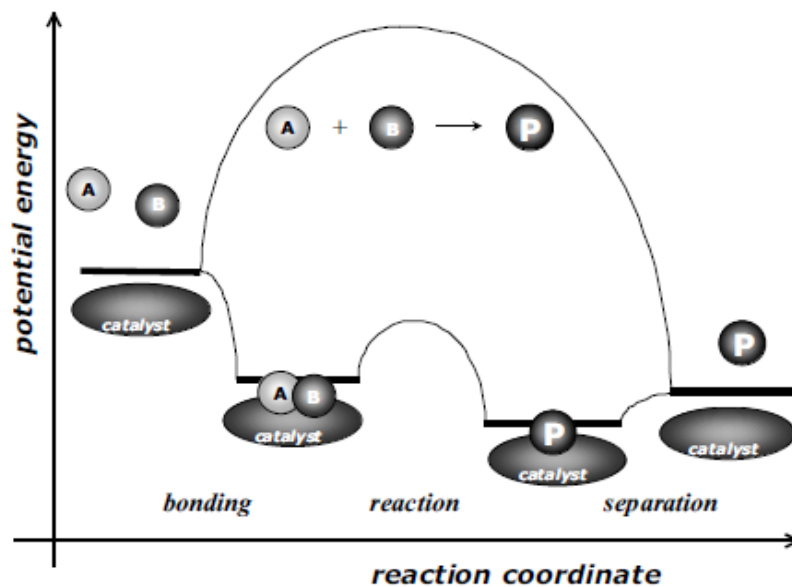


Figure 7. Potential energy diagram for both catalyzed and uncatalyzed reaction [57].

The other key parameters in catalytic applications are activity, selectivity and stability of the catalyst in a specified reaction. The activity of a catalyst can be explained by *total turnover number (TTON)* which is the number of the maximum reaction cycles that a catalyst attends in a specified reaction under definite circumstances before deactivation.

$$TTON = \frac{\text{mol of product}}{\text{mol of catalyst}} \quad (2)$$

The *turnover frequency* is often pronounced to define the efficiency of a catalyst. For a catalytic reaction of A to B with the rate of v ; TOF can be defined as the number of moles of product per mole of catalyst per unit time.

$$A \xrightarrow{\text{catalyst}} B$$

$$TOF = \frac{\text{mol of B}}{\text{mol of catalyst} \times \text{time}} \quad (3)$$

The second key parameter in catalytic reactions is *selectivity* of active catalyst that provides high ratio of desired product with minimum amount of the side products. In industrial applications, selectivity plays a vital role to minimize waste and maximize the effective use of the feedstock. Syn-gas reaction is one of the example in which different catalysts cause the formation of distinct products [58].

The last important parameter is the *stability* of a catalyst which determines the lifetime of a catalyst in a specified reaction. Due to deactivation reasons such as poisoning effects or decomposition during reaction, stability plays a critical role in the economics of the process.

2.2. What is nano-catalysis?

The importance of catalysis is incontrovertible in chemistry, where catalysis can be divided into three main groups: heterogeneous, homogeneous and biocatalysis. As mentioned in the previous section, heterogeneous and homogeneous catalytic approaches have some advantages. Although heterogeneous catalysts can be readily recovered from the reaction medium they have some drawbacks like mass transport problems. On the other hand, homogeneous catalysts present high activity and selectivity in the shade of separation problem of expensive transition metal catalysts from reactants and products [59].

Nanocatalysis has been intensively studied for many years as a branch of nanoscience. Nanoparticles can be considered as sustainable alternatives to conventional materials as active and robust heterogeneous catalysts [60] or catalyst supports [61]. The particles in nano regime provide higher surface area for catalytic applications (nanocatalysts). The extended surface area improves the contact between reactants and catalyst excessively. On that sense, nanocatalyst resembles the homogeneous catalysts. On the other hand, nanocatalysts can act as heterogeneous catalysts because of easy separation from reaction mixtures. Moreover, the activity and selectivity of nanocatalysts can be tuned by tailoring physical and chemical properties such as shape, size, composition or morphology [62]. The field of nanocatalysis is somewhere between homogeneous and heterogeneous catalysis communities, so nanocatalysts are sometimes named as *semi-heterogeneous* or *quasi-homogeneous* catalysts [63].

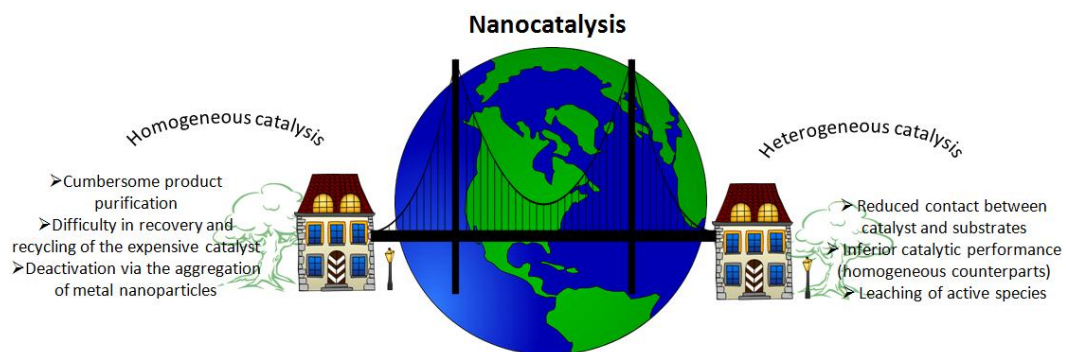


Figure 8. What is nanocatalyst?

CHAPTER 3

TRANSITION METAL(0) NANOPARTICLES IN CATALYSIS

3.1. General Introduction

A “zero-dimensional” structure is the simplest building block that may be used for nanomaterials design. The materials having diameters lower than 100 nm can be termed as nanoparticles, nanoclusters, or nanocrystals which are used synonymously in the literature. The term *nanoparticle* is generally used to define 0D nanostructures with dimensions smaller than 100 nm and relatively large ($\geq 15\%$) size dispersion [64]. The term *nanocluster* can be used to define a matter which has smaller in size (1 – 10 nm) with near-monodispersed size distribution [64]. The last term *nanocrystal* is used to define single crystals with diameters from a few nm up to 100 nm and unusual reactivity relative to large counterparts [64]. In the literature, different terms are used to define nanomaterials; therefore, in order to eliminate semantic problems, the term *nanoparticle* will be used throughout this dissertation to specify any type of metallic species in size regime of 1- 50 nm.

Transition metal(0) nanoparticles have gained great attention over the last half century. This attention originates from the different uses of these materials such as in catalysis [65], for preparation of materials with unique magnetic properties [66] and the design of devices in nanoelectronics at the molecular level [67]. If the electronic structures of nanoparticles are investigated, it is obviously seen that nanoparticles are somewhere between mononuclear coordination compounds and bulk metals. In the structure of mononuclear compounds, there are localized electronic systems with separated energy levels, however in bulk structures there are delocalized electronic systems involving broad energy bands. The increase in the number of metal atoms in nanoparticle increases in the number of bonding and antibonding electronic levels, thus decreases the energy band gap between electronic

levels [68]. The changes in the electronic structure of the cluster as a function of its size are called the *quantum size effect* [67].

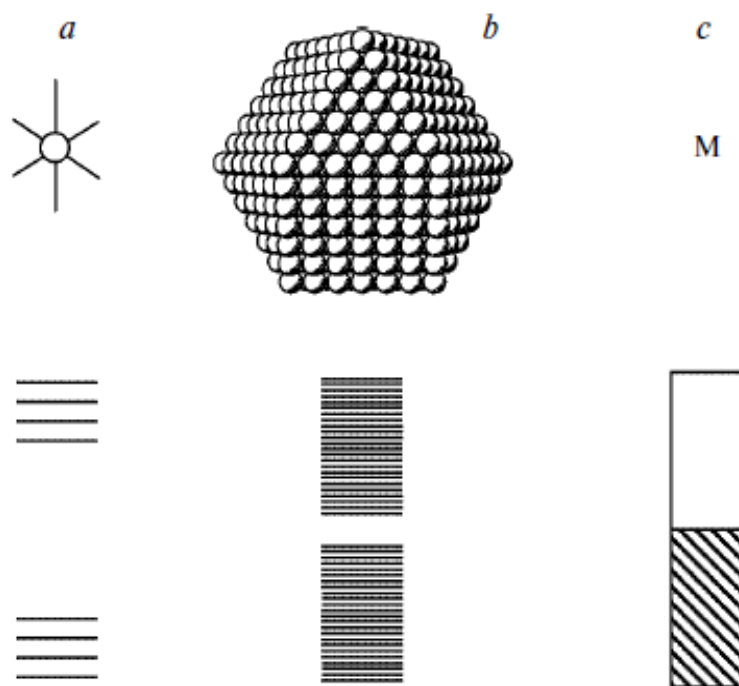


Figure 9. Schematic representation of electronic levels in (a) mononuclear complex (b) large cluster (c) bulk metal.

In addition to changes in electronic structures, nanoparticles have also distinct physical and chemical properties unlike their bulk counterparts. The most significant properties of nanoparticles are the high fraction of atoms constituting the nanoparticle on the particle surface rather than in the particle interior and larger surface area available per unit volume of the material. Both properties are enhanced by decreasing particle size. Besides, optical properties of nanoparticles become interesting because particle size and surface functionalization affect the absorption or emission wavelength. Transparency in nanoparticles could be obtained by reducing particle size below the critical wavelength of light. For metals, while melting

temperatures of nanoparticles decrease, magnetic behaviors enhance with decreasing particle size.

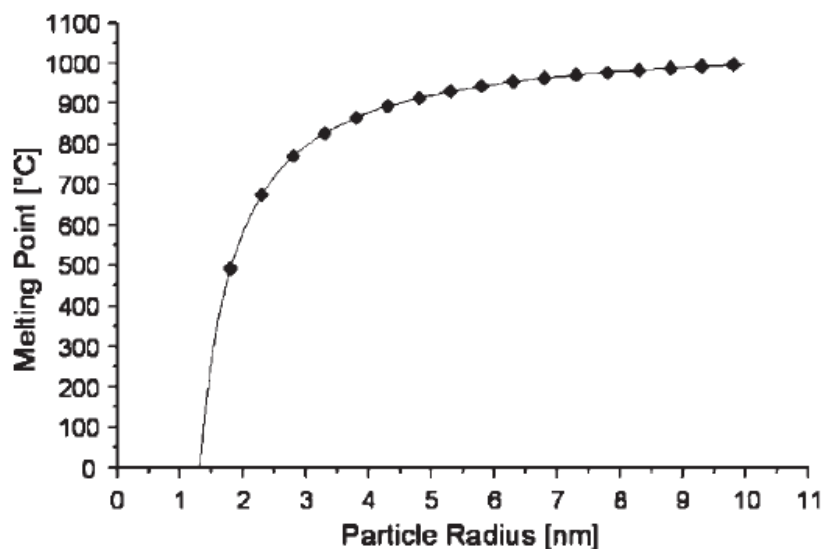


Figure 10. Melting point vs. particle size graph for gold nanoparticles [69].

3.2. Stabilization Modes for Metal(0) Nanoparticles

Due to the larger surface area of metal nanoparticles relative to their masses, metal nanoparticles have excess surface energy that causes thermodynamic instability. However, one of the most important properties of nanoparticles is their small particle size which provides them kinetic stability. Metal(0) nanoparticles have great tendency to agglomerate in order to form their bulk forms. In most cases, agglomeration causes the loss of specific properties of these materials derived from smaller particle size. At short distances, metal nanoparticles converge under the effects of the van der Waals forces; therefore, the presences of repulsive forces opposed to the van der Waals forces are necessary to prevent further growing. Special efforts have been devoted to the stabilization of metal nanoparticles with the

aim of not only preserving high surface area and activity, but also extending the lifetime of nanoparticles in solution after syntheses.

3.2.1. Electrostatic / DLVO-type Stabilization

DLVO is the classical theory for the electrostatic stabilization of nanoparticles that was developed by Derjagin-Landau-Verwey-Overbeek in 1940s. This theory states that nanoparticle stabilization is based upon a critical balance in interparticle forces between repulsive Coulombic forces and opposing attractive van der Waals forces [70]. Electrostatic stabilization could be provided by ionic compounds (i.e. halides, carboxylates or polyoxoanions) dissolved in solution. The adsorption of anions and their related counterions on unsaturated, electrophilic metal surface will form an electrical double layer around particles that causes a Coulombic repulsion between nanoparticles (Figure 11). In the case of enough electric potential based upon the double layer, further growing in particle size will stop, thus nanoparticles will be efficiently stabilized. The extent of stabilization can be readily affected by any phenomenon like ionic strength or thermal motion.

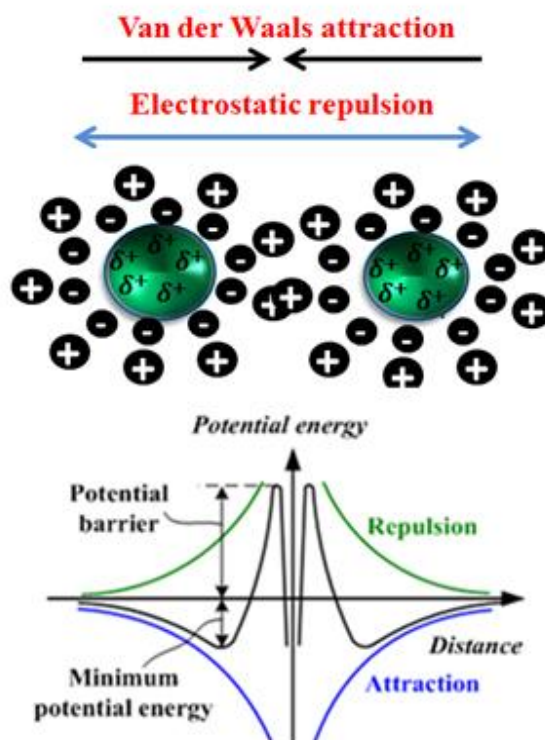


Figure 11. Electrostatic stabilization for transition metal nanoparticles and plot of energy *versus* distance between colloids [71].

3.2.2. Steric Stabilization

The stabilization of metal(0) nanoparticles could also be achieved by using sterically bulky materials such as polymers or oligomers. The adsorption of these large groups ensures a steric barrier by forming a protective layer (Figure 12). In contrast to electrostatic stabilization which is mainly applicable in aqueous solution, the steric stabilization can be applied in both organic and aqueous phase. Moreover, the length and nature of bulky groups adsorbed lead to change in thickness of the protective layer and thus affect the stability and activity of metal nanoparticles [72].

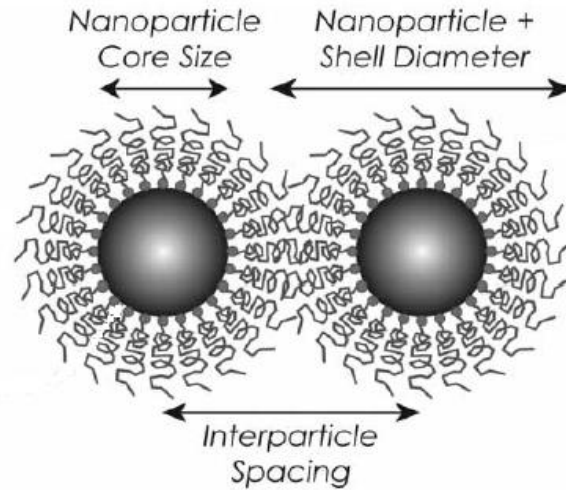


Figure 12. Schematic image of steric stabilization by adsorption of polymer chains onto a nanoparticle [73].

3.2.3. Electrosteric / Combination of DLVO Type Electrostatic and Steric Stabilization

In the literature, many researchers have used the combination of two well practiced modes of nanoparticle stabilization into so-called electrosteric stabilization. As the term electrosteric implies, this mode of stabilization is the combination of electrostatic and steric stabilization. This type of stabilization is generally achieved by means of ionic surfactants. Such compounds consist of a polar headgroup able to form an electric double layer and a lyophilic side chain able to supply steric repulsion [72].

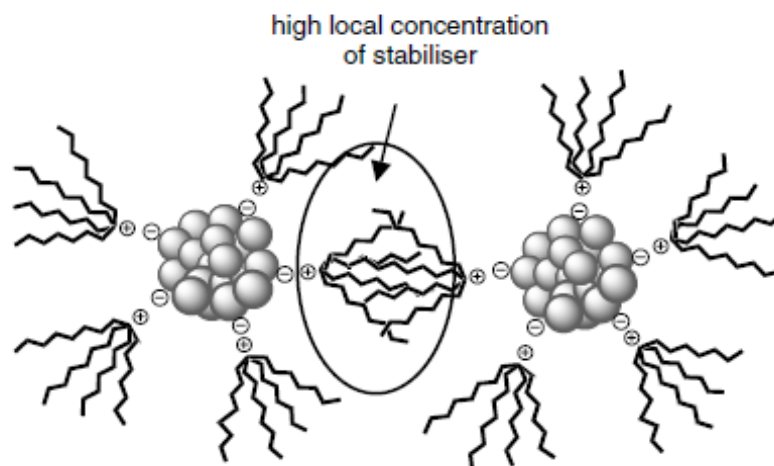


Figure 13. Schematic illustration of electrosteric stabilization of transition metal nanoparticles [74].

3.3. Synthesis Methods of Transition Metal(0) Nanoparticles

Nowadays, the main goal in transition metal nanoparticles research area is the development of reproducible synthesis methods which provide the formation of metal(0) nanoparticles with (i) specific size (1-10 nm) (ii) well characterized surface composition (iii) isolable and redispersible properties. Transition metal(0) nanoparticles can be fabricated by two main ways: *top-down* (physical way) and *bottom-up* (chemical way) methods. *Top-down* is the breakdown method by which solid is exposed to an external force that causes the breaking up of large particles into smaller ones. This physical approach causes broad particle size distribution (larger >10 nm). In addition, transition metal nanoparticles are not reproducibly prepared causing irreproducible catalytic activity [75]. *Bottom-up* methods contain nucleation and growth of metal atoms by which atoms or molecules (bottom) react under chemical or physical circumstances to generate metal nanoparticles. The main advantage of *bottom-up* method is the synthesis of monodispersed particles and thus the control of particle size. The *bottom-up* methods base basically upon the following methods; (i) chemical reduction of transition metal complexes [76], (ii) thermal or photochemical decomposition [77,78,79], (iii) decomposition of organometallics

[80], (iv) metal vapor synthesis [81], (v) electrochemical reduction [82] (vi) atomic layer deposition [83], (vii) precipitation from reverse micelle emulsions [84] (viii) sol-gel technique [85,86].

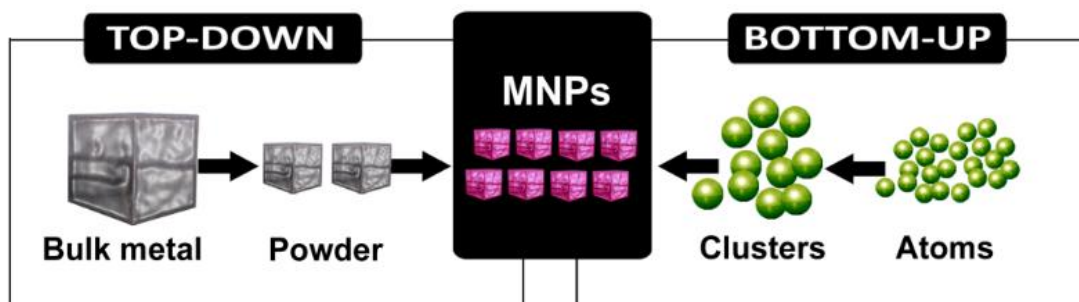


Figure 14. *Top down and bottom up* approaches used to obtain nanoparticles

3.4. Characterization of Transition Metal(0) Nanoparticles

In addition to the aim of synthesis of metal nanoparticles with near monodispersed size distribution, characterization of nanoparticles to get valuable insights about particle size and overall composition is another key goal in metal nanoparticle research area.

The most frequently used technique to characterize nanoparticles is *Transmission Electron Microscopy* (TEM) in order to get valuable information about particle size, shape, dispersion and morphology of metal nanoparticles. The important data about the crystal structures and lattice spacings of metal nanoparticles could also be obtained by *high resolution TEM* (HR-TEM).

X-Ray photoelectron spectroscopy (XPS) is another valuable technique to investigate elemental surface composition of nanoparticles as well as oxidation state and electronic environment of each component. Both qualitative and quantitative information can be obtained by evaluating chemical shifts of binding energies of

photoelectron for a specific element on the surface and the signal intensities, respectively.

The other commonly used method is *X-Ray diffraction* (XRD) to analyze nature of bulk structure as well as crystallite size, crystallographic, compositional and chemical inhomogeneties of nanocrystalline materials. The characteristic patterns of individual solids make XRD quite useful for the detection of the crystalline components of nanomaterials.

Scanning Electron Microscopy (SEM) gives information about surface morphologies of nanoparticles by analyzing either secondary or back-scattered electrons as a function of the position of the primary electron beam and the contrast of the signal. SEM can also be modified to perform elemental analysis by adding energy dispersive analysis of the x-rays (EDX) emitted by the sample [87].

The utilization of *UV-Visible Spectroscopy* (UV-vis) provides valuable information about the reduction of metal precursors and formation of metal nanoparticles in the existence of a stabilizing agent. In such a spectrum, one can easily observe the disappearance of an absorption band of the metal precursor and formation of a new absorption band for the nanoparticles.

Adsorption-desorption techniques are commonly studied for metal nanoparticles stabilized on supporting materials in order to obtain knowledge about surface area, pore volume and average pore size of supports before and after the synthesis of nanomaterials. The obtained adsorption isotherms can also be used to classify pore structure of supporting materials as microporous, mesoporous or macroporous.

Additionally, scanning tunnelling microscopy (STM), infrared spectroscopy (ATR-IR, FTIR), atomic force microscopy (AFM), elemental analysis (ICP-OES) are other commonly tools used in the characterization of the metal nanoparticles.

3.5. Scope of the Dissertation

As discussed in previous sections, preparation of transition metal nanoparticles with specific size and near monodispersed size distribution as well as stabilization of them in solution are of great attention due to their potential

applications in many fields such as catalysis. Metal nanoparticles can be stabilized against agglomeration to retain large surface area, high activity and long lifetime by using mesoporous or microporous oxide supports with large surface area. Reducing the particle size of support from the microcrystalline to the nanocrystalline regime (from $>1\ \mu\text{m}$ to $<100\ \text{nm}$) can enhance the catalytic activity of the supported materials due to increase in the external surface area of support [54]. As also discussed in Chapter 1, the release of hydrogen stored in AB can be achieved through solvolysis in solution. In this regard, methanolysis of AB has been considered as an efficient way of hydrogen release by keeping several advantages over the hydrolysis. Up to now, various transition metal(0) nanoparticles have been tested in hydrogen generation from the methanolysis of AB and among them noble metal rhodium and ruthenium based catalysts provide the highest catalytic activity in hydrogen generation from the methanolysis of AB.

The purpose of this dissertation is to prepare and characterize rhodium(0) nanoparticles stabilized on crystalline nanooxide support materials such as hydroxyapatite nanospheres, nanosilica, nanoalumina and nanocerium as well as to investigate their catalytic performance in regard to activity, stability, lifetime and heterogeneity in hydrogen generation from the methanolysis of ammonia borane. The following studies were performed in this dissertation;

i) *In situ* preparation of rhodium(0) nanoparticles supported on hydroxyapatite nanospheres (Rh(0)/nanoHAP), nanosilica (Rh(0)/nanoSiO₂), nanoalumina (Rh(0)/nanoAl₂O₃) and nanocerium (Rh(0)/nanoCeO₂) in a simple and reproducible way.

ii) The characterization of rhodium(0) nanoparticles supported on hydroxyapatite nanospheres, nanosilica, nanoalumina and nanocerium by advanced analytical techniques including ATR-IR, PXRD, TEM, HR-TEM, TEM –EDX, STEM-EDS XPS, SEM, SEM-EDX, ICP-OES and N₂ adsorption desorption.

iii) Investigating the catalytic performance of rhodium(0) nanoparticles supported on hydroxyapatite nanospheres, nanosilica, nanoalumina and nanocerium in hydrogen generation from the methanolysis of AB in order to get information about catalytic activity, stability, and lifetime as well as determination of activation parameters for each catalyzed reactions and understanding the formation kinetics of rhodium(0) nanoparticles during methanolysis of AB by using the hydrogen generation as reporter reaction.

CHAPTER 4

EXPERIMENTAL

4.1. Materials

Rhodium(III) chloride trihydrate ($\text{RhCl}_3 \cdot 3\text{H}_2\text{O}$), rhodium(II) octanoate dimer ($[\text{Rh}(\text{C}_7\text{H}_{15}\text{CO}_2)_2]_2$), ammonia borane (H_3NBH_3 , AB, 97%), methanol (99%) and hydroxyapatite nanospheres (nanoHAP, $\text{Ca}_{10}(\text{OH})_2(\text{PO}_4)_6$, particle size < 75 nm), nanosilica (nanoSiO₂, particle size ≈ 12 nm), nanoalumina (nanoAl₂O₃, particle size ≈ 13 nm) and nanoceria (nanoCeO₂, particle size ≈ 25 nm), were purchased from Aldrich. Tetrabutylammonium dihydrogen phosphate monobasic (TBAP, 97%) was purchased from Fluka. Methanol was distilled over metallic magnesium and stored under inert gas atmosphere. Distilled methanol was used in all methanolysis reactions under inert gas atmosphere unless otherwise specified. All glassware was cleaned with acetone, followed by copious rinsing with distilled water before drying in an oven at 120 °C.

4.2. Instrumentation

Rhodium content of the Rh(III)-exchanged hydroxyapatite nanospheres (Rh(III)/nanoHAP) samples and that of filtrate solutions obtained from leaching tests of Rh(0)/nanoSiO₂, Rh(0)/nanoAl₂O₃ and Rh(0)/nanoCeO₂ were determined by Inductively Coupled Plasma Optical Emission Spectroscopy (ICP-OES, Leeman-Direct Reading Echelle). Transmission electron microscopy (TEM) was performed on a JEM-2100F (JEOL) microscope operating at 200 kV. The TEM samples were harvested from *in situ* generated rhodium(0) nanoparticles supported on hydroxyapatite nanospheres (Rh(0)/nanoHAP), nanosilica (Rh(0)/nanoSiO₂), nanoalumina (Rh(0)/nanoAl₂O₃) or nanoceria (Rh(0)/nanoCeO₂) solution at the end of

catalytic methanolysis of AB. A few drops of nanoparticle solution was redispersed in 2 mL methanol and ultrasonicated for 3 min then, one drop of this solution was placed on the carbon coated copper grid of TEM and dried under inert atmosphere. Samples were examined at magnification between 100 and 400 K. The samples used for STEM-EDS, XPS, XRD, SEM or N₂ adsorption desorption analysis were harvested from *in situ* generated Rh(0)/nanoHAP, Rh(0)/nanoSiO₂, Rh(0)/nanoAl₂O₃ or Rh(0)/nanoCeO₂ solution at the end of catalytic methanolysis of AB. After settling of powders, supernatant solution was taken out using a capillary syringe. The remaining powder was dried under vacuum at room temperature. The X-ray photoelectron spectroscopy (XPS) analysis was performed on a Physical 15 Electronics 5800 spectrometer equipped with a hemispherical analyzer and using monochromatic Al K α radiation of 1486.6 eV, the X-ray tube working at 15 kV, 350W and pass energy of 23.5 keV. The X-ray diffraction (XRD) pattern was recorded on a MAC Science MXP 3TZ diffractometer using Cu-K α radiation (wavelength 1.5406 Å, 40 kV, 55 mA). The nitrogen adsorption/desorption experiments were carried out at 77 K using a NOVA 3000 series Quantachrome Instrument. The sample was out gassed under vacuum at 573 K for 3 h before the adsorption of nitrogen. SEM analyses were run on a JEOL JSM-5310LV operating at 15 kV and 33 Pa in a low-vacuum mode without metal coating on the aluminum support. UV–vis electronic absorption spectra were recorded on Varian-Carry100 double beam instrument. ATR-IR spectra were recorded on a Vartex-70 spectrophotometer. STEM-EDS mapping images were recorded on a Hitachi HT7700 TEM instrument equipped with STEM and EDAX modules operated at 120 kV. ¹¹B NMR spectra were recorded on a Bruker Avance DPX 400 (128.15 MHz for ¹¹B).

4.3. *In-situ* Preparation and Catalytic Activity of Rhodium(0) Nanoparticles Supported on Hydroxyapatite Nanospheres

4.3.1. Preparation of Rh(III)–exchanged hydroxyapatite nanospheres (Rh(III)/nanoHAP)

In a flask 80.8 mg (0.300 mmol) RhCl₃.3H₂O was dissolved in 50.0 mL water and hydroxyapatite nanospheres (1.0 g) were added to the solution. This slurry was

stirred at room temperature for 72 h, then Rh(III)/nanoHAP was isolated from the solution by centrifugation at 8000 rpm for 10 min and washed with 100 mL water and the remnant was dried at 120 °C for 24 h. The drying process of Rh(III)/nanoHAP continued under vacuum (10^{-3} Torr) at 90 °C for 8 h. Rh(III)/nanoHAP was stored in a Schlenk tube under inert gas atmosphere. Hydroxyapatite nanospheres samples were checked for water content by taking ATR-IR spectra.

4.3.2. *In situ* Formation of Rhodium(0) Nanoparticles Supported on Hydroxyapatite Nanospheres and Concomitant Catalytic Methanolysis of Ammonia Borane

In situ formation of rhodium(0) nanoparticles supported on hydroxyapatite nanospheres, hereafter referred to as Rh(0)/nanoHAP, and concomitant hydrogen generation from the methanolysis of ammonia borane (AB) were performed in the same reaction flask. The catalytic activity of Rh(0)/nanoHAP in the methanolysis of AB was determined by monitoring the liberation of hydrogen gas. The experiment was performed as follows: a jacketed reaction flask with a Teflon-coated stir bar is first evacuated to remove traces of oxygen and moisture present and then filled with nitrogen inert gas. The reaction flask is thermostated by circulating water through its jacket at a certain temperature specified. The gas outlet of the reaction flask is connected to a graduated glass tube filled with water through bubbler containing 20 mL of methylcyclohexane. (Figure 15) The same experimental set up was used for determining hydrogen gas generation during methanolysis AB catalyzed by Rh(0)/nanooxides and also to study kinetic experiments unless otherwise specified.

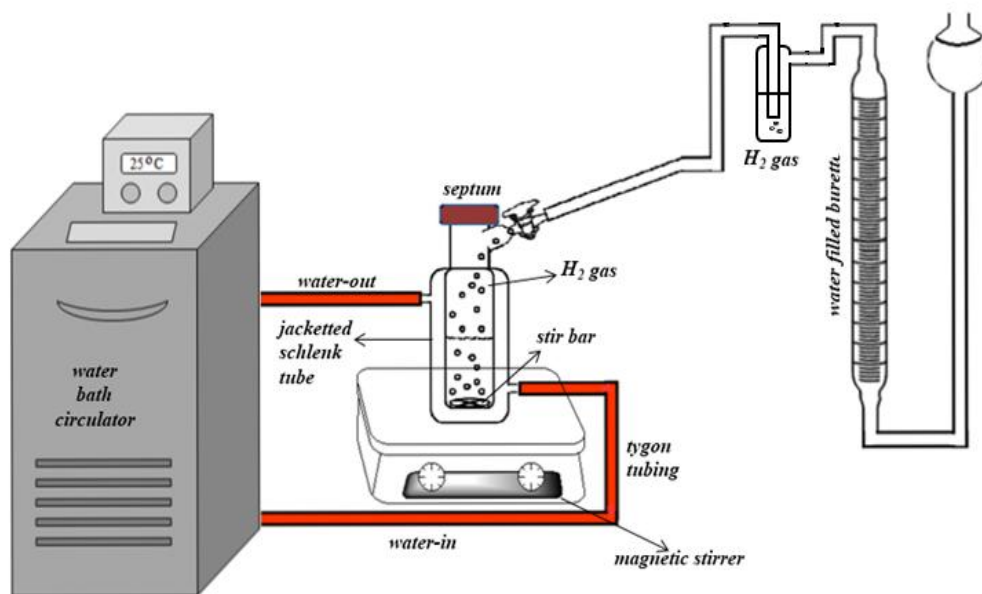


Figure 15. Experimental set-up used for determining hydrogen gas generation during reactions and also to study kinetic experiments.

A stock solution of 10 mM tetrabutylammonium dihydrogen phosphate, TBAP, which has been dried under vacuum (10^{-4} Torr) for 24h, was prepared by dissolving 70.0 mg (0.200 mmol) TBAP into 20 mL volumetric flask and diluted with methanol to 20.0 mL. The catalytic reaction solution with the desired concentration of TBAP was prepared by taking certain amount of aliquot from the stock solution and diluted by adding methanol. For instance, in a typical experiment, in order to prepare 0.8 mM TBAP solution (TBAP to metal ratio of 2), a 0.8 mL (0.008 mmol TBAP) aliquot of stock solution was transferred into reaction flask containing 20.0 mg powder of Rh(III)/nanoHAP (2.09 wt.% Rh, 4.06 μ mol Rh) and 6.2 mL methanol with a glass pipette, then reaction flask was thermostated for 5 minutes. In a Schlenk tube, 64 mg (2.0 mmol) AB was dissolved in 3.0 mL methanol while stirring under inert gas. Then, AB solution was added to the reaction flask *via* a gastight syringe, all at once, to launch catalytic methanolysis of AB. After the addition of AB, rhodium(0) nanoparticles formed and catalytic methanolysis of AB started without any induction time. The volume of hydrogen evolved during the

catalytic methanolysis was recorded by measuring the displacement of water level in the glass tube at constant pressure. When no more hydrogen liberated, experiment was stopped. Rh(0)/nanoHAP was separated from reaction solution by centrifugation and an aliquot of the solution was used for taking the ^{11}B NMR spectrum.

4.3.3. Effect of Tetrabutylammonium Dihydrogen Phosphate Concentration on Catalytic Activity of Rhodium(0) Nanoparticles Supported on Hydroxyapatite Nanospheres

In order to investigate the effect of tetrabutylammonium dihydrogen phosphate (TBAP) concentration on the catalytic activity of Rh(0)/nanoHAP, such experiment was studied in the same way specified in 4.3.2 section and started with 200 mM AB (64 mg), 0.609 mM Rh (30.0 mg Rh(III)/nanoHAP, 2.09 wt.%) and TBAP in different concentrations corresponding to the [TBAP]/[Rh] ratio of 0.0, 1.0, 2.0, and 4.0 in 10.0 mL methanol at 25.0 ± 0.5 °C. The best catalytic activity was obtained at TBAP to rhodium(0) nanoparticles molar ratio of 2.0. Hereafter, all experiments were performed using the [TBAP]/[Rh] ratio of 2.0 unless otherwise specified.

4.3.4. Kinetic Experiments and Determination of Activation Parameters for Methanolysis of Ammonia Borane Catalyzed by Rhodium(0) Nanoparticles Supported on Hydroxyapatite Nanospheres

In order to develop the rate law for the catalytic methanolysis of AB catalyzed by Rh(0)/nanoHAP, a series of experiments was performed in the same way as specified in 4.3.2 section. In such an experiment, the concentration of AB was kept constant at 200 mM and rhodium(0) concentration was altered in the range of 0.203, 0.406, 0.609, 0.812, 1.015 mM by keeping [TBAP]/[Rh] ratio of 2.0 for each rhodium concentration in 10.0 mL methanol at 25.0 ± 0.5 °C.

In order to determine the activation parameters, catalytic methanolysis of 200 mM (64 mg) AB was performed starting with 0.406 mM Rh (20.0 mg Rh(III)/nanoHAP, 2.09 wt.%) and [TBAP]/[Rh] ratio of 2.0 at various temperatures. The values of rate constant k_{obs} were determined from the plots of hydrogen versus time and utilized to calculate the activation energy (E_a^{app})

by using Arrhenius plot as well as the enthalpy change of activation ($\Delta H^{\ddagger,app}$) and the entropy change of activation ($\Delta S^{\ddagger,app}$) by drawing Eyring-Polanyi plot.

4.3.5. Recyclability Test of Rhodium(0) Nanoparticles Supported on Hydroxyapatite Nanospheres in the Methanolysis of Ammonia Borane.

After the completion of hydrogen generation from the methanolysis of 200 mM AB, the catalyst (Rh(0)/nanoHAP) was kept in the reaction solution and a new batch of AB (64 mg, 2.0 mmol) was added to reaction medium. The hydrogen generation was monitored. The same procedure was repeated in six cycles.

4.3.6. Leaching Test of Rhodium(0) Nanoparticles Supported on Hydroxyapatite Nanospheres in the Methanolysis of Ammonia Borane.

After the first run of methanolysis of 200 mM AB catalyzed by 20.0 mg of Rh(0)/nanoHAP (2.09 wt. % Rh, 0.406 mM Rh), the catalyst was allowed to settle down, the gas outlet system was detached from the line and the reaction solution was filtered under inert gas atmosphere and transferred into another reaction flask. A new batch of AB (64 mg) was added to the solution and hydrogen generation from the methanolysis of AB was followed at $25.0 \pm 0.5^\circ\text{C}$. No hydrogen generation from the methanolysis of AB was observed. In addition, filtrate solution was analyzed by ICP-OES to confirm that no rhodium leached into the solution from the surface of hydroxyapatite nanospheres during the methanolysis.

4.3.7. Heterogeneity Test for Rhodium(0) Nanoparticles Supported on Hydroxyapatite Nanospheres by Carbon Disulfide Poisoning in the Methanolysis of Ammonia Borane.

Catalyst poisoning experiment was performed by using carbon disulfide (CS_2) as poison to test the heterogeneity of the methanolysis of AB catalyzed by Rh(0)/nanoHAP. Firstly, a 2.0 mM stock solution of CS_2 was prepared in 10.0 mL methanol. A typical methanolysis reaction of AB catalyzed by Rh(0)/nanoHAP was initiated with 0.406 mM Rh (20.0 mg Rh^{+3} /nanoHAP, 2.09 wt.%), [TBAP]/[Rh] ratio of 2.0 and 200 mM AB at $25.0 \pm 0.5^\circ\text{C}$. At the time when about 40% of hydrogen evolved, 0.4 mL (0.8 μmol) CS_2 solution was added to reaction medium *via* a gastight syringe in order to poison the catalyst. The hydrogen generation ceased

immediately upon the addition of CS₂ solution and the reaction was followed for 10 minutes to observe no further hydrogen evolution.

4.4. *In situ* Preparation and Catalytic Activity of Rhodium(0) Nanoparticles Stabilized on Nanosilica or Nanoalumina or Nanoceria

4.4.1. *In Situ* Preparation of Rh(II)-Ion Impregnated on Nanosilica or Nanoalumina or Nanoceria Surface

A stock solution of 4.9 mM Rh(II) was prepared by dissolving 47.8 mg (0.123 mmol Rh) rhodium(II)octanoate dimer in about 10 mL methanol in a 25.0 mL volumetric flask and by adding more methanol to get 25.0 mL volume. Certain aliquot of this stock solution was transferred into the reaction flask containing nanosilica or nanoalumina or nanoceria powder. For instance, for the preparation of a 0.49 mM Rh precatalyst mixture, 1.0 mL (4.9 μ mol Rh) aliquot of stock solution is transferred into reaction flask containing 50 mg nanosilica or nanoalumina or nanoceria powder which corresponds to a rhodium loading of 1.0 wt.% Rh. After addition of 6.0 mL methanol with a glass pipette, the resulting suspension was stirred for 3h to obtain Rh(II)-ion impregnated on nanosilica (Rh(II)/nanoSiO₂) or for 1h to prepare Rh(II)-ion impregnated on nanoalumina (Rh(II)/nanoAl₂O₃) or for 1h to prepare Rh(II)-ion impregnated on nanoceria (Rh(II)/nanoCeO₂) to ensure complete adherence of Rh(II) ions to the support at 25.0 \pm 0.5 °C.

4.4.2. *In situ* Formation of Rhodium(0) Nanoparticles Stabilized on Nanosilica or Nanoalumina or Nanoceria and Catalytic Methanolysis of Ammonia Borane

The *in situ* formation of rhodium(0) nanoparticles stabilized on nanosilica, hereafter referred to as Rh(0)/nanoSiO₂, or nanoalumina, hereafter referred to as Rh(0)/nanoAl₂O₃, or nanoceria, hereafter referred to as Rh(0)/nanoCeO₂ and concomitant hydrogen generation from the methanolysis of AB were achieved in the same reaction flask. The catalytic activity of Rh(0)/nanoSiO₂ or Rh(0)/nanoAl₂O₃ or Rh(0)/nanoCeO₂ in the methanolysis of AB was determined by following the liberation of hydrogen gas. The experimental set up specified in section 4.3.2 was used to measure hydrogen gas evolved from the methanolysis of AB (Figure 15). In a typical experiment, a solution of 64 mg (2.0 mmol) AB in 3.0 mL methanol is added *via* a gastight syringe to the reaction flask containing 7.0 mL suspension of Rh(II)/nanoSiO₂ or Rh(II)/nanoAl₂O₃ or Rh(II)/nanoCeO₂ in methanol with the

desired Rh(II) concentration and the catalytic methanolysis of AB is launched. After a short induction time, the color changes from pale blue to black indicating the formation of rhodium(0) nanoparticles in methanol solution and rapid hydrogen generation from methanolysis of AB starts. The volume of hydrogen evolved during catalytic methanolysis is recorded by measuring the displacement of water level in the glass tube at constant pressure. When no more hydrogen liberated, experiment is stopped.

4.4.3. Kinetic Experiments and Determination of Activation Parameters for Methanolysis of Ammonia Borane Catalyzed by Rhodium(0) Nanoparticles Stabilized on Nanosilica, Nanoalumina or Nanoceria

In order to develop a rate law for catalytic methanolysis of AB catalyzed by Rh(0)/nanoSiO₂ or Rh(0)/nanoAl₂O₃ or Rh(0)/nanoCeO₂, a series of experiment was performed in the same way specified in 4.4.2 section. In the first one, catalytic methanolysis of AB was studied by keeping the concentration of AB constant at 200 mM (64 mg AB) and varying the loading of rhodium(0) nanoparticles in the range of 0.50, 1.0, 2.0, 3.0, 5.0 wt.% Rh for Rh(0)/nanoSiO₂ and 0.50, 1.0, 1.5, 2.0 wt.% Rh for Rh(0)/nanoAl₂O₃ and 1.0, 2.0, 3.0 and 4.0 % wt. Rh for Rh(0)/nanoCeO₂.

In order to determine the activation parameters, catalytic methanolysis of 200 mM (64 mg) AB was performed starting with 0.49 mM Rh for Rh(II)/nanoSiO₂ (50 mg Rh(II)/nanoSiO₂ precatalyst, 1.0 wt.% Rh,) or 0.24 mM Rh for Rh(II)/nanoAl₂O₃ (50 mg Rh(II)/nanoAl₂O₃ precatalyst, 0.50 wt.% Rh) at various temperatures. In the studies of Rh(0)/nanoCeO₂, a series of the experiments was performed in which catalytic methanolysis of 200 mM (64 mg) AB was run starting with 0.49, 0.99 and 1.5 mM Rh for Rh(II)/nanoCeO₂, providing 1.0, 2.0 and 3.0 wt.% Rh, respectively at different temperatures. For each temperature, the value of rate constant, k_{obs} , was calculated from the hydrogen generation rate and used to determine the activation energy (E_a^{app}) by using Arrhenius plot as well as the enthalpy change of activation ($\Delta H^{\ddagger,app}$) and the entropy change of activation ($\Delta S^{\ddagger,app}$) by drawing Eyring-Polanyi plot.

4.4.4. Catalytic Lifetime of Rhodium(0) Nanoparticles Stabilized on Nanosilica, Nanoalumina or Nanoceria in the Methanolysis of Ammonia Borane

The lifetime of the catalyst was measured by determining the total turnover number (TTON) of hydrogen generation from the methanolysis of AB catalyzed by

Rh(0)/nanoSiO₂ or Rh(0)/nanoAl₂O₃ or Rh(0)/nanoCeO₂. For this purpose, lifetime experiment was started with 10 mL solution containing 50 mg Rh(II)/nanoSiO₂ (2.0 wt.% rhodium, 9.9 μmol Rh) or 50 mg Rh(II)/nanoAl₂O₃ (0.50 wt.% rhodium, 2.4 μmol Rh) or 50 mg Rh(II)/nanoCeO₂ (1.0 wt.% rhodium, 4.9 μmol Rh) and 400 mM (128 mg) AB at 25.0 ± 0.5 °C. When the expected amount of hydrogen evolved, a new batch of substrate was added to the reaction medium under nitrogen inert gas. Same procedure was applied until no more hydrogen liberation was observed.

4.4.5. Heterogeneity test for Rhodium(0) Nanoparticles Stabilized on Nanosilica or Nanoalumina by Carbon Disulfide Poisoning in the Methanolysis of Ammonia Borane

In order to test the heterogeneity of rhodium(0) nanoparticles stabilized on nanosilica or nanoalumina, catalyst poisoning experiment was performed by using carbon disulfide (CS₂) as poison. Firstly, a stock solution of CS₂ was prepared in the same way as described in section 4.3.7. Then, a typical methanolysis reaction of AB catalyzed by Rh(0)/nanoSiO₂ or Rh(0)/nanoAl₂O₃ was initiated with 50 mg Rh(II)/nanoSiO₂ (1.0% wt. Rh, 0.49 mM Rh) or Rh(II)/nanoAl₂O₃ (0.50 % wt. Rh, 0.24 mM Rh) and 200 mM AB at 25.0 ± 0.5 °C. At the time when about 40% of hydrogen evolved, 0.5 mL (0.2 μmol) CS₂ solution was added to reaction medium *via* a gastight syringe in order to poison the catalyst. Hydrogen generation ceased immediately upon the addition of CS₂ solution and the reaction was followed for 10 minutes to observe no further hydrogen evolved.

4.4.6. Leaching test for Rhodium(0) Nanoparticles Stabilized on Nanosilica, Nanoalumina or Nanoceria

After the first run of catalytic methanolysis of 200 mM AB, catalyzed by 50 mg Rh(0)/nanoSiO₂ or Rh(0)/nanoAl₂O₃ (0.50 % wt. Rh, 0.24 mM Rh), or Rh(0)/nanoCeO₂ (1.0% wt. Rh, 0.49 mM Rh) the reaction was stopped and opened under nitrogen inert gas atmosphere and the suspension in reaction flask was filtered; the filtrate was transferred in another reaction flask, and 64.0 mg AB (200 mM AB) was added. The hydrogen generation from methanolysis of AB was followed as described above. No hydrogen generation was observable in 2 h indicating that the filtrate has no catalytic activity in the methanolysis of AB; thus no leaching of rhodium into the solution could be detected. Additionally, the filtrate solution obtained by filtration of the reaction

mixture after the catalytic methanolysis reaction is also analyzed by ICP-OES for the rhodium content.

CHAPTER 5

RESULTS AND DISCUSSIONS

In the literature, there have been enormous reports that show the preparation and stabilization of transition metal(0) nanoparticles on the surface of microporous or mesoporous [53,88,89] as well as oxide supports with large surface area [90,91,92]. These stabilized metal(0) nanoparticles present outstanding catalytic activity in many different chemical reactions [93,94,95,96]. The main purpose of this dissertation is to develop rhodium(0) nanoparticles supported on the surface of oxide nanopowders as catalysts for hydrogen generation from the methanolysis of ammonia borane. The downsizings of particle size of the support materials from micrometer to nanometer can significantly enhance the catalytic activity because support materials with smaller particle size are expected to provide a higher external surface area, a large number of exchanged sites, and lower mass transfer limitations at low temperatures. In what follows, results of the study on rhodium(0) nanoparticles supported on nanooxide materials will be given in the order of hydroxyapatite, silica, alumina, and ceria.

5.1. Preparation and Characterization of Rhodium(0) Nanoparticles Supported on Hydroxyapatite Nanospheres and Further Stabilized by Dihydrogen Phosphate Ion and Investigation of Their Catalytic Activities in Hydrogen Generation From the Methanolysis of Ammonia Borane

In the first part of this dissertation, hydroxyapatite nanospheres ($\text{Ca}_{10}(\text{OH})_2(\text{PO}_4)_6$, particle size <75 nm) was chosen as a host material for the stabilization of rhodium(0) nanoparticles. The reasons of why hydroxyapatite nanospheres were preferred can be summarized as follows;

- i)* having nonporous structure which eliminates the mass transfer limitation,

- ii) showing high ion-exchange capability and adsorption capacity,
- iii) owing to the low surface acidity, which eliminates side reactions derived from support [97].

5.1.1. Preparation and Characterization of Rhodium(0) Nanoparticles Supported on Hydroxyapatite Nanospheres and Further Stabilized by Dihydrogen Phosphate Ion

Rhodium(0) nanoparticles supported on hydroxyapatite nanospheres, hereafter referred to as Rh(0)/nanoHAP, were prepared by ion-exchange of Rh³⁺ ions with Ca²⁺ ions of hydroxyapatite, followed by reduction of the resulting Rh(III)-exchanged hydroxyapatite nanospheres (Rh(III)/nanoHAP) precatalyst during the catalytic methanolysis of AB in the presence of tetrabutylammonium dihydrogen phosphate at room temperature. Firstly hydroxyapatite nanospheres were added to the aqueous solution of rhodium(III) chloride and stirred at room temperature for 72 h. After centrifugation, copious washing with distilled water and then drying under vacuum (10⁻³ Torr) at 90 °C for 8 h, Rh(III)/nanoHAP precatalyst was obtained. Then, Rh(III)/nanoHAP precatalyst was reduced to Rh(0)/nanoHAP during the catalytic methanolysis of AB in the presence of tetrabutylammonium dihydrogen phosphate at room temperature. The active catalyst was isolated from the reaction solution at the end of methanolysis reaction of AB by centrifugation and characterized by a combination of advance analytical techniques.

In order to check whether Rh(III)/nanoHAP could be completely dried after long drying process at 90 °C, ATR-IR spectra were taken for both nanoHAP and Rh(III)/nanoHAP and given in Figure 16. The comparison of two spectra shows the common absorption peaks due to the functional groups of hydroxyapatite. A weak absorption peak at 3570 cm⁻¹ due to the O-H stretching is observed in both spectra, confirming the integrity of hydroxyapatite powder [98,99]. No absorption peak is observed for the presence of water in the hydroxyapatite samples indicating that both samples are completely dried.

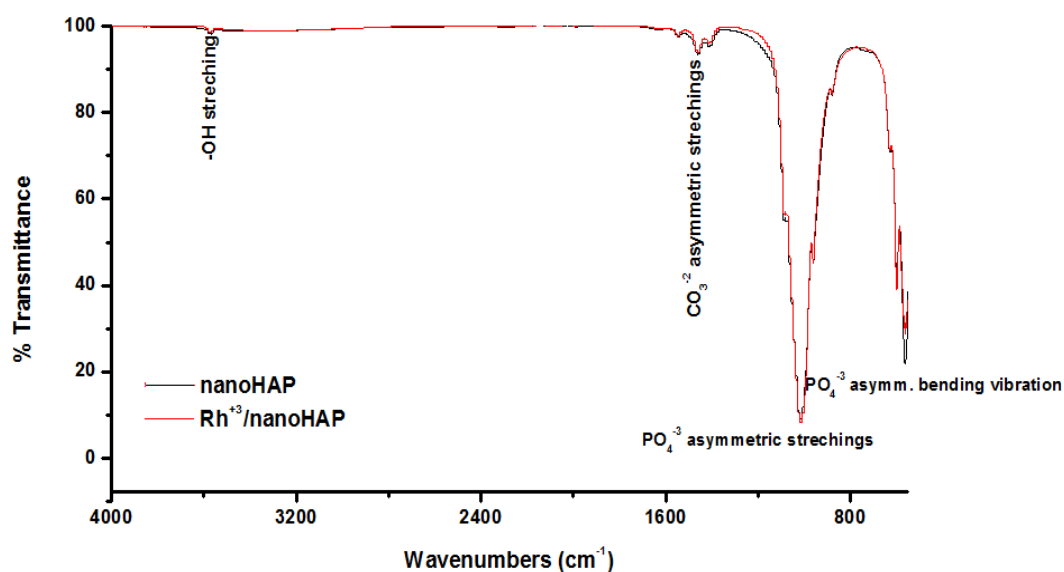


Figure 16. ATR-IR spectrum of nanosized hydroxyapatite and Rh(III)/nanoHAP after drying process.

The elemental analysis by inductively coupled plasma optical emission spectroscopy (ICP-OES) was performed in order to determine the actual rhodium content of Rh(III)/nanoHAP after ion exchange process. The result exhibits a rhodium loading of 2.09 % wt. for the sample. This loading value was used to prepare desired rhodium concentration in reaction solution.

Figure 17 depicts the powder X-Ray diffraction (PXRD) patterns of nanoHAP, Rh(III)/nanoHAP, and Rh(0)/nanoHAP altogether for comparison. PXRD patterns of the latter two are identical to that of the host nanoHAP framework, thus demonstrating that there is no noticeable change in intensities and positions of the main Bragg peaks or loss in the crystallinity [100]. Consequently, the host material remain intact after the preparation of Rh(III)/nanoHAP and the reduction of Rh^{3+} ions to Rh(0) during the methanolysis of AB. There is no detectable peak attributable to rhodium nanoparticles in Figure 17b and 17c, due to low rhodium content on nanoHAP.

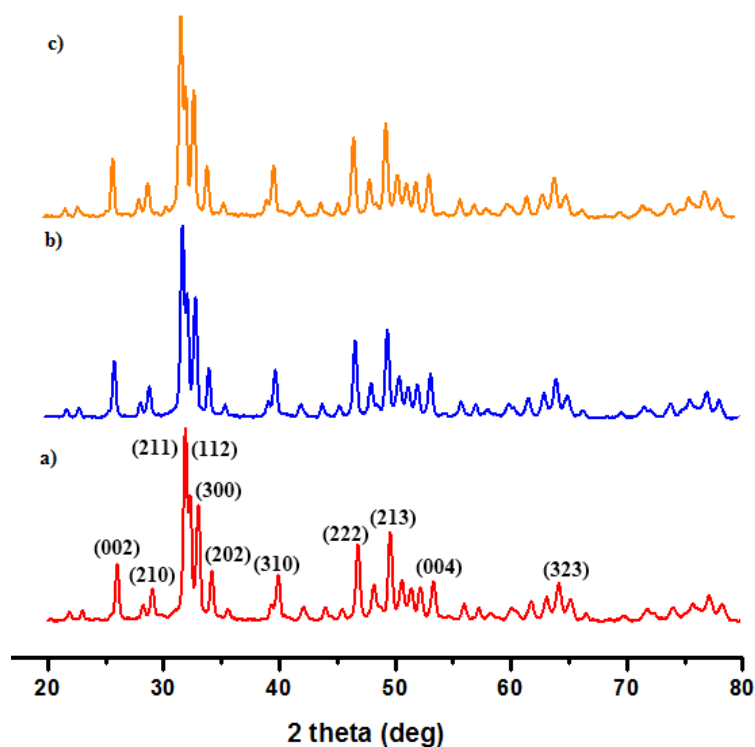


Figure 17. Powder X-ray diffraction (PXRD) patterns of (a) hydroxyapatite nanospheres ($[\text{Ca}_5(\text{OH})(\text{PO}_4)_3]_x$), (b) Rh(III)-exchanged hydroxyapatite nanospheres (Rh(III)/nanoHAP) and (c) rhodium(0) nanoparticles supported on hydroxyapatite nanospheres (Rh(0)/nanoHAP).

Figure 18 shows the results of TEM analyses of Rh(0)/nanoHAP with a rhodium loading of 2.09% wt. taken at different magnifications after catalytic reaction. TEM images in Figure 18 a-c present the uniform dispersion of rhodium(0) nanoparticles on the surface of nanoHAP support. The particle size histogram of rhodium(0) nanoparticles in Figure 18d was obtained by measuring the size of more than 50 non-touching nanoparticles from different TEM images. The particle size of highly dispersed rhodium(0) nanoparticles on the surface of nanoHAP varies from 3.6 nm to 6.4 nm with a mean diameter of 4.7 ± 0.8 nm.

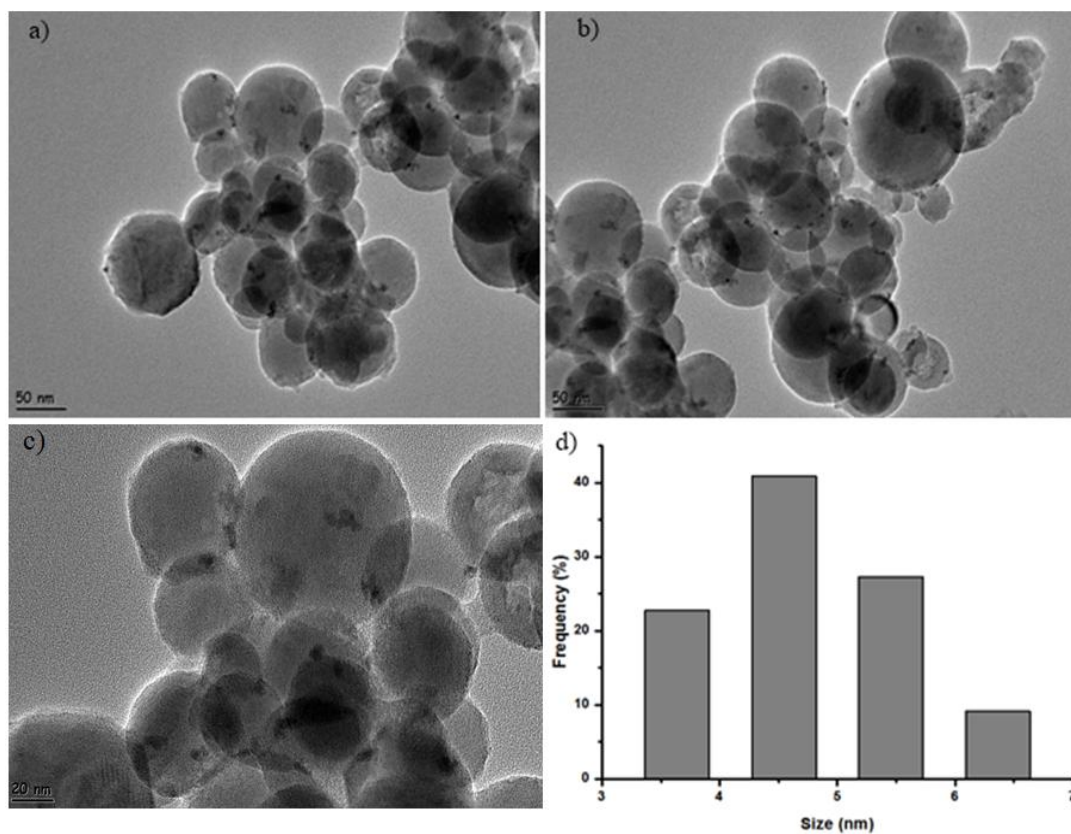


Figure 18. (a), (b), (c) TEM images of Rh(0)/nanoHAP in different magnifications (d) corresponding particle size histogram of Rh(0)/nanoHAP .

The existence of rhodium(0) nanoparticles on the surface of nanoHAP can be confirmed by TEM-EDX spectrum taken from the various areas of Rh(0)/nanoHAP samples (Figure 19). The TEM-EDX spectrum proves the existence of rhodium as the sole element in addition to the framework elements of the hydroxyapatite (Ca, P, and O) and also Cu from TEM grid.

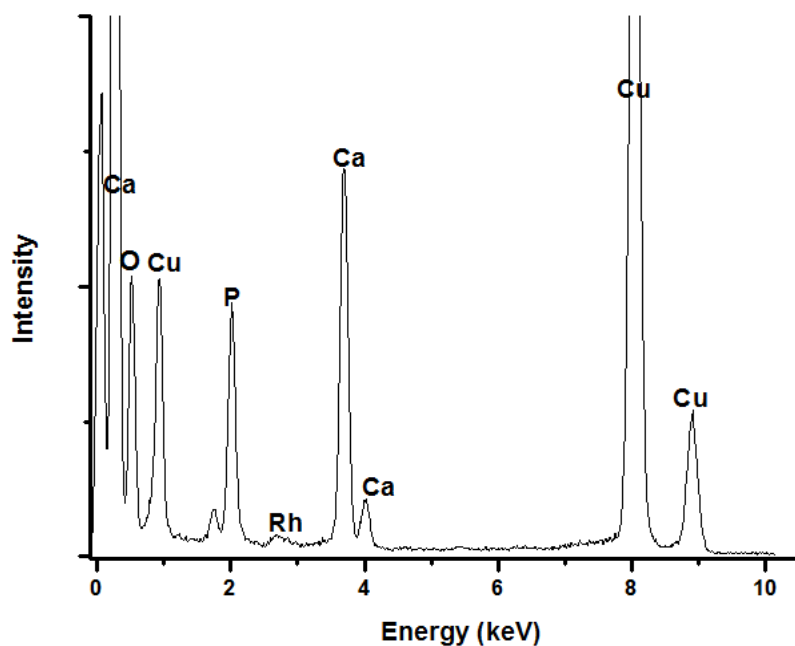


Figure 19. TEM-EDX spectrum of rhodium(0) nanoparticles supported on hydroxyapatite nanospheres with a rhodium loading of 2.09 wt %.

X-Ray photoelectron spectroscopy (XPS) gives valuable insights about the oxidation state of rhodium and the surface composition of Rh(0)/nanoHAP. Figure 20a depicts the survey scan XPS spectrum of Rh(0)/nanoHAP sample which indicates that rhodium is the only element detected in addition to the framework (elements Ca, P, and O) of hydroxyapatite. The high resolution XPS spectrum of Rh(0)/nanoHAP after sputtering with argon ion in Figure 20b shows two prominent bands at 306.6 and 311.4 eV that are readily assigned to Rh(0) $3d_{5/2}$ and Rh(0) $3d_{3/2}$, respectively [101,102]. Two additional peaks at higher energy 309.7 and 314.2 eV can be ascribed to Rh³⁺ $3d_{5/2}$ and Rh³⁺ $3d_{3/2}$, respectively [102].

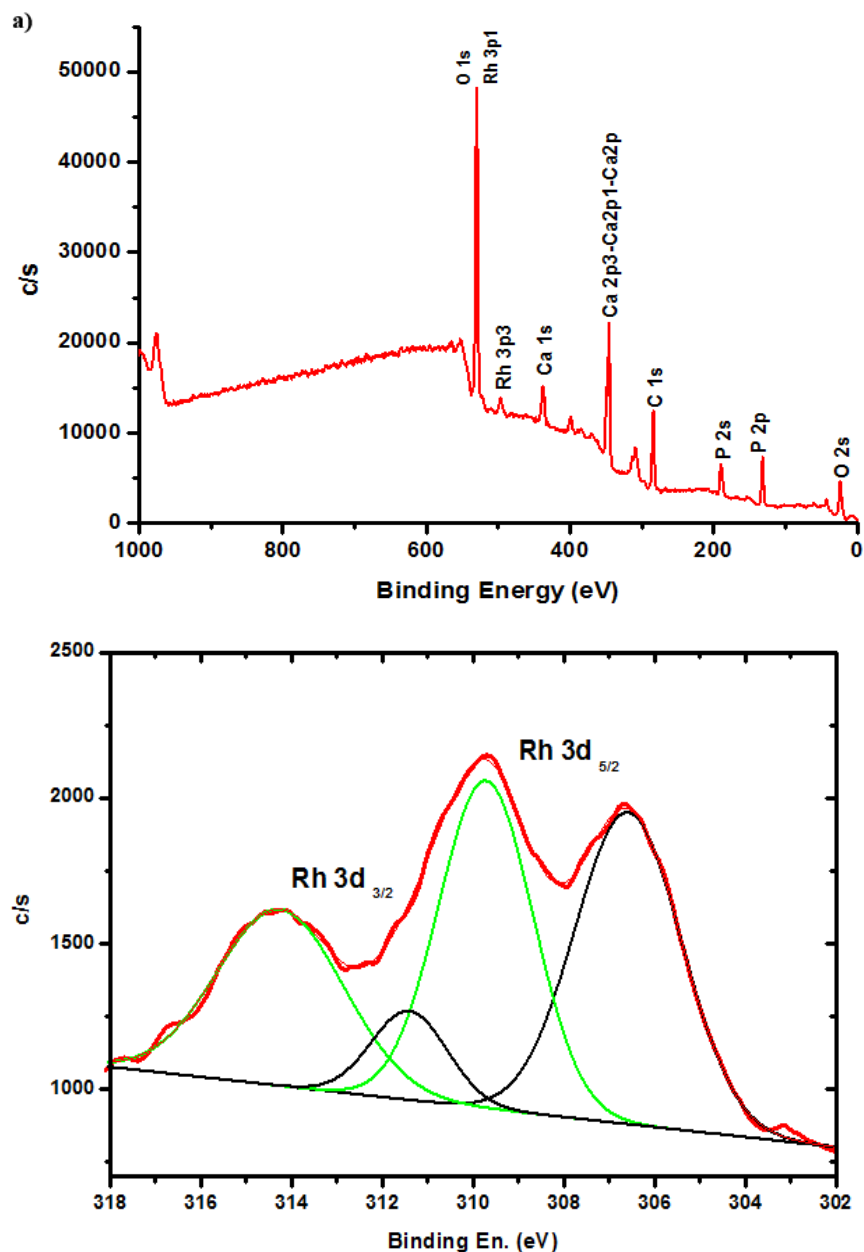


Figure 20. a) X-ray photoelectron (XPS) survey scan of Rh(0)/nanoHAP b) XPS high resolution spectra of Rh(0)/nanoHAP for Rh 3d after the methanolysis of AB.

The Rh^{3+} species are most likely formed on the surface of nanoparticles upon exposure to air during XPS sampling. Figure 21 shows the results of the sputtering of Rh(0)/nanoHAP sample by argon ion bombardment which causes an increase in the relative intensity of two bands of Rh(0) while a decrease in the relative intensity of Rh(III) bands. This observation reinforces the assumption that the surface of

rhodium(0) nanoparticles is partially oxidized when exposed to air for a few minutes during XPS sampling.

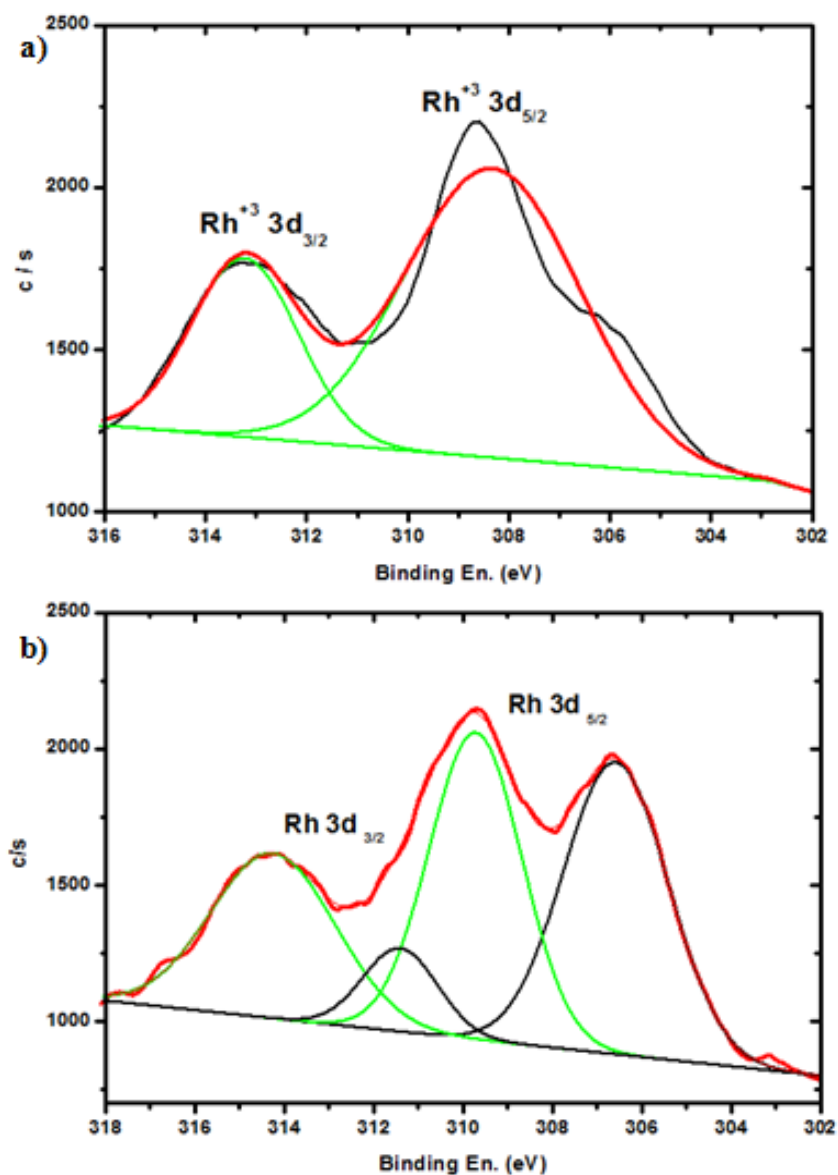


Figure 21. High resolution Rh 3d XPS spectrum of Rh(0)/nanoHAP a) before sputtering and b) after sputtering by argon bombardment.

Nitrogen adsorption-desorption isotherms of both nanoHAP and Rh(0)/nanoHAP sample are given in Figure 22. The results show that both have type III isotherm indicating the absence of micropores (<2 nm) [103]. Brunauer-Emmett-Teller (BET) surface area of bare nanoHAP was determined to be 25.9 m².g⁻¹, which is lower than that of Rh(0)/nanoHAP (31.9 m².g⁻¹). The slight increase by 6.0 m².g⁻¹ in the surface area measurement on passing from nanoHAP to Rh(0)/nanoHAP is a complementary finding for the existence of rhodium(0) nanoparticles on the surface of hydroxyapatite nanospheres.

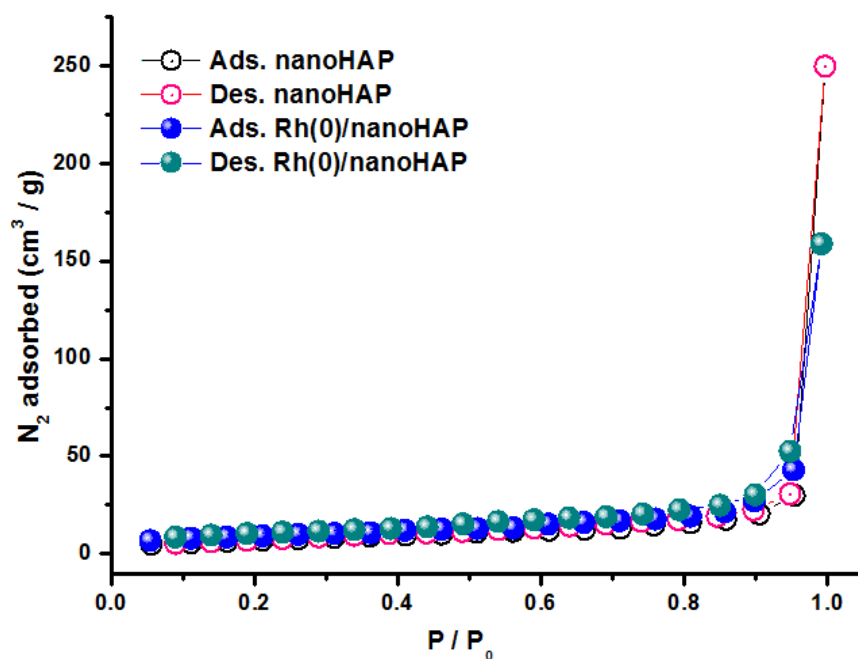


Figure 22. Nitrogen adsorption-desorption isotherms of nanoHAP and Rh(0)/nanoHAP.

5.1.2. The Catalytic Activities of Rhodium(0) Nanoparticles Supported on Hydroxyapatite Nanospheres and Further Stabilized by Dihydrogen Phosphate Ion in Hydrogen Generation From the Methanolysis of Ammonia Borane

5.1.2.1. Kinetic Studies and Determination of Activation Parameters for the Methanolysis of Ammonia Borane Catalyzed by Rhodium(0) Nanoparticles Supported on Hydroxyapatite Nanospheres and Further Stabilized by Dihydrogen Phosphate Ion

In the preparation steps of rhodium(0) nanoparticles supported on hydroxyapatite nanospheres, firstly Rh^{3+} ions were replaced with Ca^{2+} ions of host material by ion-exchange, then the resulting Rh(III) ions impregnated on hydroxyapatite nanospheres (Rh(III)/nanoHAP) were reduced to rhodium(0) nanoparticles supported on hydroxyapatite nanospheres (Rh(0)/nanoHAP) during the catalytic methanolysis of ammonia borane (AB) in the presence of tetrabutylammonium dihydrogen phosphate ions (TBAP). The formation of rhodium(0) nanoparticles and concomitant hydrogen generation from the methanolysis of AB were followed by monitoring the volume of H_2 gas liberated and then converting into equivalent H_2 per mole of AB using the known 3:1 H_2/AB stoichiometry (on page 7, Eqn.1). The manner in hydrogen generation from the methanolysis of AB catalyzed by Rh(0)/nanoHAP can be observed in Figure 23 presenting the plots of mol of H_2 evolved per mole of AB *versus* time for the catalytic methanolysis starting with 200 mM AB, 0.609 mM Rh (30.0 mg Rh(III)/nanoHAP, 2.09 %wt. Rh) and with or without [TBAP]/[Rh] ratio of 2.0 in 10.0 mL methanol at 25.0 ± 0.5 °C.

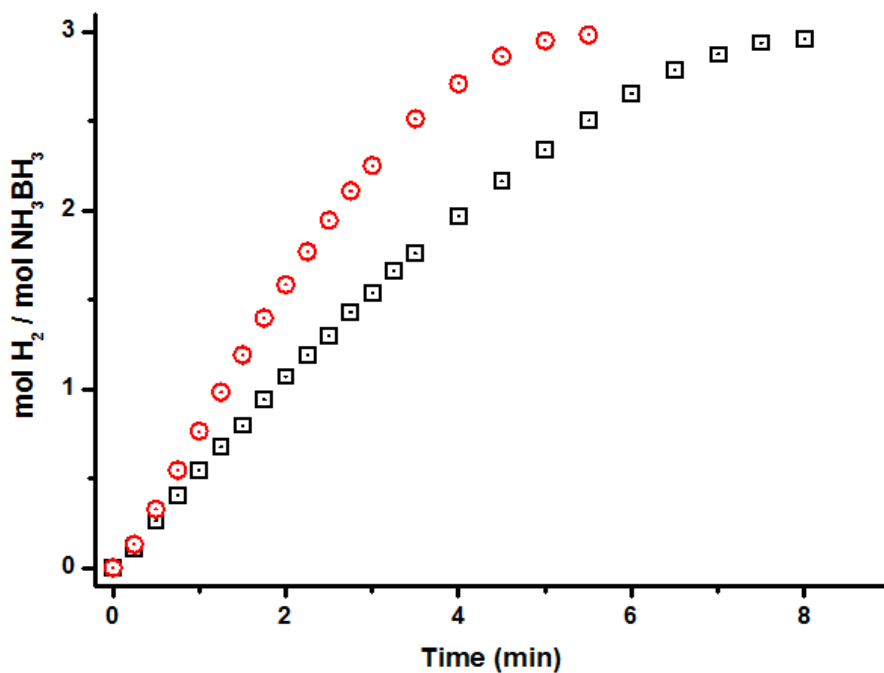


Figure 23. Plots of mol of H₂ evolved per mole of AB *versus* time for methanolysis of 200 mM AB starting with 0.609 mM Rh (30.0 mg Rh(III)/nanoHAP, 2.09 wt.%) and with (○) or without (□) [TBAP]/[Rh] ratio of 2.0 in 10.0 mL methanol at 25.0 ± 0.5 °C.

Note that AB acts as both reducing agent and substrate in the catalytic methanolysis reaction; therefore injection of AB solution into the reaction flask causes the reduction of Rh(III) ions to rhodium(0) nanoparticles, thus hydrogen liberation from the methanolysis of AB launches instantly without an induction time and holds almost linearly until the production of 3.0 equivalents of H₂ gas per mole of AB. Although Rh(0)/nanoHAP are active catalyst in hydrogen generation from the methanolysis of AB, their catalytic activity declines in the course of methanolysis reaction, indicating that sole hydroxyapatite nanospheres does not provide enough stabilization for rhodium(0) nanoparticles (Figure 23). Therefore, they need to be further stabilized. In the literature, there have been many researches suggesting the use of hydrogen phosphate anion as stabilizer for the nanoparticles of transition metals with atomic size matching to the O-O distance in the

phosphate ion [104,105,106,107]. Tetrabutylammonium dihydrogen phosphate (TBAP) was added into the reaction solution to further stabilize rhodium(0) nanoparticles supported on hydroxyapatite nanospheres during the methanolysis of AB. In order to investigate the effect of TBAP concentration on the catalytic activity of rhodium(0) nanoparticles in the methanolysis of AB, catalytic activity studies were performed starting with four different samples having different [TBAP]/[Rh] ratio. Figure 24 shows the plots of mol H₂ evolved per mole of AB *versus* time during the catalytic methanolysis starting with 200 mM AB (64 mg), 0.609 mM Rh (30.0 mg Rh(III)/nanoHAP, 2.09 wt.%) and TBAP in different concentrations corresponding to the [TBAP]/[Rh] ratio of 0.0, 1.0, 2.0, and 4.0 in 10.0 mL methanol at 25.0 ± 0.5 °C. In all cases, while hydrogen generation starts immediately without induction time, the initial hydrogen generation rate shows dependence on the relative concentration of TBAP. The plot of variation in hydrogen generation rate with the [TBAP]/[Rh] ratio for the methanolysis of AB is shown in the inset of Figure 24. The catalytic activity is enhanced by increasing the concentration of TBAP, reaching a maximum value of 46.1 mL H₂/min at the [TBAP]/[Rh] ratio of 2.0 and then decreasing with further increase in the concentration of TBAP. The excess amount of TBAP causes a high coverage of rhodium(0) nanoparticles surface, inhibiting effective contact of substrate molecules and rhodium(0) nanoparticles on the surface of hydroxyapatite nanospheres and thus catalytic activity declines. The data given in the inset of Figure 24 is another piece of evidence for the contribution of phosphate anions to the stabilization of rhodium(0) nanoparticles on the surface of hydroxyapatite [108]. The optimum [TBAP]/[Rh] ratio is determined to be 2.0 regarding the catalytic activity and stability of rhodium(0) nanoparticles. When [TBAP]/[Rh] ratio of 2.0 is used, the hydrogen generation continues almost linearly until the consumption of AB present in the solution. In other words, the activity loss in the course of reaction is negligible at this concentration of TBAP stabilizer. Therefore, all experiments were performed using the [TBAP]/[Rh] ratio of 2.0 unless otherwise specified.

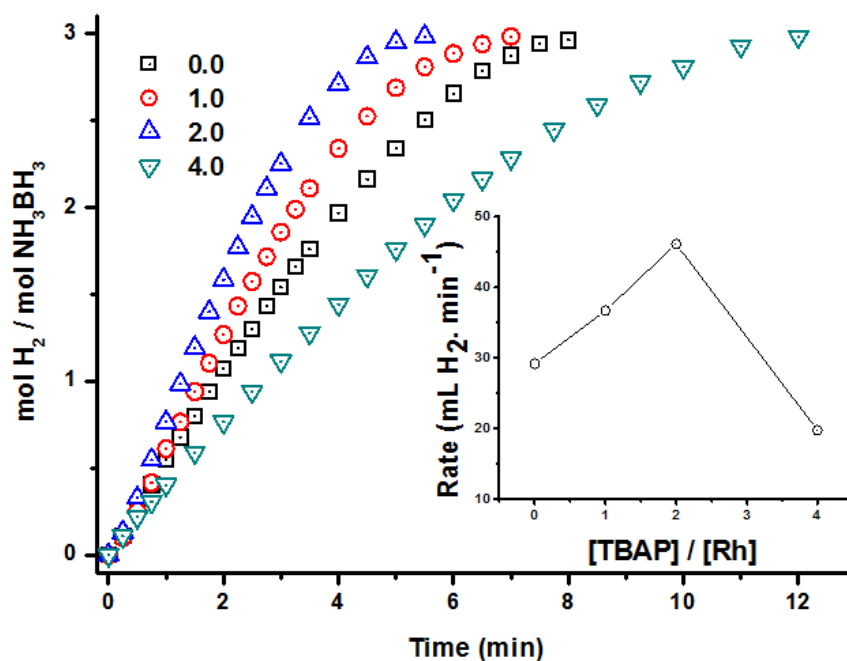


Figure 24. Plots of mol H₂ evolved per mole of AB *versus* time for the methanolysis of AB starting with 10.0 mL solution containing 200 mM AB (64 mg), 0.609 mM Rh (30.0 mg Rh(III)/nanoHAP, 2.09 wt.%) and [TBAP] / [Rh] in different ratios at 25.0 ± 0.5°C. Inset: Plot of hydrogen generation rate *versus* [TBAP]/[Rh] ratio for the methanolysis of AB.

Rhodium(0) nanoparticles supported on hydroxyapatite nanospheres and further stabilized by dihydrogen phosphate anion are highly active catalyst in hydrogen generation from the methanolysis of AB even at low concentration and room temperature providing 3.0 equivalent H₂ per mole of AB. Figure 25 exhibits the plots of mol H₂ evolved per mole of AB *versus* time during the catalytic methanolysis starting with 200 mM AB in the presence of TBAP ([TBAP]/[Rh] ratio of 2.0) and Rh(III)/nanoHAP (2.09% wt Rh) in various rhodium concentrations at 25.0 ± 0.5 °C.

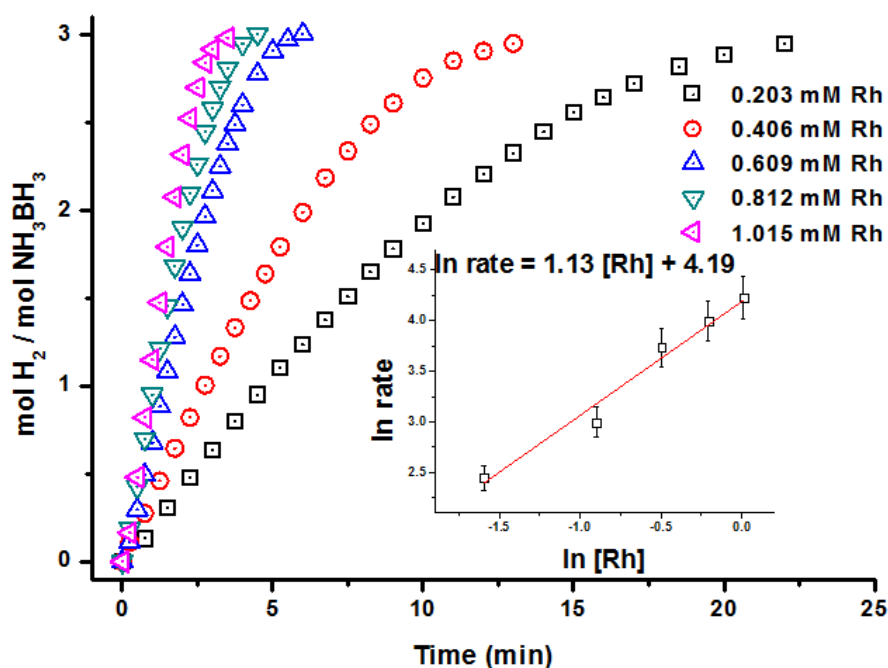


Figure 25. Plots of mol H₂ evolved per mole of AB *versus* time for the methanolysis of 10.0 mL solution of 200 mM AB in different metal concentrations ([Rh] = 0.203, 0.406, 0.609, 0.812, 1.015 mM) and 2.0 equivalent of TBAP stabilizer per mol of rhodium at 25.0 ± 0.5 °C. Inset: Plot of hydrogen generation rate *versus* the concentration of rhodium (both in logarithmic scale.)

There is no observable induction time in each plots, hydrogen generation starts instantly and proceeds almost linearly until 3.0 equivalents hydrogen liberated. It is clearly seen that the initial rate of hydrogen generation increases with the increasing concentration of catalyst. The hydrogen generation rate was determined from the linear portion of the graph for each experiment and plotted *versus* the initial concentration of rhodium, both axes in logarithmic scale. This plot gives a straight line with a slope of 1.1 indicating that the methanolysis of AB catalyzed by Rh(0)/nanoHAP is first order with respect to catalyst. Since the rate of hydrogen generation does remain essentially unchanged in the course of reaction, the catalytic methanolysis of AB is assumed to be independent of substrate concentration, at least in the range used in our study.

In order to determine activation parameters, temperature dependence of the methanolysis of AB catalyzed by Rh(0)/nanoHAP was investigated at different temperature in the range of 20-40 °C at constant rhodium ([Rh]=0.406 mM, 20.0 mg Rh(III)/nanoHAP, 2.09 wt.%) and substrate concentration ([AB]=200 mM, 64 mg) as well as the [TBAP]/[Rh] ratio at 2.0 in 10.0 mL methanol. The plots of mol H₂ evolved per mole of AB *versus* time for the catalytic methanolysis of AB at different temperatures are illustrated in Figure 26a. Expectedly, the rate of hydrogen generation from the methanolysis of AB increases with the increasing temperature. The values of observed reaction rate constant, k_{obs} , at various temperatures calculated from the slope of the linear part of each plot in Figure 26a were used for the construction of Arrhenius [109] and Eyring [110] plots given in Figure 26b and c, respectively. The slope of Arrhenius line was used to calculate apparent Arrhenius activation energy, yielding the activation energy $E_a^{app} = 56 \pm 2$ kJ/mol. This value is relatively lower than the value determined for the same methanolysis catalyzed by PVP-stabilized Ni (62 kJ/mol) [37] or Cu-Cu₂O-CuO (67.9 kJ/mol) [46] but still higher than the 40 kJ/mol found for the methanolysis of AB catalyzed by zeolite confined Rh (40 kJ/mol) [41] or 35 kJ/mol for PVP-stabilized Pd [38]. The other activation parameters were determined from Eyring plot. The slope and intercept of Eyring plot were used to calculate activation enthalpy, $\Delta H^{\ddagger,app} = 58 \pm 2$ kJ/mol; and activation entropy, $\Delta S^{\ddagger,app} = -27 \pm 4$ J/mol K, for the methanolysis of AB catalyzed by Rh(0)/nanoHAP.

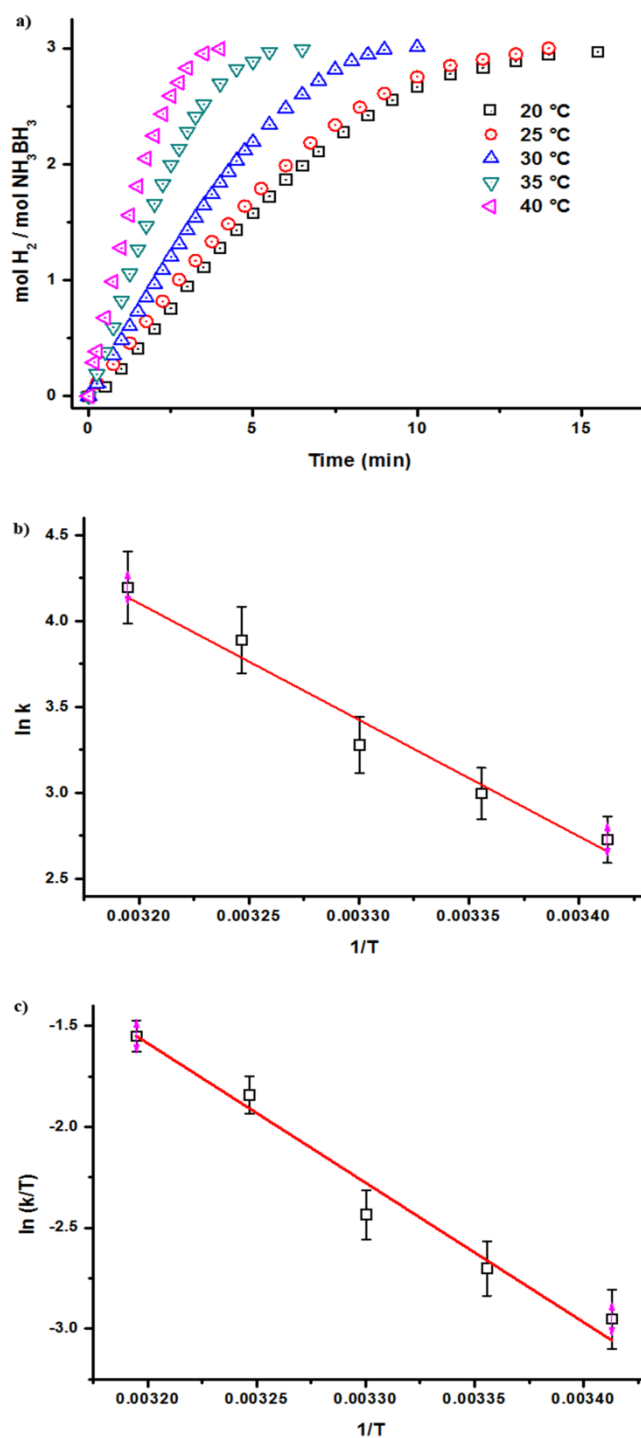


Figure 26. a) Plots of mol H_2 evolved per mole of AB *versus* time for the catalytic methanolysis of AB at various temperatures in the range of 20 – 40 °C keeping the concentration of substrate at $[\text{AB}] = 200 \text{ mM}$ and rhodium at $[\text{Rh}] = 0.406 \text{ mM}$ (20.0 mg Rh(III)/nanoHAP, 2.09 wt.%) as well as the $[\text{TBAP}] / [\text{Rh}]$ ratio at 2.0 constant in 10.0 mL methanol. b) Arrhenius Plot c) Eyring Plot.

5.1.2.2. Catalytic Lifetime and Recyclability Test of Rhodium(0) Nanoparticles Supported on Hydroxyapatite Nanospheres and Further Stabilized by Dihydrogen Phosphate Ions in Hydrogen Generation From the Methanolysis of Ammonia Borane

The catalytic lifetime experiment of Rh(0)/nanoHAP was performed in order to measure the total turnover number (TTON) for hydrogen generation from the methanolysis of AB at 25.0 ± 0.5 °C. Such a lifetime experiment was started with 10.0 mL solution of 5.5 mg Rh(III)/nanoHAP (rhodium loading of 2.09% wt., 1.1 mmol Rh), 400 mM AB plus [TBAP]/[Rh] ratio of 2.0. Hydrogen generation was continued by adding a new batch of AB into the solution until no more H₂ gas liberated and catalyst deactivated. The changes in turnover number (TON) and turnover frequency (TOF) in the course of reaction can be easily observed in Figure 27. Rh(0)/nanoHAP provide 26,000 turnovers in the hydrogen generation from the methanolysis of AB at 25.0 ± 0.5 °C before deactivation. Expectedly, the TOF value declines as the reaction continues and ultimately reaches minimum because of viscose form of reaction solution due to the continuous addition of AB or deactivating effect of boron containing by products. The initial turnover frequency (TOF) value is 147 min^{-1} (mol H₂/mol Rh×min) for Rh(0)/nanoHAP in the catalytic methanolysis of AB at 25.0 ± 0.5 °C. This value is higher than other TOF value reported in the literature for same reaction using rhodium catalyst such as RhCl₃ (TOF = 100 min^{-1}) [29], zeolite confined rhodium(0) nanoparticles (TOF = 30 min^{-1}) [41].

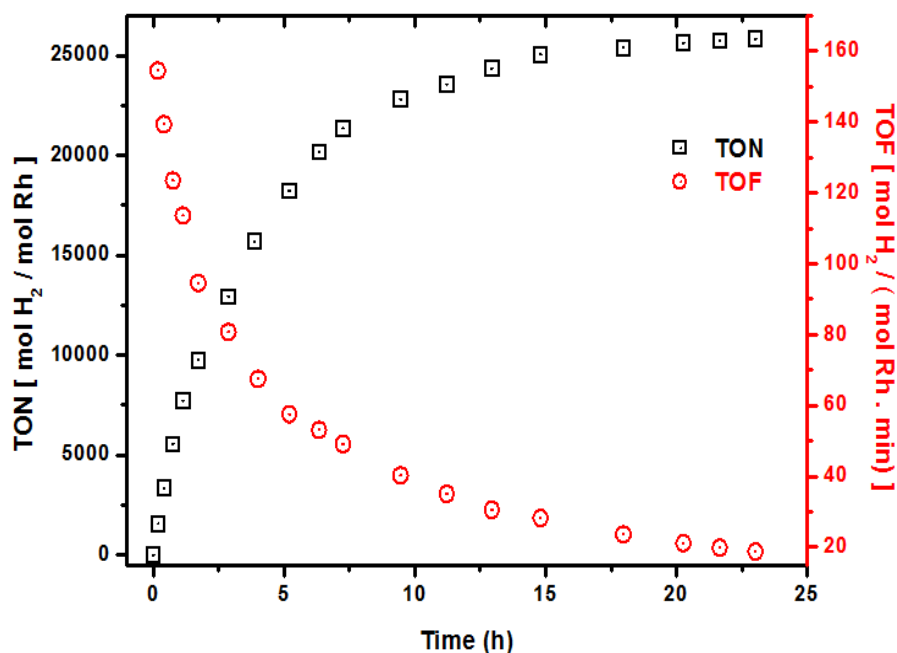


Figure 27. Plot of total turnover number (TTO) or turnover frequency *versus* time for the methanolysis of AB with 10.0 mL solution of 5.5 mg Rh(III)/nanoHAP (rhodium loading of 2.09 wt. %, 1.1 $\mu\text{mol Rh}$), 400 mM AB (for each run) plus [TBAP]/[Rh] ratio at 2.0

A similar procedure as the lifetime experiment was followed in recyclability test for Rh(0)/nanoHAP in hydrogen generation from the methanolysis of AB. After complete methanolysis of AB (64 mg, 2.0 mmol), the catalyst was kept in the reaction solution and a new batch of AB (64 mg) was added to the reaction medium at 25.0 ± 0.5 °C. The catalyst retains 21% of its initial activity at the sixth run. The decrease in catalytic activity in successive runs is likely caused by the increase in viscosity of the solution during methanolysis and probably due to the passivation of nanoparticles surface by increasing amount of methoxyborate, which might decrease the accessibility of active sites [111,112].

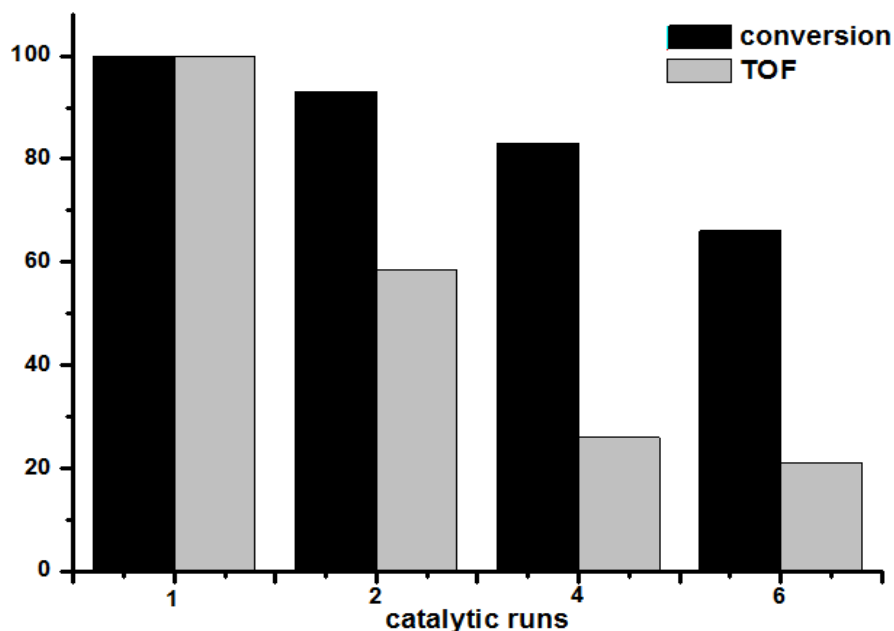


Figure 28. Catalytic activity and conversion of AB *versus* number of catalytic runs for Rh(0)/nanoHAP catalyst (38.5 mg Rh(0)/nanoHAP, 2.09 wt.% , [Rh] = 0.782 mM, [AB] = 200 mM at 25.0 ± 0.5 °C.)

5.1.2.3. Leaching Test for Rhodium(0) Nanoparticles Supported on Hydroxyapatite Nanospheres and Further Stabilized by Dihydrogen Phosphate Ions in the Methanolysis of Ammonia Borane

In order to check whether hydrogen generation from the methanolysis of AB is completely ceased by the removal of catalytically active Rh(0)/nanoHAP from reaction solution, leaching test were performed in the methanolysis of AB (200 mM) under the same reaction conditions. Figure 29 depicts the plots of mol of H₂ evolved per mole of AB *versus* time during the catalytic methanolysis of 200 mM AB starting with 0.406 mM Rh (20.0 mg Rh(III)/nanoHAP, 2.09 wt.%) plus [TBAP]/[Rh] ratio of 2.0 in 10.0 mL methanol and the filtrate solution obtained by filtration of solid materials after methanolysis at 25.0 ± 0.5 °C. Filtrate solution has no catalytic activity in the methanolysis of AB. In addition, filtrate of reaction solution was further analyzed by ICP after the first run of methanolysis of AB in order to detect

the amount of rhodium leached from the surface of hydroxyapatite into the reaction solution during methanolysis. ICP results showed that the rhodium concentration in filtrate is less than 0.05 ppm, which is negligible compared to the initial rhodium concentration of 0.406 mM in the reaction solution. Therefore, it can be concluded that Rh(0)/nanoHAP are kinetically competent and heterogeneous catalyst in hydrogen generation from the methanolysis of AB.

5.1.2.4. Carbon Disulfide (CS₂) Poisoning Heterogeneity Test for Rhodium(0) Nanoparticles Supported on Hydroxyapatite Nanospheres and Further Stabilized by Dihydrogen Phosphate Ions in the Methanolysis of Ammonia Borane

Carbon disulfide poisoning experiment was performed to test the heterogeneity of catalysis. The strong binding of poison to the metal centre can block the access of the substrate to the active site [113,114]. In our poisoning experiment, after the liberation of 40% hydrogen from the methanolysis of AB (200 mM) catalyzed by 0.406 mM Rh (20.0 mg Rh(III)/nanoHAP, 2.09 wt.%) in 10.0 mL methanol, when the catalytically active rhodium(0) nanoparticles were certainly formed, 0.2 equivalent CS₂ per mole of catalyst was added into reaction solution at 25.0 ± 0.5 °C. Figure 29 exhibits the plots of mol H₂ evolved per mole of AB *versus* time for the catalytic methanolysis of AB (200 mM) catalyzed by Rh(0)/nanoHAP ([Rh]=0.406 mM) with or without 0.2 equivalent CS₂ added into reaction solution at 25.0 ± 0.5 °C. The complete cessation of catalytic methanolysis of AB upon addition of CS₂ is a compelling evidence for the heterogeneity of Rh(0)/nanoHAP in the methanolysis of AB.

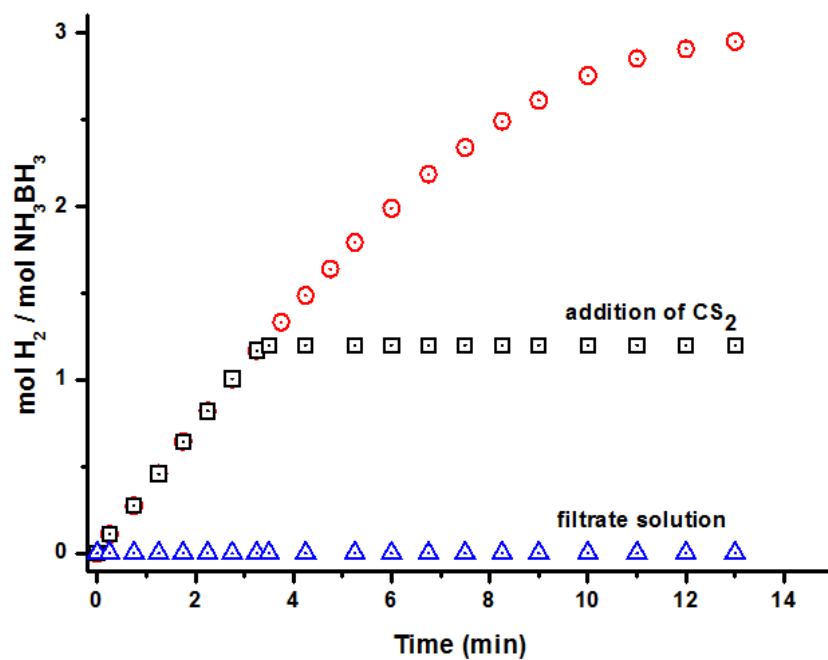


Figure 29. Plots of mol of H₂ evolved per mole of AB *versus* time for the methanolysis of 200 mM AB catalyzed by 0.406 mM Rh (20.0 mg Rh(III)/nanoHAP, 2.09 wt.%) plus [TBAP] / [Rh] ratio of 2.0 with (square □) or without (circle, ○) addition of CS₂ in 10.0 mL methanol, and the filtrate solution obtained from the filtration of active catalyst after the methanolysis of AB at 25.0 ± 0.5 °C. (triangle Δ)

5.2. Preparation and Characterization of Rhodium(0) Nanoparticles Supported on Nanosilica and Investigation of Their Catalytic Activities in Hydrogen Generation From the Methanolysis of Ammonia Borane

The second part of this dissertation covers the preparation and characterization of nanosilica stabilized rhodium(0) nanoparticles and examination of their catalytic activity in hydrogen generation from the methanolysis of AB. The particle size of silica is in the nanoregime with average diameter of 12 nm. The chemical compound silicon dioxide, also known as silica, is an oxide of silicon with a chemical formula of SiO_2 .

The following key properties are the reasons why silica can be preferred as support material [115,116];

- i) inert to chemical reactions with solvent
- ii) high stability even at high temperatures and pressures
- iii) easily functionalized due to high surface reactivity
- iv) excellent porosity
- v) low cost and wide accessibility

5.2.1. Preparation and Characterization of Rhodium(0) Nanoparticles Supported on Nanosilica

The formation of rhodium(0) nanoparticles supported on nanosilica ($\text{Rh}(0)/\text{nanoSiO}_2$) and concomitant hydrogen generation from the methanolysis of AB occur in the same reaction flask. First, rhodium(II) octanoate dimer was stirred with nanosilica powder in methanol for 3h, hence the suspension of Rh(II) ions impregnated on nanosilica ($\text{Rh}(\text{II})/\text{nanoSiO}_2$) were obtained. Then, AB solution was injected into the reaction flask containing a suspension of $\text{Rh}(\text{II})/\text{nanoSiO}_2$ precatalyst in methanol; thus the reduction of Rh(II) ions to rhodium(0) nanoparticles and hydrogen generation from the methanolysis of AB started at the same time. After a short induction period, the colour of solution altered from pale blue to black indicating the formation of rhodium(0) nanoparticles in methanol solution and then, fast hydrogen generation from the methanolysis of AB launched. In such an experiment, that the impregnation of Rh(II) ions on nanosilica and then, the *in situ* formation of $\text{Rh}(0)/\text{nanoSiO}_2$ were performed in the same medium provides less effort in the catalyst preparation. $\text{Rh}(0)/\text{nanoSiO}_2$ are quite active catalyst in hydrogen generation from the methanolysis of AB, then the active catalyst were

isolated from the reaction solution by centrifugation and then, characterized by a set of advanced analytical techniques.

The first characterization technique was powder XRD to check whether there are any changes in the framework lattice or crystallinity of the support material, nanosilica. The XRD patterns of nanosilica and Rh(0)/nanoSiO₂ are presented in Figure 30. The comparison of both patterns shows that there is no noticeable alternation in intensities or in the positions of main Bragg peaks of silica. This result implies the preserving of both crystallinity and the lattice of silica after the preparation of Rh(II)/nanoSiO₂ and the formation of Rh(0)/nanoSiO₂ during methanolysis of AB. The extra peak indicating the rhodium(0) nanoparticles could not be observed in the latter pattern because of low rhodium loading on nanosilica sample.

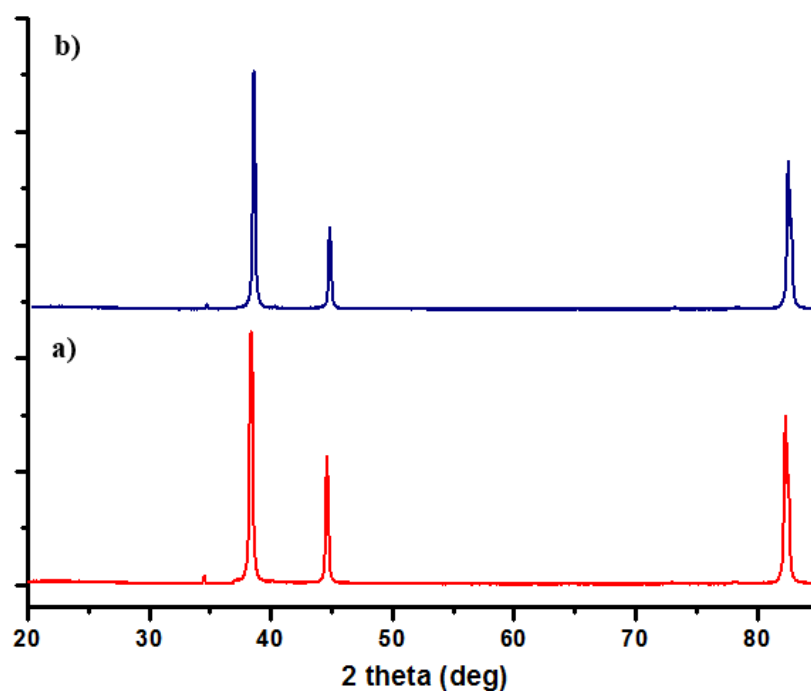


Figure 30. Powder X-ray diffraction (PXRD) patterns of a) silica nanopowder (nanoSiO₂), b) rhodium(0) nanoparticles supported on nanosilica (Rh(0)/nanoSiO₂) with rhodium loading of 3.0% wt. Rh.

TEM analysis was performed in order to get information about morphology and particle size of Rh(0)/nanoSiO₂ sample. Figure 31 depicts the TEM images of Rh(0)/nanoSiO₂ with various rhodium loading (0.50, 1.0, 2.0, 3.0 and 5.0 % wt. Rh) isolated after catalytic methanolysis of AB. TEM results indicate that rhodium(0) nanoparticles were uniformly dispersed on the surface of nanosilica. Additionally, Figure 31f exhibits the plot of particle size of rhodium(0) nanoparticles *versus* the rhodium loading (% wt.) of Rh(0)/nanoSiO₂ samples in which there is an increasing trend in particle size in the range of 3.4 – 4.9 nm with increasing rhodium loading on samples. TEM-EDX analysis of the samples were also performed in order to prove the existence of rhodium(0) nanoparticles on the nanosilica structure. The EDX spectrum (Figure 32) taken during TEM observation from many different areas of Rh(0)/nanoSiO₂ samples also confirms that rhodium is the only element detected with framework elements of nanosilica (Si and O)..

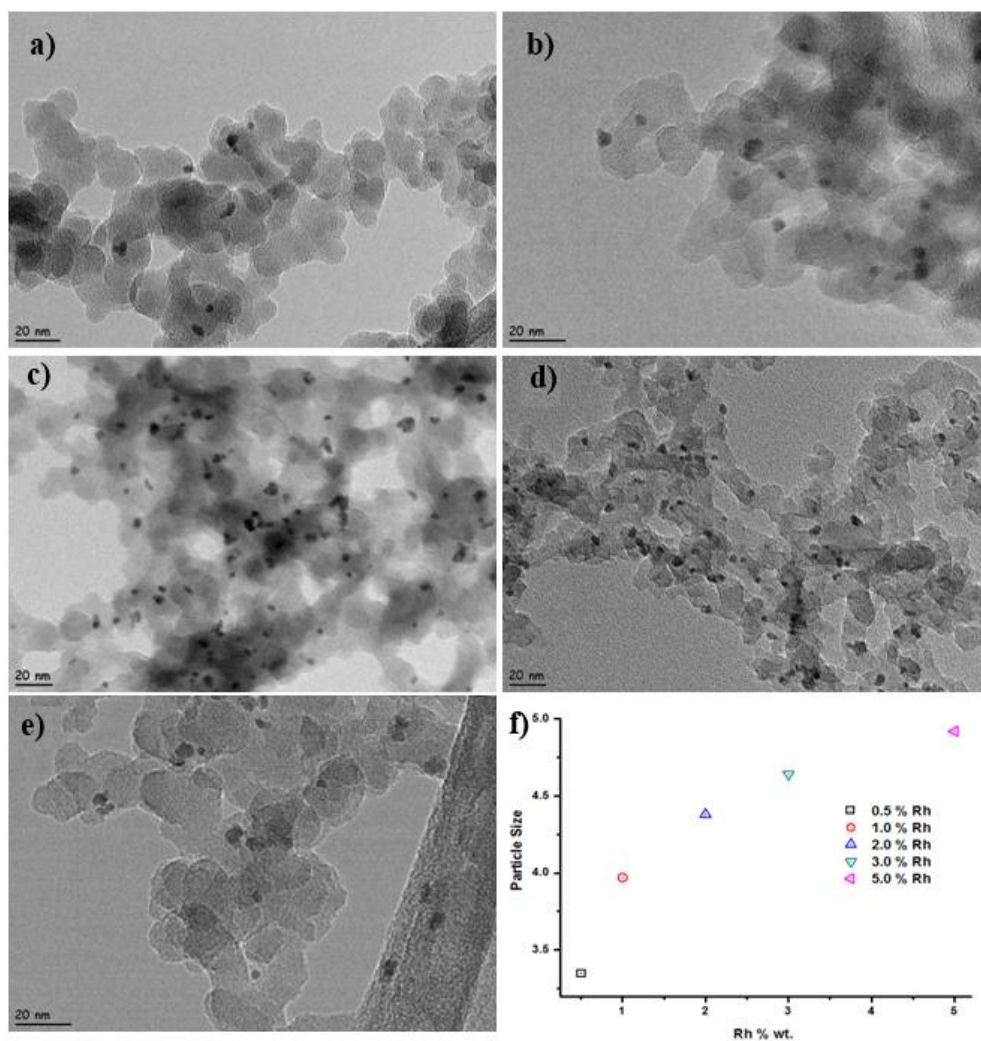


Figure 31. TEM images of rhodium(0) nanoparticles supported on nanosilica with different rhodium loading a) 0.5, b) 1.0, c) 2.0, d) 3.0 and e) 5.0% wt. Rh after catalytic methanolysis reaction performed starting with 200 mM AB catalyzed by desired amount of of rhodium(0) nanoparticles supported on nanosilica at 25.0 ± 0.5 °C. f) the plot of percentage rhodium loading *versus* particle size.

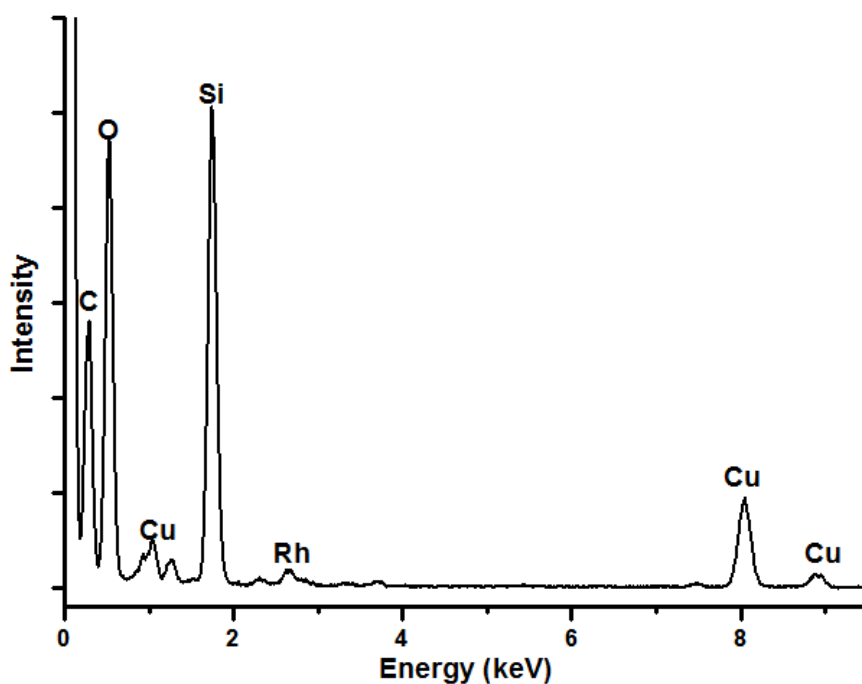


Figure 32. TEM-EDX spectrum of Rh(0)/nanoSiO₂ obtained after the catalytic methanolysis of AB.

XPS studies of Rh(0)/nanoSiO₂ sample were performed to analyze the chemical composition of sample and oxidation state of rhodium. The survey scan spectrum of Rh(0)/nanoSiO₂ sample with a rhodium loading of 5.0 %wt. Rh, given in Figure 33a shows the presence of rhodium in addition to the framework elements of nanosilica as indicated by TEM-EDX. The high resolution Rh 3d XPS spectrum of same Rh(0)/nanoSiO₂ sample is demonstrated in Figure 33b. There are two prominent bands observed at 306.7 and 311.8 eV attributed to Rh(0) 3d_{5/2} and Rh(0) 3d_{3/2}, respectively, by comparison to the values of metallic rhodium [102,117]. Two additional higher energy peaks at 309.1 and 314.8 eV show the presence of rhodium in higher oxidation state, likely in the form of oxide [118,119], which may arise from the oxidation of rhodium(0) nanoparticles when exposed to air for a few minutes during XPS sampling.

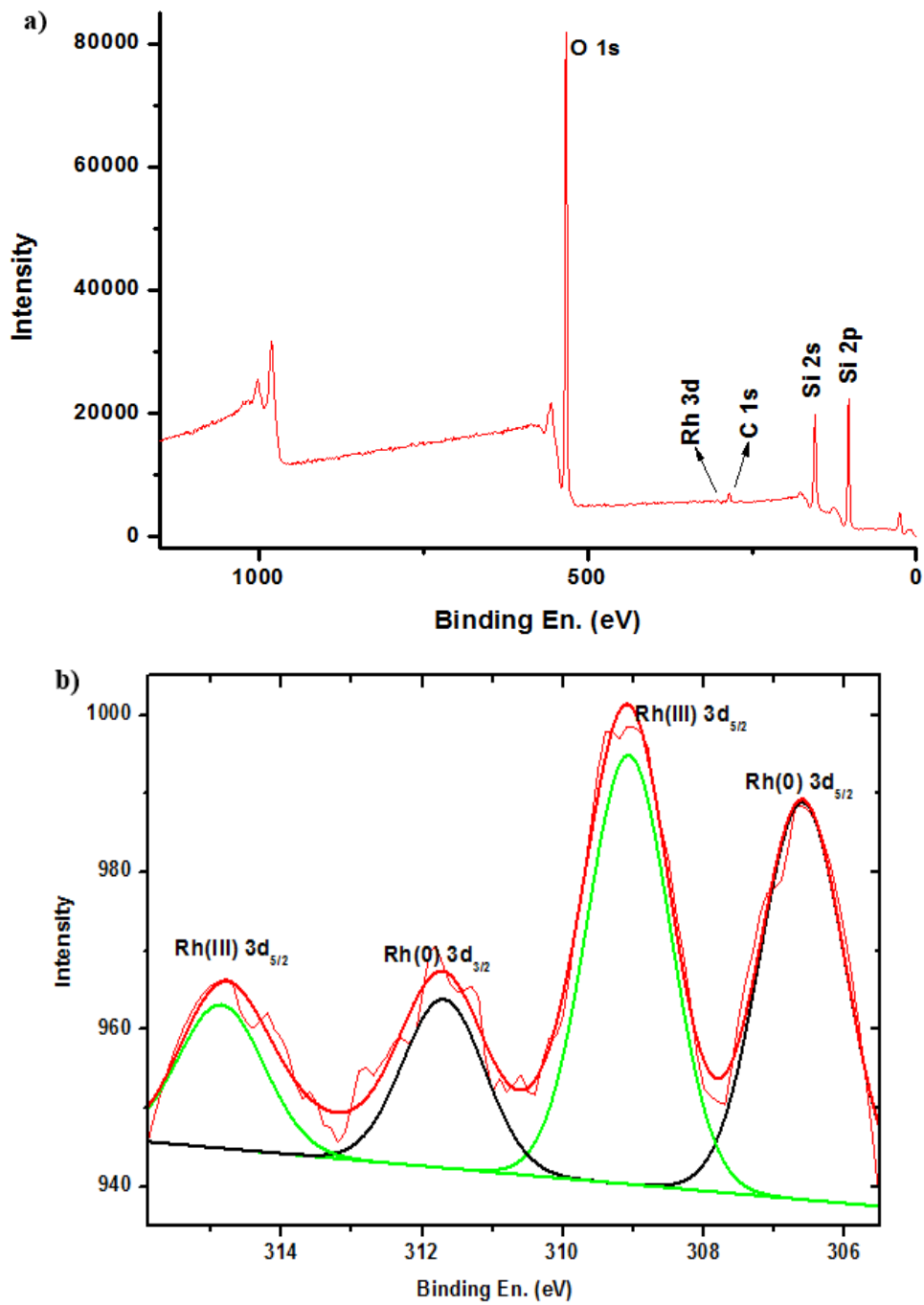


Figure 33. a) X-ray photoelectron (XPS) survey scan spectrum, a) high resolution Rh 3d XPS spectrum of Rh(0)/nanoSiO₂ with a rhodium loading of 5.0% wt. Rh.

N₂ adsorption-desorption analysis was carried out for both nanosilica and Rh(0)/nanoSiO₂ in order to determine BET surface areas of each materials. On passing from nanosilica to Rh(0)/nanoSiO₂, surface area is relatively increased by 35.6 m²g⁻¹ (from 246.8 to 282.4 m²g⁻¹). The increase in the BET surface area demonstrates the existence of rhodium(0) nanoparticles on the surface of nanosilica.

5.2.2. The Catalytic Activities of Rhodium(0) Nanoparticles Supported on Nanosilica in Hydrogen Generation From the Methanolysis of Ammonia Borane

5.2.2.1. Kinetic Studies and Determination of Activation Parameters for the Methanolysis of Ammonia Borane Catalyzed by Rhodium(0) Nanoparticles Supported on Nanosilica

Rh(0)/nanoSiO₂ was *in-situ* formed from the reduction of Rh(II)/nanoSiO₂ precatalyst during hydrogen generation from the methanolysis of AB at room temperature. Upon injecting AB solution into reaction solution containing a suspension of Rh(II)/nanoSiO₂ in methanol, the reduction of Rh(II) ions and hydrogen liberation from the methanolysis of AB launched simultaneously. The formation of rhodium(0) nanoparticles and synchronical hydrogen evolution from the methanolysis of AB were tracked by monitoring the volume of H₂ generated and then, converting into the equivalent H₂ per mole of AB, using the known 3:1 H₂/AB stoichiometry (Eqn. 1). Figure 34 shows the plots of mol H₂ evolved per mole of AB *versus* time for the catalytic methanolysis of AB starting with 200 mM AB and 50 mg of Rh(II)/nanoSiO₂ (1.0 wt.% Rh, [Rh] = 0.49 mM) in 10 mL methanol at 25.0 ± 0.5 °C. The color of reaction solution changed from pale blue to black within 1.5 min then, hydrogen production started immediately and proceeded almost linearly until the liberation of 3.0 equivalents H₂ per mole AB. The change in color and sigmoidal shape of hydrogen generation curve demonstrate the reduction of Rh(II) ions and formation of rhodium(0) nanoparticles with a 2- step, nucleation and autocatalytic surface growth mechanism of nanoparticle formation [120,121].

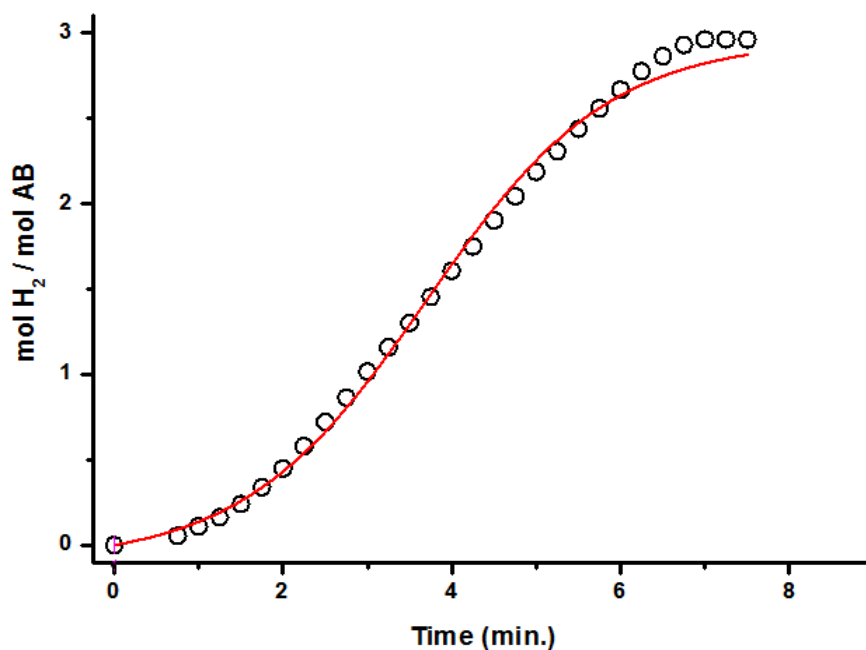
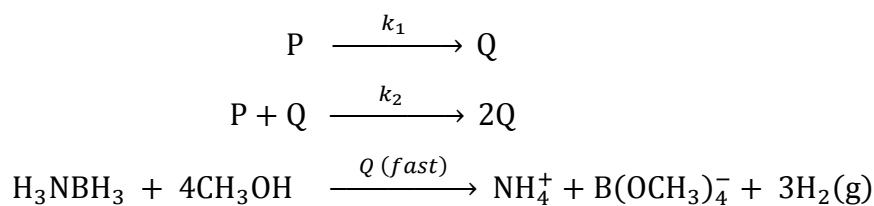


Figure 34. Plot of mol H₂ evolved per mole of AB *versus* time for the catalytic methanolysis of AB starting with 200 mM AB and 50 mg of Rh(II)/nanoSiO₂ (1.0 wt.% Rh, [Rh]= 0.49 mM) in 10 mL methanol at 25.0 ± 0.5 °C.

The formation kinetics of rhodium(0) nanoparticles catalyst can be determined using the hydrogen generation as reporter reaction [120,121,122]. The Finke-Watzky 2-step mechanism (nucleation and autocatalytic growth) for the nanoparticle formation is given in Scheme 1, where P stands for the added precursor Rh(II)/nanoSiO₂ and Q for the growing rhodium(0) nanoparticles.



Scheme 1. Illustration of the methanolysis of AB as reporter reaction: P is the precursor rhodium(II) ions impregnated on the porous nanosilica and Q is the growing Rh(0)_n nanoparticles catalyst.

The fitting of hydrogen generation data to 2-step mechanism gives valuable information about the kinetics of rhodium(0) nanoparticle formation in the case of faster rate of hydrogen generation than that of nanoparticle formation. Sigmoidal kinetics curve seen in Figure 34 fit well to the function given in Eqn. 4.

$$[\text{AB}]_t = \frac{\frac{k_1}{k_2} + [\text{AB}]_0}{1 + \frac{k_1}{k_2[\text{AB}]_0} \exp(k_1 + k_2[\text{AB}]_0)t} \quad (4)$$

Here, k_1 is the rate constant for the slow, continuous nucleation, k_2 is the rate constant for the autocatalytic surface growth, $[\text{AB}]_0$ and $[\text{AB}]_t$ are the concentration of AB at time 0 and t , respectively. The sigmoidal hydrogen generation curve and its curve fit to slow, continuous nucleation, followed by autocatalytic surface growth kinetics indicate that rhodium(0) nanoparticles are formed from a soluble precursor complex in the presence of reducing agent, AB. The rate constants for each step could be determined to be $3.0 \times 10^{-2} \text{ min}^{-1}$ for k_1 and $1.2 \times 10^2 \text{ M}^{-1} \text{ min}^{-1}$ for k_2 from the nonlinear least square curve-fit in Figure 34. The values of k_2 has been corrected mathematically for stoichiometry factor of $[\text{AB}]/[\text{cat}]$ and determined to be 407 [122], but not for

the “scaling factor”; it means that this correction is not related to the changing the number of rhodium atoms on the growing surface of metal. These rate constants are for slow, continuous nucleation and autocatalytic surface growth reaction of rhodium(0) nanoparticles, respectively, starting with 200 mM AB and 50 mg of Rh(II)/nanoSiO₂ (1.0 wt.% Rh, [Rh] = 0.49 mM) in 10 mL methanol at 25.0 ± 0.5 °C. It is emphasized that k_1 and k_2 are not directly correlated to each other because each represents the rate constants of two different reactions.

In order to examine the effect of support on the catalytic activity and stability of rhodium(0) nanoparticles, a comparative test was performed starting with rhodium(II) octanoate dimer either alone or impregnated on nanosilica. Figure 35 depicts the plots of mol H₂ evolved per mole of AB *versus* time for the catalytic methanolysis of AB starting with 200 mM AB plus either 50 mg of Rh(II)/nanoSiO₂ (1.0 wt.% Rh, [Rh] = 0.49 mM) or 1.9 mg of rhodium(II) octanoate (0.49 mM Rh) in 10 mL methanol at 25.0 ± 0.5 °C. Even though the initial activities of both catalysts appear to be same, the rhodium(0) nanoparticles without support material lose catalytic activity rapidly. Additionally, in the case of rhodium(0) nanoparticles in the absence of support, the bulk rhodium metal formation is observed at the end of methanolysis. These results refer that support material provides stabilization for rhodium(0) nanoparticles and prevents the aggregation to bulk metal. Hence, the nanosilica support is required to obtain stable and catalytically active rhodium(0) nanoparticles.

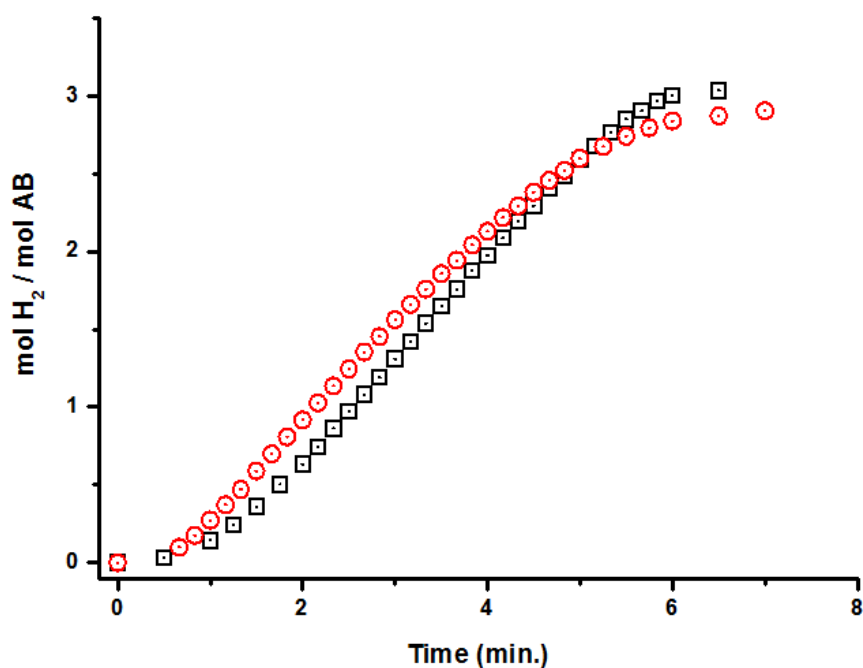


Figure 35. Plots of mol H₂ evolved per mole of AB *versus* time for the catalytic methanolysis of AB starting with 200 mM AB plus either (black squares, □) 50 mg of Rh(II)/nanoSiO₂ (1.0 wt.% Rh, [Rh] = 0.49 mM) or (red circles, ⊙) 1.9 mg of rhodium(II) octanoate (0.49 mM Rh) in 10 mL methanol at 25.0 ± 0.5 °C.

Rhodium(0) nanoparticles supported on nanosilica are quite active catalyst in hydrogen generation from the methanolysis of AB even in low rhodium concentration at room temperature. Figure 36a exhibits the plots of mol of H₂ evolved per mole of AB *versus* time during the catalytic methanolysis performed starting with 200 mM AB in various rhodium loading, thus in various rhodium concentration at 25.0 ± 0.5°C. In all cases, there is a short induction period less than 2 min and then, hydrogen evolution continues linearly until 3.0 equivalents hydrogen generated. That the catalytic activity remains unchanged during surface growth of rhodium(0) nanoparticles demonstrates the structure insensitivity of methanolysis reaction. All the experimental curves having sigmoidal shape fit well to the 2-step mechanism, which enables us to determine the rate constants k_1 of the slow, continuous nucleation and k_2 of the autocatalytic surface growth for the formation of

rhodium(0) nanoparticles catalyst from rhodium(II) ions during the methanolysis of AB. The large value of k_2/k_1 indicates high level of kinetic control for the rhodium(0) nanoparticles formation from the reduction of rhodium(II) ions (Table 1).

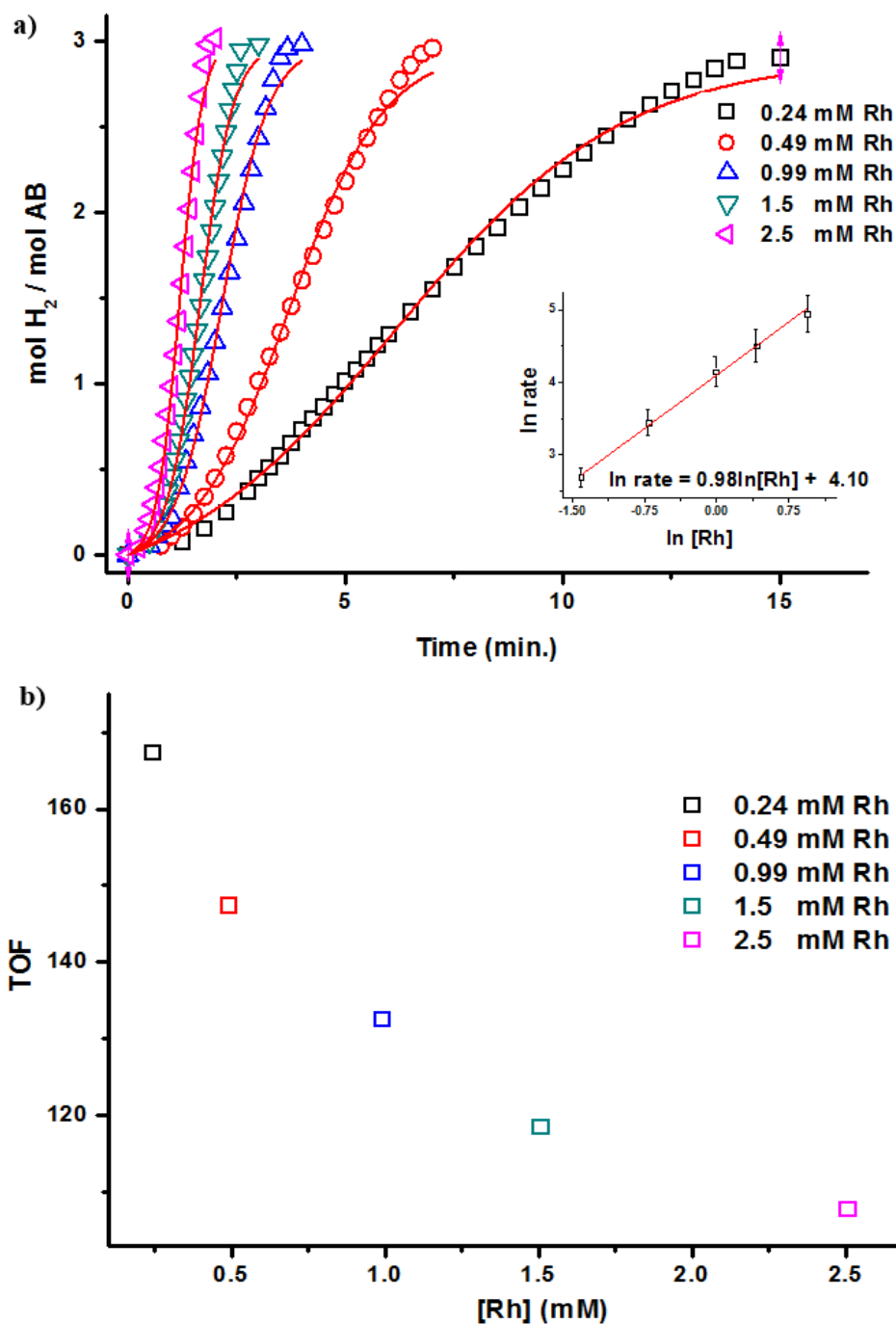


Figure 36. a) Plots of mol H_2 evolved per mole of AB *versus* time for methanolysis of 200 mM AB in different metal concentrations ($[\text{Rh}] = 0.24, 0.49, 0.99, 1.5, 2.5$ mM, each prepared using metal loading of 0.50, 1.0, 2.0, 3.0, 5.0% wt. Rh, respectively) at 25.0 ± 0.5 °C. Inset: Plot of hydrogen generation rate *versus* the concentration of rhodium (both in logarithmic scale.). b) Inverse dependence of initial TOF value on the initial precatalyst Rh concentration.

Table 1. The rate constants k_1 of the slow, continuous nucleation, $P \rightarrow Q$, and k_2 of the autocatalytic surface growth, $P + Q \rightarrow 2Q$, for the formation of rhodium(0) nanoparticles catalyst from the reduction of rhodium(II) ions during the methanolysis of AB (200 mM) starting with Rh(II)/nanoSiO₂ with different rhodium loading, rhodium concentrations, hydrogen generation rates, turnover frequency (TOF) values, and the TOF values corrected for the number of rhodium atoms on the surface of nanoparticles for the methanolysis of AB at 25.0 ± 0.5 °C

wt.%Rh	Particle size (nm)	Number of Rh atoms in NP	Number of Rh atoms on surface	[Rh] (mM)	k_1 (min ⁻¹)	k_2 (M ⁻¹ min ⁻¹)	k_2/k_1	H ₂ generation rate (mmol.min ⁻¹)	TOF (min ⁻¹)	TOF _{corrected} (min ⁻¹)
0.50	3.4 ± 0.4	1494	498	0.24	$(3.35 \pm 0.16) \times 10^{-2}$	97.8 ± 3.1	2.92×10^3	0.55	168	504
1.0	4.0 ± 1.0	2432	689	0.49	$(3.03 \pm 0.24) \times 10^{-2}$	121.1 ± 3.9	4.00×10^3	1.17	147	519
2.0	4.4 ± 0.7	3237	834	0.99	$(3.26 \pm 0.38) \times 10^{-2}$	124.2 ± 4.6	3.81×10^3	2.38	133	516
3.0	4.6 ± 1.1	3699	911	1.5	$(3.33 \pm 0.36) \times 10^{-2}$	115.7 ± 3.7	3.47×10^3	3.37	119	483
5.0	4.9 ± 1.8	4471	1034	2.5	$(4.11 \pm 0.64) \times 10^{-2}$	97.2 ± 4.2	2.37×10^3	5.24	108	467

The hydrogen generation rate was determined from the linear portion of each plot in Figure 36a and converted to the turnover frequency (TOF) of rhodium(0) nanoparticles in hydrogen generation from the methanolysis of AB at 25.0 ± 0.5 °C. The TOF values, defined per rhodium present in the catalyst as usual [123], as well as TOF values corrected for the number of rhodium atoms on the surface of nanoparticle, and hydrogen generation rates for the methanolysis of AB in different initial concentration of rhodium at 25.0 ± 0.5 °C were also listed in Table 1. Rh(0)/nanoSiO₂ sample with rhodium loading of 0.5 wt.% Rh provides the highest catalytic activity with an initial TOF = 168 min^{-1} (504 min^{-1} corrected for surface rhodium atoms, Table 1) ever reported for hydrogen generation from the methanolysis of AB at 25.0 ± 0.5 °C. Following equations were used to calculate the number of rhodium atoms in nanoparticles as well as rhodium atom on the surface of nanoparticles. All corrected TOF values were calculated by using the following equations;

Number of rhodium atoms in nanoparticles [124]:

$$n = \frac{\left(N_0 \rho \left(\frac{4}{3}\right) \pi \left(\frac{D}{2}\right)^3\right)}{W} \quad (5)$$

where;

n= number of rhodium atoms

$N_0 = 6.022 \times 10^{23} \text{ mol}^{-1}$

D= diameter of rhodium nanoparticles

W= atomic weight of rhodium ($102.91 \text{ g.mol}^{-1}$)

ρ = room temperature density of rhodium (12.41 gcm^3)

Number of rhodium atoms on the surface of nanoparticle:

$$n_s = \frac{4\pi \left(\frac{D}{2}\right)^2}{(2r)^2} \quad (6)$$

r= atomic radius of rhodium (0.135 nm)

Corrected TOF = TOF / fraction of surface Rh atoms (7)

It is noteworthy that there is an inverse correlation between TOF values and initial concentration of rhodium in the Rh(0)/nanoSiO₂ catalyst, down to

value of 108 min^{-1} for the 5.0 % wt. Rh. The inverse dependence of TOF on the initial concentration of Rh(0)/nanoSiO₂ samples is shown in Figure 36b. In fact, it is anticipated that the true TOF should be constant for a given metal containing catalyst in a given reaction under specified reaction conditions, therefore, understanding this inverse dependence of the TOF on precatalyst concentration is important [125]. However, this inverse correlation has been mentioned many times with some explanations in literature [126,127,128]. One of the mechanisms suggested for the observed inverse relation between the TOF and catalyst concentration correlates the variation in the catalytic activity with the particles size in size specific reactions [129]. The use of lower concentration of precatalyst forms smaller particles and higher catalytic activity is observed for those smaller particles for some reactions [130], then this size-specific catalytic activity can produce an inverse TOF versus precatalyst concentration dependence. In structure insensitive reactions such as ours, the explanation would be straightforward: the catalytic activity per metal atom is expected to decrease as the fraction of surface sites over the total metal atoms decreases with the increasing particle size. The TOF value of Rh(0)/nanoSiO₂ in hydrogen generation from the methanolysis of AB decreases as the particle size of the rhodium(0) nanoparticles increases with the increasing initial concentration of rhodium (Figure 31f and Figure 36b). However, when the TOF values are corrected for the number of rhodium atoms on the surface of nanoparticle (Table 1) the inverse dependence of the catalytic activity on the size of nanoparticles disappears, as the corrected TOF values are similar to each other within the experimental error. The disappearance of inverse dependence for the corrected TOF values is also compelling evidence that the inverse relation between the catalytic activity and the concentration of rhodium is indeed a size issue.

The inset graph represented in Figure 36a shows the plot of the hydrogen generation rate *versus* the initial rhodium concentration, both axes in logarithmic scale. The straight line of plot has a slope of $0.98 \approx 1.0$ specifying that the methanolysis of AB catalyzed by Rh(0)/nanoSiO₂ is first order with respect to rhodium concentration. The catalytic methanolysis of AB continues almost linearly after induction period in each experiment, thusly the methanolysis of AB is most likely zero order with respect to AB concentration.

The series of different temperature experiments were performed in order to determine activation parameters for the nucleation and autocatalytic surface growth of rhodium(0) nanoparticles on the surface of nanosilica as well as for the methanolysis of AB catalyzed by Rh(0)/nanoSiO₂. Figure 37a depicts the plots of mol H₂ evolved per mole of AB *versus* time for the methanolysis of AB starting with 0.49 mM Rh catalyst (1.0 wt.% Rh, 50 mg Rh(II)/nanoSiO₂) plus 200 mM AB substrate at various temperatures. All the experimental temperature kinetic data fit well the 2–step mechanism thus the rate constants of each step (k_1 and k_2) could be determined. Table 2 summarizes the results of rate constants of k_1 and k_2 as well the k_2/k_1 ratio. Activation energy for the nucleation and autocatalytic surface growth could be determined from the Arrhenius plots by using the values of rate constants k_1 and k_2 at various temperatures in Figure 37b and 37c, respectively: $E_a = 79 \pm 5$ kJ/mol for the nucleation and $E_a = 49 \pm 2$ kJ/mol for the autocatalytic surface growth. Activation energy values give an idea on the energy barrier for the slow nucleation and autocatalytic surface growth of metal(0) nanoparticles catalyst.

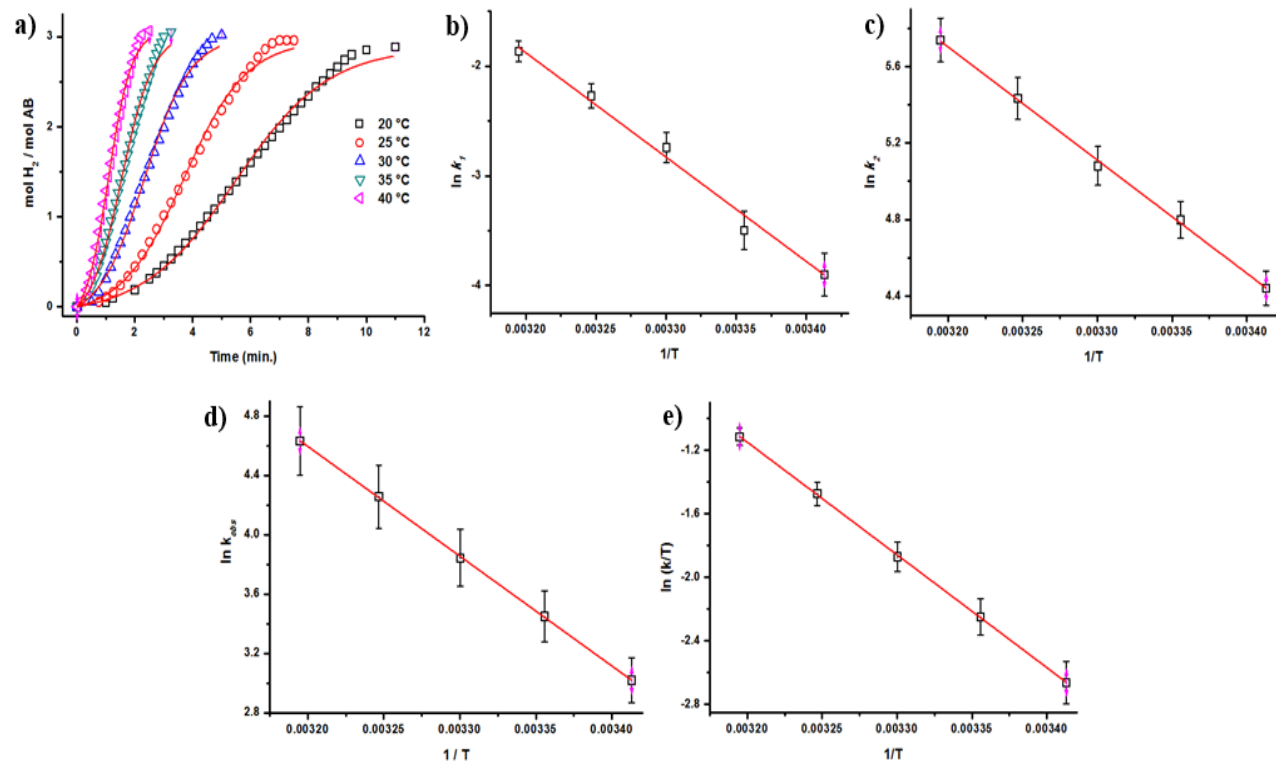


Figure 37. a) Plots of mol H₂ evolved per mole of AB *versus* time for the catalytic methanolsis of AB at various temperatures in the range of 20 – 40 °C keeping the concentration of substrate at [AB] = 200 mM and rhodium at [Rh] = 0.49 mM (1.0 wt. % Rh, 50 mg Rh(0)/nanoSiO₂), b) The Arrhenius plot for nucleation of rhodium(0) nanoparticles, c) The Arrhenius plot for the autocatalytic surface growth of rhodium(0) nanoparticles, d) The Arrhenius plot, e) The Eyring plot for Rh(0)/nanoSiO₂ catalyzed methanolsis of AB. [AB] = 200 mM, [Rh] = 0.49 mM (1.0 wt. % Rh, 50 mg Rh(0)/nanoSiO₂).

The slopes of the plots represented in Figure 37a were used to determine hydrogen generation rate, then, the reaction rate constants, k_{obs} and TOF values were calculated for each temperatures (Table 2). The increase in the temperature expectedly improves the rate of hydrogen generation from the methanolysis of AB. Besides, also TOF values increase with increasing temperature reaching a remarkable value of 468 min^{-1} (1625 min^{-1} corrected for the number of rhodium atoms on the surface of nanoparticle) in hydrogen evolution from the methanolysis of AB at 40°C catalyzed by Rh(0)/nanoSiO₂. The activation parameters for the catalytic methanolysis of AB were determined by using Arrhenius [109] and Eyring [110] plots depicted in Figure 37d and e respectively; the activation energy $E_a^{\text{app}} = 62 \pm 2 \text{ kJ/mol}$, the activation enthalpy $\Delta H^{\ddagger, \text{app}} = 59 \pm 2 \text{ kJ/mol}$, and the activation entropy $\Delta S^{\ddagger, \text{app}} = -18 \pm 4 \text{ J/mol.K}$.

Table 2. The rate constants k_1 of the slow, continuous nucleation, $P \rightarrow Q$, and k_2 of the autocatalytic surface growth, $P + Q \rightarrow 2Q$, for the formation of rhodium(0) nanoparticles catalyst from the reduction of rhodium(II) ions during the methanolysis of AB, hydrogen generation rates, k_{obs} values, turnover frequency (TOF) values, and the TOF values corrected for the number of rhodium atoms on the surface of nanoparticles for the methanolysis of AB starting with $[AB] = 200$ mM and $[Rh] = 0.49$ mM at different temperatures.

Temperature (°C)	k_1 (min^{-1})	k_2 ($\text{M}^{-1} \text{min}^{-1}$)	k_2/k_1	H_2 generation rate ($\text{mmol H}_2 \cdot \text{min}^{-1}$)	k_{obs} ($\text{mol H}_2 \cdot \text{molRh}^{-1} \cdot \text{s}^{-1}$)	TOF (min^{-1})	TOF _{corrected} (min^{-1})
20	$2.03 \times 10^{-2} \pm 1.34 \times 10^{-3}$	84.9 ± 2.2	4.19×10^3	0.77	1.39	92	325
25	$3.03 \times 10^{-2} \pm 2.45 \times 10^{-3}$	121.3 ± 3.9	4.01×10^3	1.17	2.46	147	519
30	$6.44 \times 10^{-2} \pm 4.36 \times 10^{-3}$	160.7 ± 5.2	2.50×10^3	1.70	4.10	246	869
35	$1.03 \times 10^{-1} \pm 6.39 \times 10^{-3}$	229.0 ± 7.1	2.22×10^3	2.57	6.23	380	1343
40	$1.55 \times 10^{-1} \pm 8.54 \times 10^{-3}$	310.7 ± 10.0	2.01×10^3	3.63	7.66	460	1625

5.2.2.2. Catalytic Lifetime of Rhodium(0) Nanoparticles Supported on Nanosilica in Hydrogen Generation From the Methanolysis of Ammonia Borane

The catalytic lifetime experiment of Rh(0)/nanoSiO₂ was performed in order to determine the total turnover number (TTON) and turnover frequency (TOF) provided by rhodium(0) nanoparticles in hydrogen generation from the methanolysis of AB before deactivation. Figure 38 gives the plots of TTON and TOF *versus* time for the methanolysis of AB starting with 10 mL suspension containing 0.99 mM Rh (50.0 mg Rh(0)/nanoSiO₂, 2.0 wt.% Rh,) and 400 mM AB at 25.0 ± 0.5 °C. Upon liberation of expected amount of H₂ gas, a new portion of AB was added into the reaction flask and hydrogen generation was monitored. The same procedure was repeated until no more H₂ gas was generated.

Total turnover number of Rh(0)/nanoSiO₂ was determined to be 10,000 in hydrogen generation from the methanolysis of AB at 25.0 ± 0.5 °C before deactivation. The initial turnover frequency value was calculated to be 168 min⁻¹ (652 min⁻¹ the value corrected for the number of rhodium atom on the surface of nanoparticle) for Rh(0)/nanoSiO₂ in hydrogen generation from the methanolysis of AB at 25.0 ± 0.5 °C.

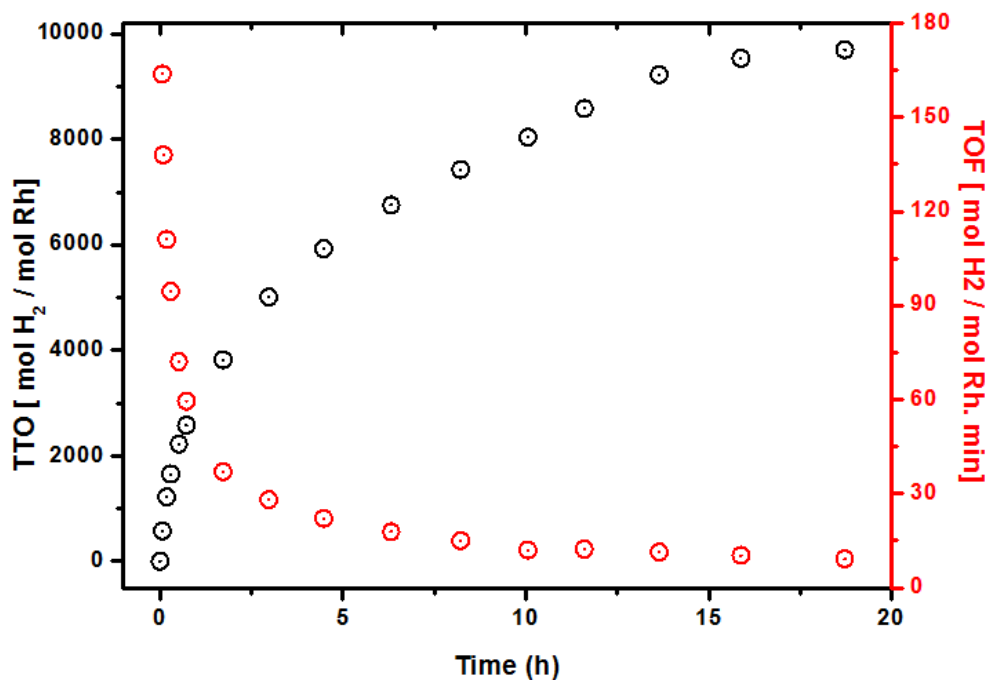


Figure 38. Plot of total turnover number (TTO) or turnover frequency *versus* time for the methanolysis of AB with 10 mL solution of 0.99 mM Rh (50.0 mg Rh(0)/nanoSiO₂, 2.0 wt.% Rh,) and 400 mM AB (for each run) at 25.0 ± 0.5 °C.

5.2.2.3. Leaching Test for Rhodium(0) Nanoparticles Supported on Nanosilica in the Methanolysis of Ammonia Borane

In order to examine whether hydrogen generation from the methanolysis of AB completely ceased by the removal of active catalyst Rh(0)/nanoSiO₂ from reaction solution, a control experiment was started with 200 mM AB plus 50 mg Rh(II)/nanoSiO₂ (1.0 % wt. Rh, [Rh] = 0.49 mM) in 10 mL methanol at 25.0 ± 0.5 °C. After the completion of catalytic methanolysis of AB, the reaction flask was opened under inert gas atmosphere; reaction solution was filtered to remove Rh(0)/nanoSiO₂, effectively. Filtrate was transferred into another reaction flask. A new batch of 200 mM AB was added to the reaction flask, hydrogen generation was monitored at 25.0 ± 0.5 °C. Filtrate solution exhibited no catalytic activity in the methanolysis of AB (Figure 39). The results of the leaching test confirm the retaining of

rhodium(0) nanoparticles within the nanosilica matrix (no rhodium passes into solution). It can also be concluded that Rh(0)/nanoSiO₂ are kinetically competent and heterogeneous catalyst in the methanolysis of AB. It is noteworthy that accurate measurement of the catalytic activity of isolated solid materials is not possible because of the notable materials loss during the isolation and redispersion. Therefore, a reliable reusability test could not be performed

5.2.2.4. Carbon Disulfide (CS₂) Poisoning Heterogeneity Test for Rhodium(0) Nanoparticles Supported on Nanosilica in the Methanolysis of Ammonia Borane

The heterogeneity of Rh(0)/nanoSiO₂ was checked by performing a CS₂ poisoning experiment. Due to the strong binding of poison to the metal center, the access of the substrate to the active site is blocked by poison [113,114]. In our poisoning experiment, after the liberation of 40% H₂ gas from the methanolysis of AB (200 mM) catalyzed by 0.49 mM Rh, when the catalytically active rhodium(0) nanoparticles were certainly formed, 0.20 equivalent CS₂ per mole of rhodium was swiftly injected to reaction flask, whereby the activity of Rh(0)/nanoSiO₂ was inhibited and hydrogen generation from the methanolysis of AB ceased immediately (Figure 39). The complete cessation of the catalytic methanolysis of AB upon CS₂ addition is a compelling evidence for the heterogeneity of Rh(0)/nanoSiO₂ in the methanolysis of AB.

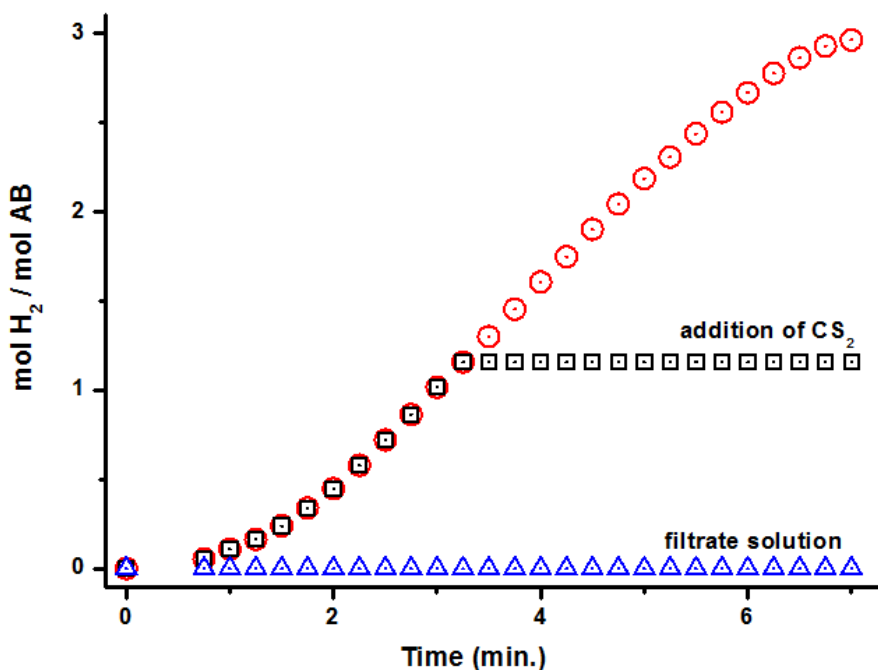


Figure 39. Plots of mol H₂ evolved per mole of AB *versus* time for the methanolysis of 200 mM AB catalyzed by Rh(0)/nanoSiO₂ (0.49 mM Rh, 1.0 wt. % Rh(0)/nanoSiO₂) with (square, ◻) and without (circle, ○) addition of 0.2 equiv. CS₂, and (triangle, Δ) the filtrate solution obtained from filtration of active catalyst after methanolysis of AB at 25.0 ± 0.5 °C.

5.2.2.5. Establishment of that Rhodium(0) Nanoparticles Supported on Nanosilica Catalyzed Methanolysis of Ammonia Borane is in the Kinetic Regime

An important question to be answered is whether the hydrogen generation from the methanolysis of AB is under mass transfer limitation or not [131]. To answer this question, a control experiment was performed starting with 200 mM AB and 0.49 mM Rh (50 mg Rh(II)/nanoSiO₂, 1.0 wt.% Rh) in 10 mL methanol at 25.0 ± 0.5 °C by varying the stirring rate. The results of the control experiment are given in Figure 40 which shows that stirring rate has essentially no effect on the rate of hydrogen generation from the methanolysis of AB at 25.0 ± 0.5 °C. This is a classic simple, but convincing, piece of evidence for the reaction being in the kinetic regime, not under the mass transfer limitations [132]. The observation that the hydrogen generation rate is independent of the stirring rate can be ascribed to small particle

size of support (smaller than 12 nm). Different from the other supported catalysts, Rh(0)/nanoSiO₂ doesn't precipitate when left in solution and remains as suspension for weeks. Thus, the rhodium(0) nanoparticles on the surface of small sized nanosilica are readily accessible by the substrate molecules, even in a nonstirred solution. Note that all the experiments in this study were performed under stirring at 1000 rpm.

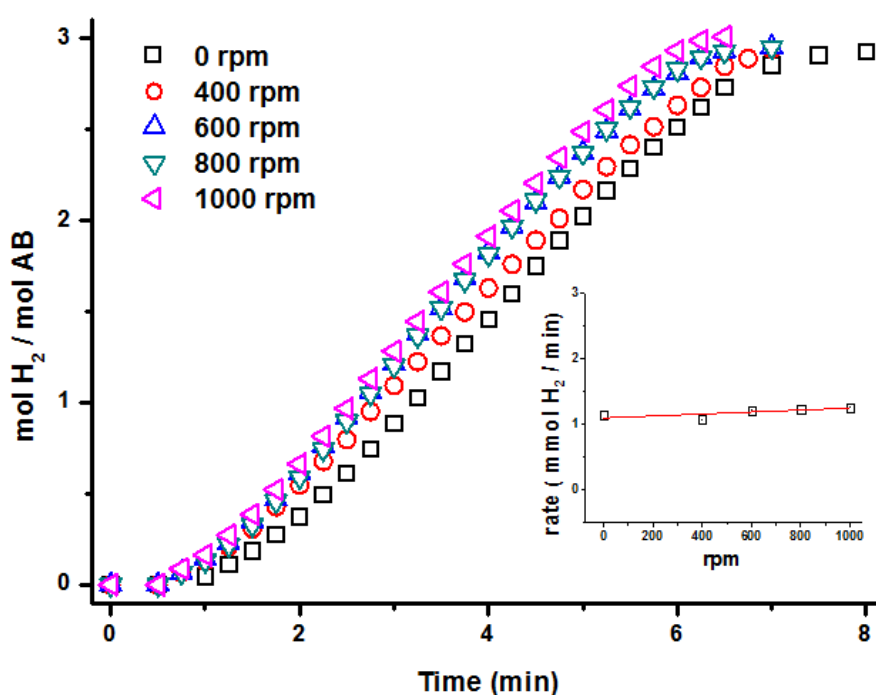


Figure 40. Plots of mol H₂ evolved per mole of AB *versus* time for the catalytic methanolysis of AB starting with 200 mM AB and 0.49 mM Rh (50 mg Rh(II)/nanoSiO₂, 1.0 wt.% Rh) in 10 mL methanol at 25.0 ± 0.5 °C at different stirring rate. The inset shows the plot of hydrogen generation rate *versus* the stirring rate.

5.3. Preparation and Characterization of Rhodium(0) Nanoparticles Supported on Nanoalumina and Investigation of Their Catalytic Activities in Hydrogen Generation from Methanolysis of Ammonia Borane

In the third part of this dissertation, rhodium(0) nanoparticles were stabilized on the structure of nanoalumina and their catalytic activities were examined in hydrogen generation from the methanolysis of AB. Alumina is a well-studied structural material with different transition phases which have been used in many industrial and technological applications. It has been mostly preferred as a catalyst or catalyst support used in heterogeneous catalysis due to its valuable properties. The particle size of our third supporting material is in nano regime with an average particle diameter of 13 nm. The following textural properties of nanoalumina are the reasons why it has been preferred as supporting materials in catalytic applications;

- i)* high specific surface area
- ii)* pore volume
- iii)* pore-size distribution
- iv)* acid/base characteristics of surface
- v)* chemical and hydrothermal stability
- vi)* interaction with supported transition metals
- vii)* low cost

5.3.1. Preparation and Characterization of Rhodium(0) Nanoparticles Supported on Nanoalumina

The preparation of Rh(II) ions impregnated on nanoalumina (Rh(II)/nanoAl₂O₃) and *in situ* formation of rhodium(0) nanoparticles supported on nanoalumina (Rh(0)/nanoAl₂O₃) during the catalytic methanolysis of AB occurred in the same medium. Briefly, a certain aliquot from stock solution of rhodium(II) octanoate was added to the suspension of nanoalumina in methanol and stirred for 1 h. Thus, the suspension of Rh(II) ions impregnated on nanoalumina (Rh(II)/nanoAl₂O₃) in methanol with desired rhodium concentration was obtained. Then, AB solution was injected to the same reaction flask thus; the catalytic methanolysis of AB was started after a short induction period. During that period, the colour of solution was altered from pale blue to black, demonstrating the reduction of Rh(II) ions impregnated on the surface of nanoalumina to rhodium(0) nanoparticles and formation of Rh(0)/nanoAl₂O₃. Rh(0)/nanoAl₂O₃ were quite active catalyst in

hydrogen generation from the methanolysis of AB, liberating 3.0 equivalent H₂ gas per mole of AB. The active catalyst was isolated from reaction solution by centrifugation and characterized by a combination of advanced analytical techniques.

After the preparation of Rh(II)/nanoAl₂O₃, the precatalyst was isolated from reaction flask and ATR-IR spectroscopy was studied in order to check whether rhodium(II) ions are accompanied by the octanoate anion in the impregnation on the surface of nanoalumina. Figure 41 shows the ATR spectra of sole nanoalumina and Rh(II)/nanoAl₂O₃ with a rhodium loading of 1.0 % wt. The broad absorption band at 3500 cm⁻¹ and a weak band at 1638 cm⁻¹ for the stretching and bending modes of OH groups, additionally strong framework bands in the range 500-1000 cm⁻¹ (not shown in the spectra to simplify the view) are common peaks for two samples, resulting from the structure of nanoalumina [133]. Besides, one can observe that there are two additional absorption bands at 1570 and 1420 cm⁻¹ in the ATR-IR spectrum of Rh(II)/nanoAl₂O₃ owing to the asymmetric and symmetric stretching of carboxylate group along with the C-H stretching bands at around 2900 cm⁻¹ indicating the presence of octanoate anion on the surface of nanoalumina [134]. Herein, the observed frequency differences of 150 cm⁻¹ between asymmetric and symmetric C-O vibrations indicates the existence of chelating or bridging carboxylate group [135].

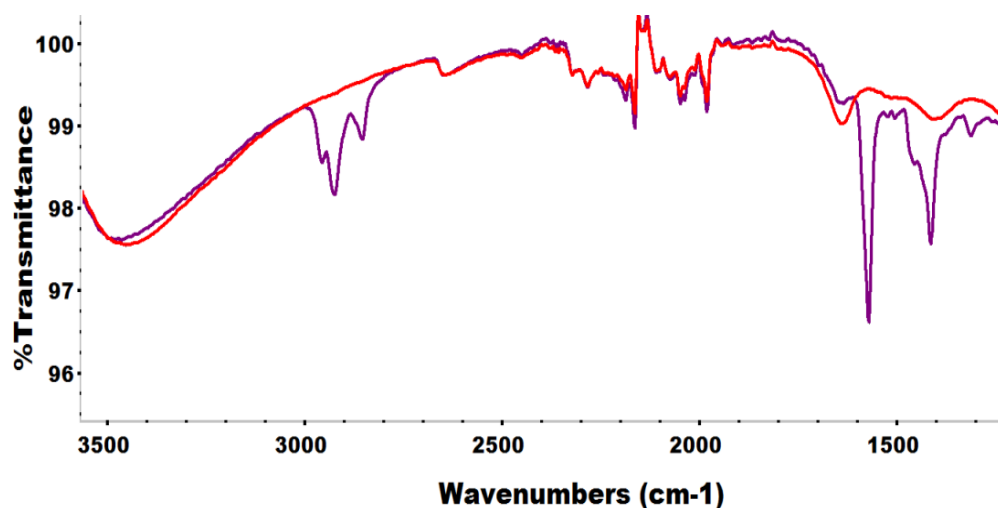


Figure 41. ATR-IR spectrum of (a) nanoalumina (b) Rh(II)/nanoAl₂O₃ with a rhodium loading of 1.0% wt. Rh.

Powder XRD spectroscopy was performed in order to examine whether there are any changes in the lattice or crystallinity of nanoalumina after preparation of Rh(0)/nanoAl₂O₃. XRD powder patterns for bare nanoalumina and Rh(0)/nanoAl₂O₃ are exhibited in Figure 42. The characteristic diffraction peaks of nanoalumina are observed in each of the powder XRD patterns, which indicate that alumina remains intact after the preparation of Rh(II)/nanoAl₂O₃ and the reduction of rhodium(II) to rhodium(0) during the methanalysis of AB. No additional diffraction peaks are observed which would be ascribable to rhodium(0) nanoparticles, most likely due to the low metal loading of nanoalumina.

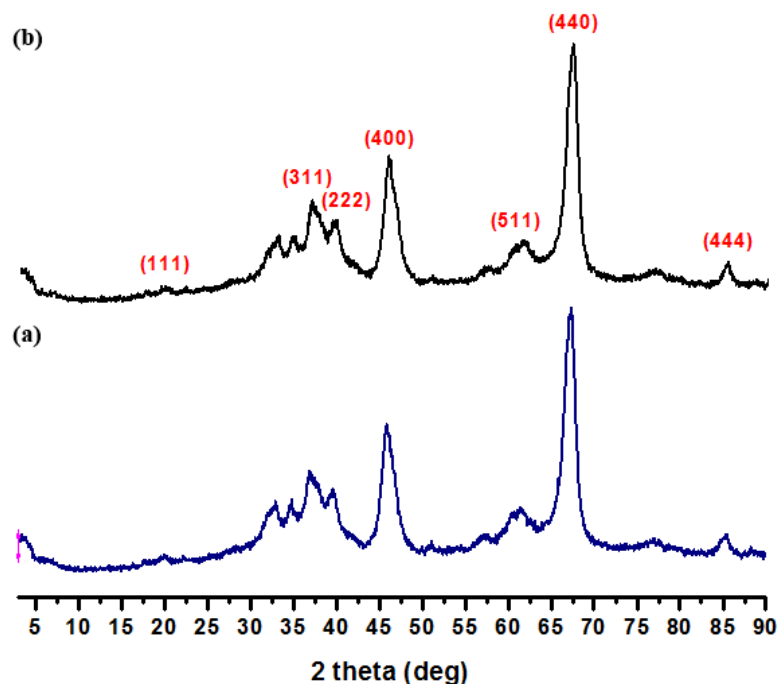


Figure 42. Powder X-ray diffraction (PXRD) patterns of a) nanoAl₂O₃, b) Rh(0)/nanoAl₂O₃ with rhodium loading of 0.50 % wt. Rh.

The TEM analysis of Rh(0)/nanoAl₂O₃ with different rhodium loadings (0.50, 1.0, 1.5 and 2.0 % wt. Rh) was performed to investigate the morphology and particle size of rhodium(0) nanoparticles for each percent loadings. The results of TEM reveal that rhodium(0) nanoparticles were homogeneously dispersed with a mean particle size of 3.6 - 4.1 nm on the surface of nanoalumina. Moreover, high resolution TEM images (HR-TEM) could be taken for Rh(0)/nanoAl₂O₃ with a rhodium loading of 1.0 %wt and the (111) lattice fringes of 0.222 nm could be measured for rhodium(0) nanoparticles [136]. Particle size histogram for each percent rhodium loadings could be constructed and depicted in Figure 43 as inset figures. TEM results also indicate the inverse relation between particle size and rhodium loading. Figure 43f shows the plot of particle size *versus* the percent rhodium loading of Rh(0)/nanoAl₂O₃ samples, indicating the increase in the particle size with the increasing metal loading of the nanomaterials.

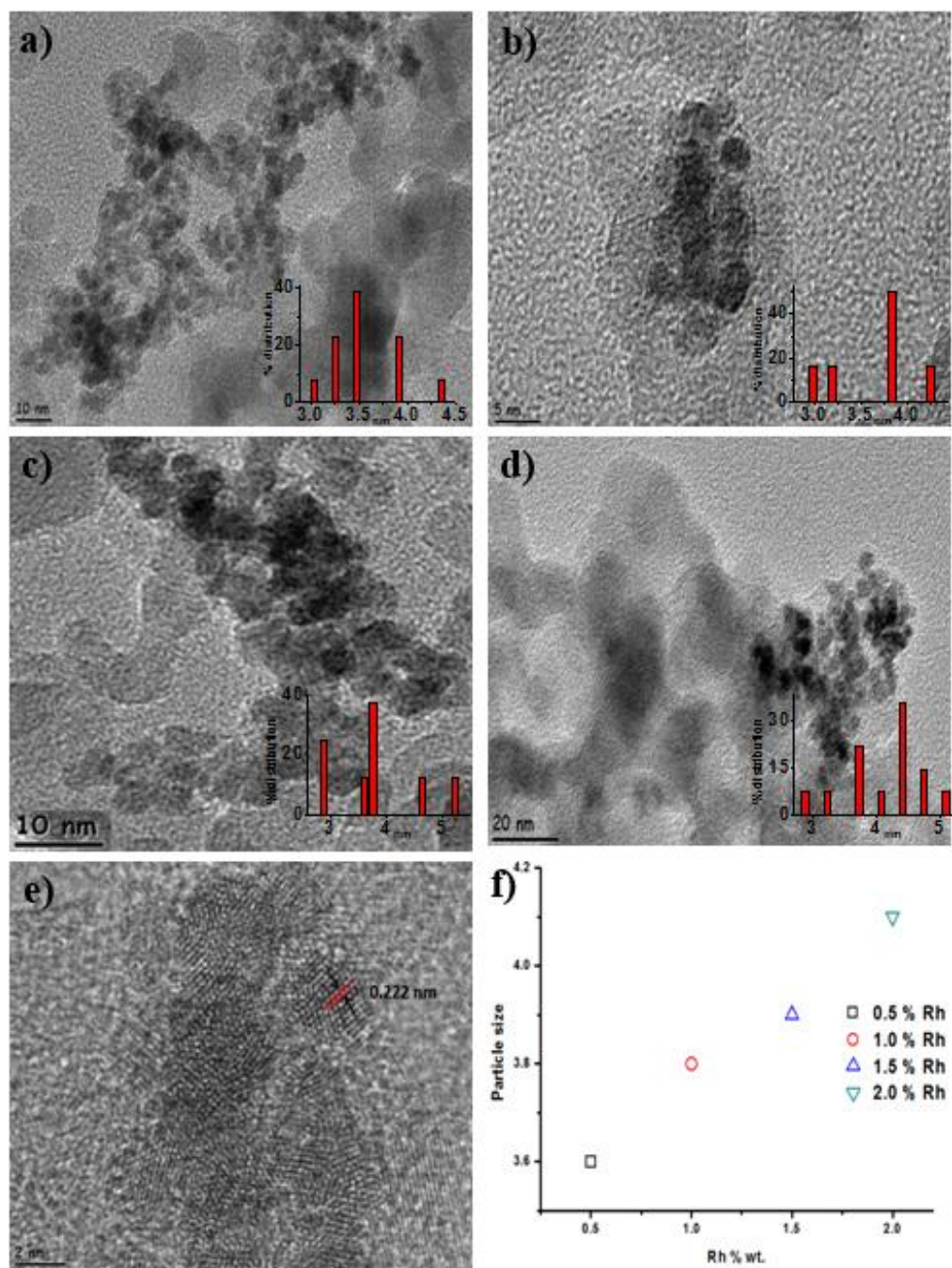


Figure 43. TEM images of Rh(0)/nanoAl₂O₃ with different rhodium loading a) 0.5, b) 1.0, c) 1.5, and d) 2.0 wt. % Rh after catalytic methanolysis reaction performed starting with 200 mM AB catalyzed by desired amount of Rh(0)/nanoAl₂O₃ at 25.0 ± 0.5 °C. e) HRTEM images of Rh(0)/nanoAl₂O₃ with rhodium loading of 1.0 wt. % f) the plot of percentage rhodium loading *versus* particle size.

The oxidation state and chemical environment of deposited rhodium nanoparticles can be analyzed by XPS. The survey scan XPS of Rh(0)/nanoAl₂O₃ with a rhodium loading of 2.0% wt. Rh in Figure 44a shows the presence of rhodium in addition to the framework elements of alumina (Al and O) in agreement with the SEM-EDX results (see later). The deconvolution of high resolution Rh 3d XPS spectrum of the same Rh(0)/nanoAl₂O₃ sample in Figure 44b depicts two prominent peaks at 307.2 and 312.2 eV, readily ascribed to the Rh(0) 3d_{5/2} and 3d_{3/2}, respectively, by comparing to the values of metallic rhodium [102]. Additionally, higher energy bands observed at 308.9, 314.9 eV and 310.3, 315.2 eV are attributable to the Rh⁺³ and Rh⁺⁴ 3d_{5/2} and 3d_{3/2}, respectively, likely in the form of oxide, which may originate from surface oxidation of rhodium(0) nanoparticles during the XPS sampling [137].

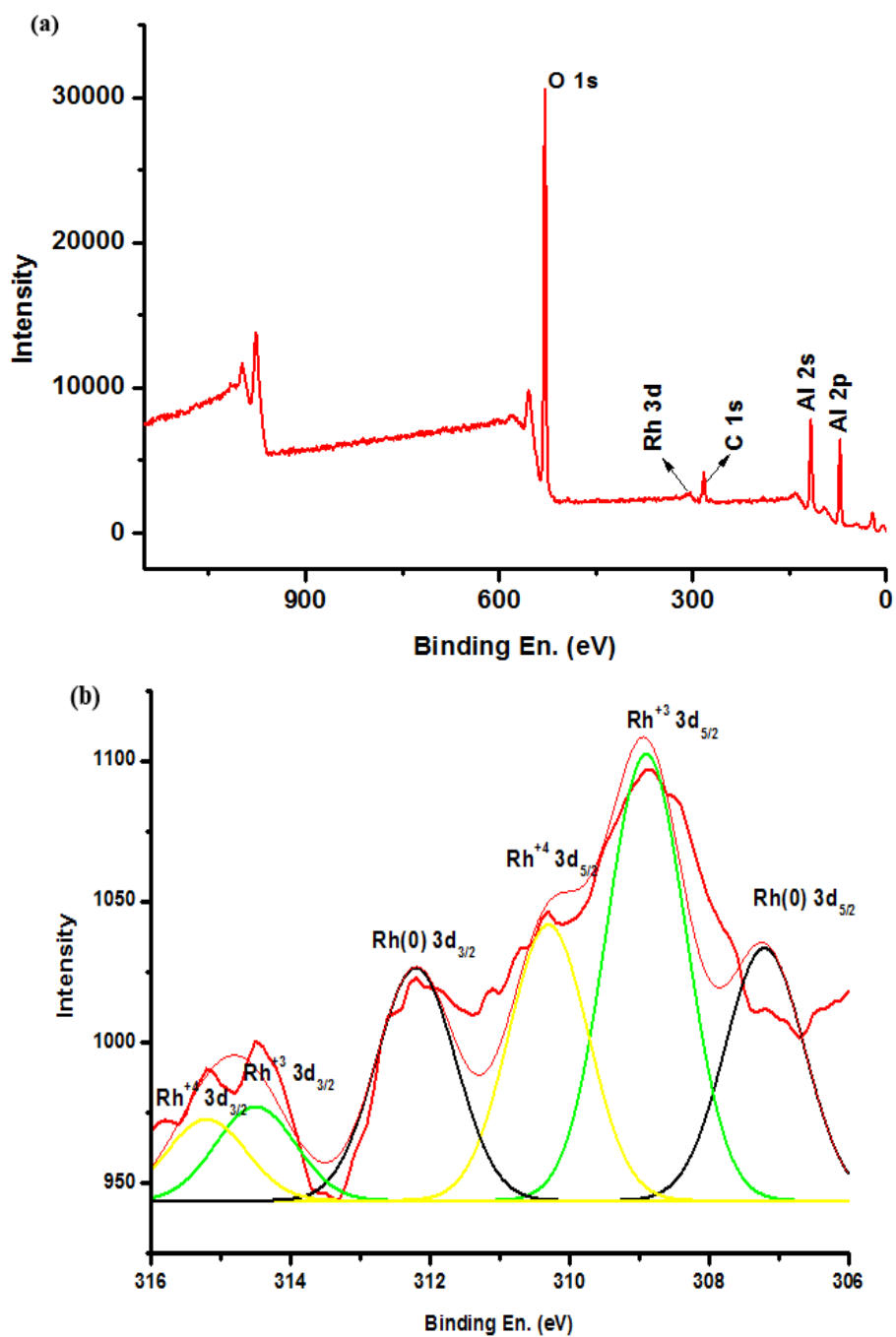


Figure 44. a) X-ray photoelectron (XPS) survey scan spectrum, b) high resolution Rh 3d XPS spectrum of Rh(0)/nanoAl₂O₃ with a rhodium loading of 2.0% wt. Rh.

Scanning electron microscopy (SEM) image of Rh(0)/nanoAl₂O₃ with a rhodium loading of 2.0 % wt. in Figure 45a shows that there is no bulk rhodium metal formation in detectable size on the surface of nanoalumina and SEM-EDX spectrum in Figure 45b confirms the presence of rhodium in addition to the framework elements of alumina (Al, O).

Surface area of nanoAl₂O₃ and Rh(0)/nanoAl₂O₃ with a loading of 1.5 % wt. Rh were determined by the N₂ adsorption measurement to be 91.6 and 96.1 m²·g⁻¹, respectively. The slight increase in the surface area of nanoalumina can be considered as an additional evidence for the formation of rhodium(0) nanoparticles on the surface of supporting materials.

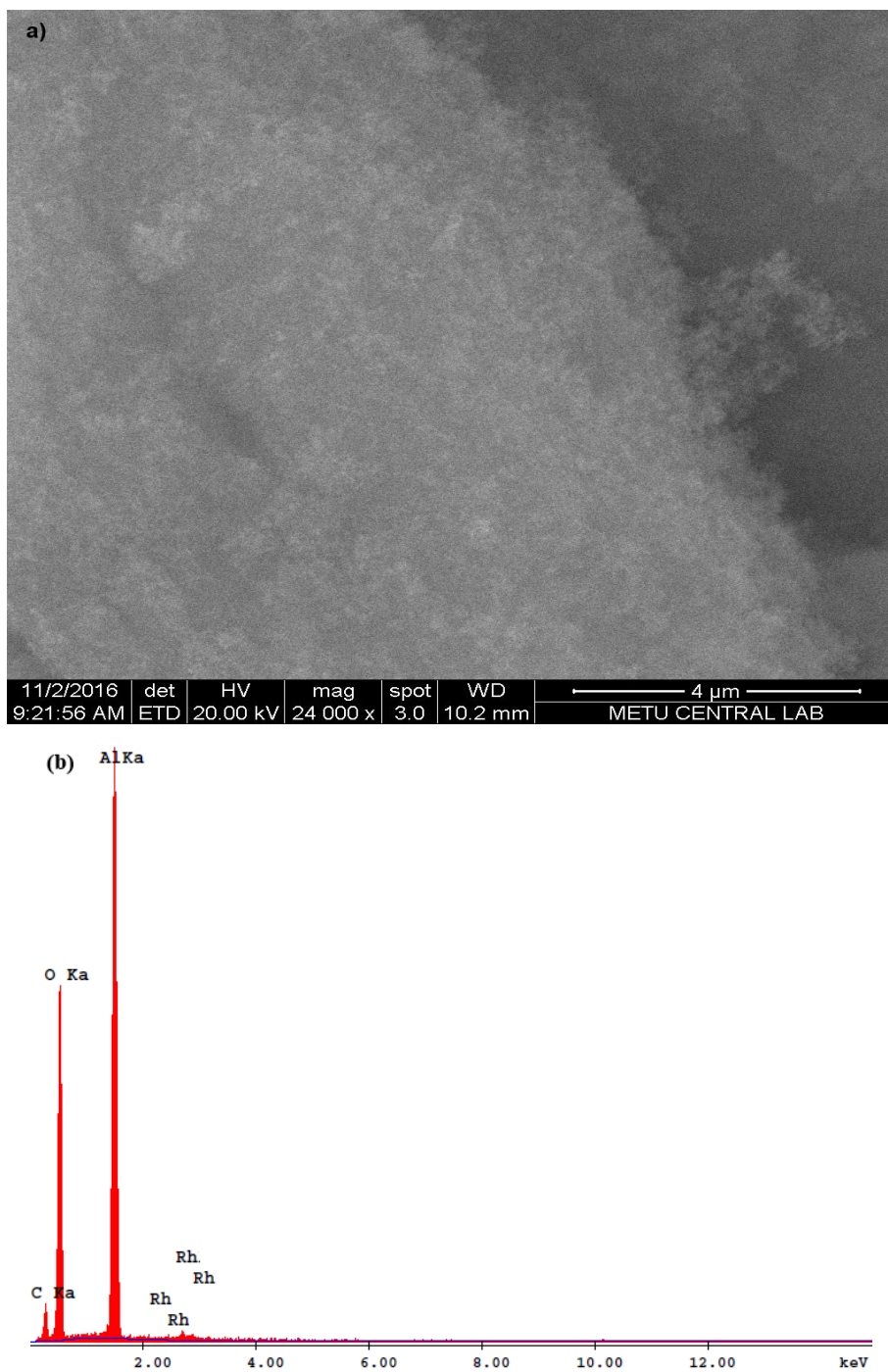


Figure 45. a) SEM image of Rh(0)/nanoAl₂O₃ b) SEM-EDX spectrum of Rh(0)/nanoAl₂O₃ with a rhodium loading of 2.0% wt. Rh.

5.3.2. The Catalytic Activities of Rhodium(0) Nanoparticles Supported on Nanoalumina in Hydrogen Generation from the Methanolysis of Ammonia Borane

5.3.2.1. Kinetic Studies and Determination of Activation Parameters for Methanolysis of Ammonia Borane Catalyzed by Rhodium(0) Nanoparticles Supported on Nanoalumina

The reduction of rhodium(II) octanoate, impregnated on the porous nanoalumina, Rh(II)/nanoAl₂O₃, provides the *in situ* formation of rhodium(0) nanoparticles supported on nanoalumina, Rh(0)/nanoAl₂O₃, during the methanolysis of AB. Rh(0)/nanoAl₂O₃ were found to be active catalyst in hydrogen generation from the methanolysis of AB. The volume of H₂ evolved during the reaction was monitored and converted into the equivalent H₂ per mole of AB using the known 3:1 H₂/AB stoichiometry (Eqn. 1). Evaluation of the kinetic data gives valuable insights to the formation of rhodium(0) nanoparticles and concomitant H₂ generation from the methanolysis of AB. Figure 46 displays the graph of mol H₂ per mole of AB *versus* time for the catalytic methanolysis of 200 mM AB in the presence of 50 mg of Rh(II)/nanoAl₂O₃ (0.50 wt.% Rh, [Rh] = 0.24 mM) in 10 mL methanol at 25.0 ± 0.5 °C. In such an experiment, the release of 3.0 equivalents H₂ per mole of AB could be achieved with almost linear hydrogen generation curve after a short induction period less than 1 min. The reaction medium changes its colour from the initial pale blue to black during the induction period. In addition to the alteration in colour, the sigmoidal shape of the hydrogen generation *versus* time plot in Figure 46 indicates the reduction of rhodium(II) to rhodium(0) and formation of rhodium(0) nanoparticles with Finke-Watzky 2-step mechanism consisting of slow, continuous nucleation (P → Q, rate constant k_1) and autocatalytic surface growth (P + Q → 2Q, rate constant k_2) as shown in Scheme 1 (on page 63), where P stands for the added precursor Rh(II)/nanoAl₂O₃ and Q for the growing rhodium(0) nanoparticles. The kinetic data in Figure 46 fit well to Eqn. 4 (on page 65) derived from the F-W 2-step mechanism [120] providing the rate constants $k_1 = 6.6 \times 10^{-2} \text{ min}^{-1}$ and $k_2 = 7.8 \times 10^1 \text{ M}^{-1} \text{ min}^{-1}$. These rate constants are for the slow, continuous nucleation and autocatalytic surface growth of Rh(0) nanoparticles, respectively, starting with 200 mM AB and 50 mg of Rh(II)/nanoAl₂O₃ (0.50 wt.% Rh, [Rh] = 0.24 mM) in 10 mL

methanol at 25.0 ± 0.5 °C. The large value of k_2/k_1 ratio (1.2×10^3) implies on the high level of kinetic control of the nanoparticles formation [120].

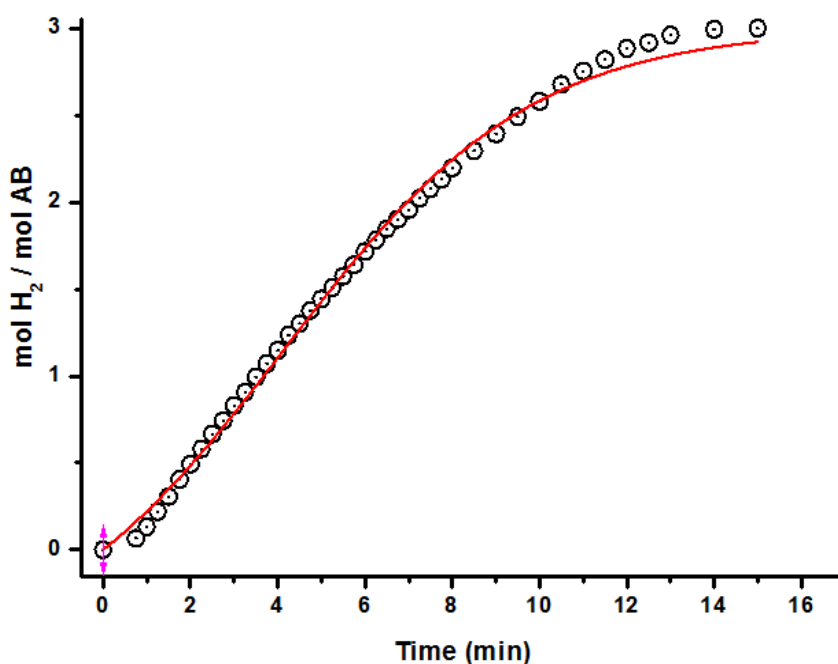


Figure 46. Plots of mol H₂ evolved per mole of AB *versus* time for the catalytic methanolysis of AB starting with 200 mM AB and 50 mg of Rh(II)/nanoAl₂O₃ (0.50 wt.% Rh, [Rh]= 0.24 mM) in 10 mL methanol at 25.0 ± 0.5 °C. The red curve shows the fit of data to the F-W 2-step mechanism of nanoparticle formation.

As control, two experiments were also performed under the same conditions starting with rhodium(II) octanoate either alone or impregnated on nanoalumina to investigate the effect of support on both activity and stability of rhodium(0) nanoparticles formed. Figure 47 depicts the plots of mol of H₂ evolved per mole of AB *versus* time for the catalytic methanolysis of 200 mM AB plus either 50 mg Rh(II)/nanoAl₂O₃ (1.0% wt. Rh, [Rh] = 0.49 mM) or 1.9 mg rhodium(II) octanoate (0.49 mM Rh) in 10 mL methanol at 25.0 ± 0.5 °C. The results of these control experiments show that both catalysts have similar

initial catalytic activity, however Rh(0) nanoparticles in the absence of support lose catalytic activity in the course of methanolysis reaction. It is noteworthy that bulk rhodium metal precipitate formed in the absence of support at the end of methanolysis. Therefore, it can be concluded that nanoalumina is an efficient support to obtain rhodium(0) nanoparticles which are stable and catalytically active.

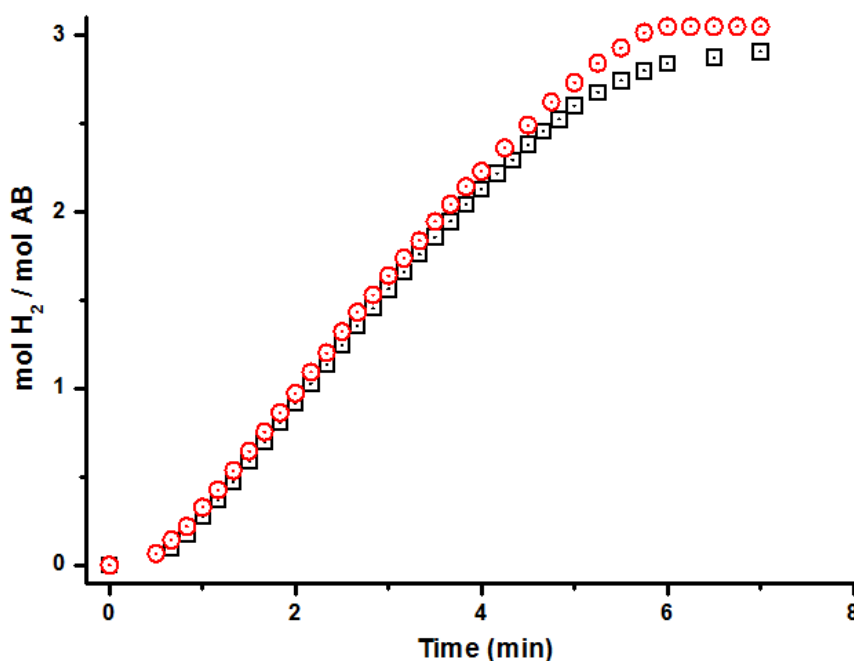


Figure 47. Plots of mol H₂ evolved per mole of AB *versus* time for the catalytic methanolysis of AB starting with 200 mM AB plus either (red circles, ○) 50 mg of Rh(II)/nanoAl₂O₃ (1.0 wt.% Rh, [Rh] = 0.49 mM) or (black squares, □) 1.9 mg of rhodium(II) octanoate (0.49 mM Rh) in 10 mL methanol at 25.0 ± 0.5°C.

An excellent catalytic performance of Rh(0)/nanoAl₂O₃ was observed in hydrogen generation from the methanolysis of AB providing 3.0 equivalents H₂ per mole of AB at room temperature. Figure 48a shows the plots of mol H₂ evolved per mole of AB *versus* time during the catalytic methanolysis

performed starting with 200 mM AB in various rhodium loading, thus in various rhodium concentrations at 25.0 ± 0.5 °C. In all cases after a short induction period less than 1.0 min, a hydrogen evolution starts and continues almost linearly until the complete consumption of AB present in the solution. It is noteworthy that the rate of hydrogen generation remains practically constant in linear portion of the plots. This implies on the structure insensitivity of catalytic methanolysis of AB. All the kinetic data in Figure 48a fit well to the Finke Watzky 2-step mechanism of nanoparticle formation [120,121] yielding the rate constants k_1 of the slow, continuous nucleation and k_2 of the autocatalytic surface growth for the formation of rhodium(0) nanoparticles from rhodium(II) during the methanolysis (Table 3) [120]. The large values of k_2/k_1 ratio in Table 3 indicate that the formation of rhodium(0) nanoparticles from the reduction of rhodium(II) precursor during the methanolysis of AB is kinetically controlled.

Turnover frequency (TOF) values were calculated from the hydrogen generation rate in the linear part of each plot given in Figure 48a for the methanolysis of 200 mM AB at 25.0 ± 0.5 °C and listed in Table 3 along with the corrected TOF values by considering the number of rhodium sites on the surface of nanoparticle. Eqn. 5, 6, and 7 were used in calculations of number rhodium atoms in nanoparticle, number of rhodium atoms on the surface of nanoparticle and corrected TOF values, respectively. Rh(0)/nanoAl₂O₃ sample with rhodium concentration of 0.24 mM Rh provides the highest catalytic activity with an initial TOF = 218 min⁻¹ (692 min⁻¹ corrected for surface rhodium atoms, Table 3) ever reported for hydrogen generation from the methanolysis of AB at 25.0 ± 0.5 °C [123]. Comparison of the values in Table 3 shows that the TOF decreases as the rhodium loading in the Rh(0)/nanoAl₂O₃ catalyst increases. The inverse relation between the TOF and the catalyst concentration (Figure 48b) can be correlated to the increasing size of rhodium(0) nanoparticles (Figure 43f). The catalytic activity of Rh(0)/nanoAl₂O₃ in hydrogen generation from the methanolysis of AB decreases as the particle size of the rhodium(0) nanoparticles increases with the increasing rhodium loading. However, when TOF values are corrected for the number of rhodium atoms on the surface of nanoparticles (Table 3) the inverse dependence of catalytic activity on the size of nanoparticles becomes

less pronounced. The disappearance of inverse dependence for the corrected TOF values is also indicative of that the inverse relation between the catalytic activity and rhodium concentration is indeed a size issue.

The hydrogen generation rate was determined from the linear portion of graph for each rhodium concentration in Figure 48a and plotted *versus* the initial rhodium concentration as an inset graph in Figure 48a, both axes being in logarithmic scale. This plot gives a straight line with a slope of $0.90 \approx 1.0$ indicating that the methanolysis of AB catalyzed by Rh(0)/nanoAl₂O₃ is first order with respect to catalyst. It is noteworthy that hydrogen generation starts immediately after a short induction time less than 1.0 min and proceeds almost linearly in course of methanolysis reaction; therefore it is conceivable that methanolysis of AB is zero order with respect to substrate.

Table 3. The rate constants k_1 of the slow, continuous nucleation, $P \rightarrow Q$, and k_2 of the autocatalytic surface growth, $P + Q \rightarrow 2Q$, for the formation of rhodium(0) nanoparticles catalyst from the reduction of rhodium(II) ions during the methanolysis of AB (200 mM) starting with Rh(II)/nanoAl₂O₃ with different rhodium loading, rhodium concentrations, hydrogen generation rates, turnover frequency (TOF) values, and the TOF values corrected for the number of rhodium atoms on the surface of nanoparticles for the methanolysis of AB at 25.0 ± 0.5 °C.

wt. %Rh	Particle size (nm)	Number of Rh atoms in NP	Number of Rh atoms on surface	[Rh] (mM)	k_1 (min ⁻¹)	k_2 (M ⁻¹ min ⁻¹)	k_2/k_1	H ₂ generation rate (mmol/min)	TOF (min ⁻¹)	TOF _{corrected} (min ⁻¹)
0.5	3.6 ± 0.4	1773	558	0.244	$(6.64 \pm 0.25) \times 10^{-2}$	78.1 ± 3.1	1.18×10^3	0.54	218	692
1.0	3.8 ± 0.7	2085	622	0.491	$(7.46 \pm 0.57) \times 10^{-2}$	117.5 ± 5.4	1.57×10^3	1.17	188	630
1.5	3.9 ± 0.7	2254	655	0.761	$(8.54 \pm 0.64) \times 10^{-2}$	104.1 ± 4.2	1.22×10^3	2.38	158	544
2.0	4.1 ± 0.6	2619	724	0.991	$(8.21 \pm 0.96) \times 10^{-2}$	118.9 ± 6.2	1.48×10^3	3.37	154	557

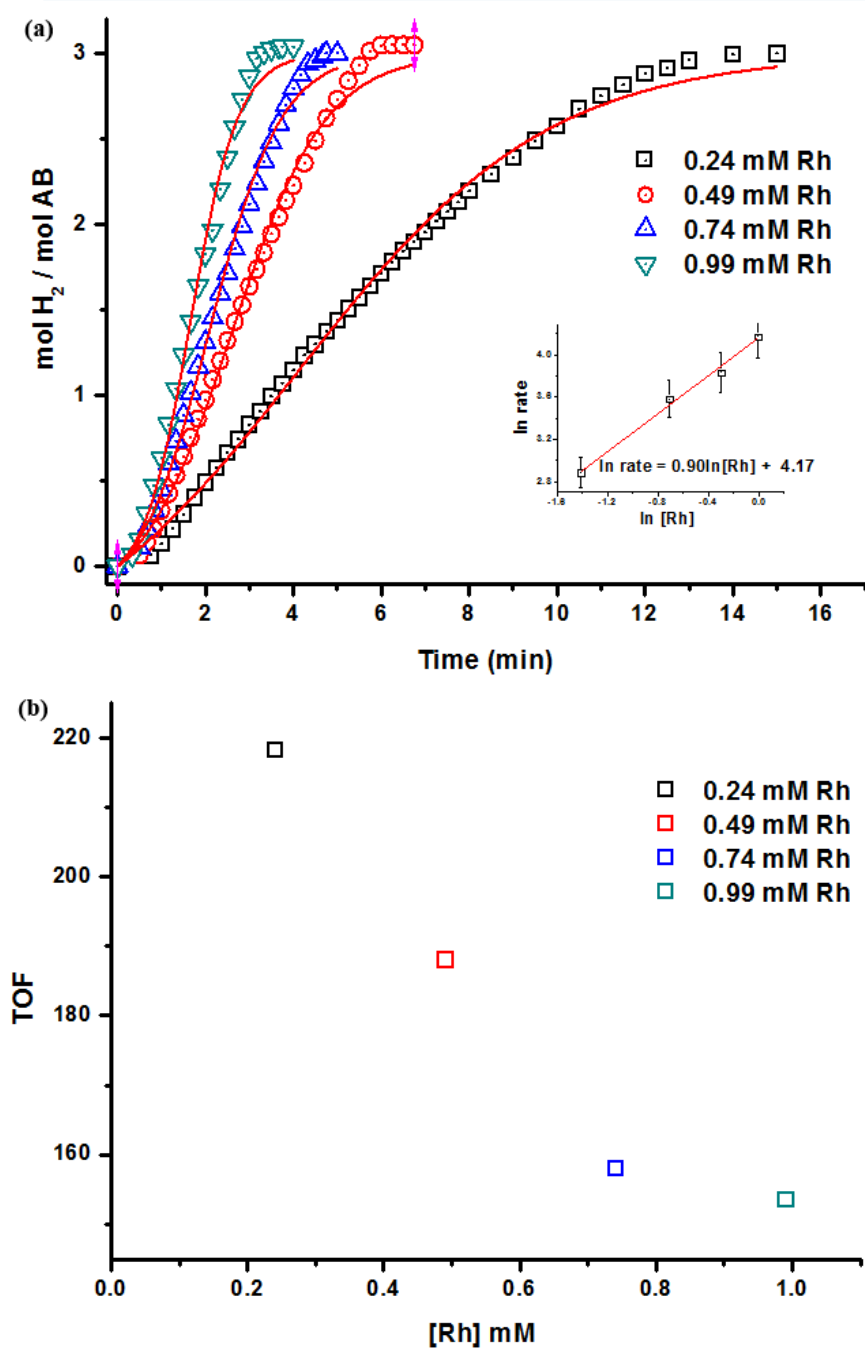


Figure 48. a) Plots of mol H_2 evolved per mole of AB *versus* time for methanolysis of 200 mM AB in different metal concentrations ($[\text{Rh}] = 0.24, 0.49, 0.74$ and 0.99 mM, each prepared using metal loading of 0.50, 1.0, 1.5, 2.0% wt. Rh, respectively) at 25.0 ± 0.5 °C. Inset: Plot of hydrogen generation rate *versus* the concentration of rhodium (both in logarithmic scale.). b) Inverse dependence of initial TOF value on the initial precatalyst Rh concentration.

Figure 49a gives the plots of mol H₂ evolved per mole of AB *versus* time for the methanolysis of AB starting with 0.24 mM Rh catalyst (0.50 wt.% Rh, 50 mg Rh(II)/nanoAl₂O₃) plus 200 mM AB substrate at various temperatures in the range of 20-35 °C. The rate constants k_1 of the slow, continuous nucleation and k_2 of the autocatalytic surface growth for the formation of rhodium(0) nanoparticles catalyst during the methanolysis of AB can be calculated by curve-fitting the experimental data to the Finke-Watzky 2-step mechanism [120]. Table 4 gives the list of the rate constants k_1 and k_2 as well the k_2/k_1 ratio. A high level kinetic control in the formation of rhodium(0) nanoparticles from the reduction of rhodium(II) precursor in the presence of nanoalumina can readily be seen from the large value of k_2/k_1 ratio at any temperature in the range 20-35 °C [120]. Since we have the rate constants k_1 and k_2 for the individual steps of the rhodium(0) nanoparticles formation at various temperatures we are now able to calculate the activation parameters for the slow, continuous nucleation and autocatalytic surface growth of the rhodium(0) nanoparticles on the surface of nanoalumina, as well as for the catalytic methanolysis of AB catalyzed by Rh(0)/nanoAl₂O₃ from the temperature dependent kinetic data. Activation energy for the nucleation and autocatalytic surface growth were determined from the Arrhenius plots by using the values of rate constants k_1 and k_2 at different temperatures in Figure 49b and 49c, respectively: $E_a = 67 \pm 2$ kJ/mol for the nucleation and $E_a = 48 \pm 2$ kJ/mol for the autocatalytic surface growth.

Activation parameters for methanolysis of AB catalyzed by Rh(0)/nanoAl₂O₃ could also be determined from the temperature dependent kinetic data in Figure 49a. The slope of each plot in the linear part could be used to calculate the rate constant k_{obs} and the TOF values at various temperatures (Table 4). It is noteworthy that also TOF value increases with increasing temperature reaching a remarkable value of 557 min⁻¹ (1770 min⁻¹ corrected for the number of rhodium atoms on the surface of nanoparticle) in hydrogen generation from the catalytic methanolysis of AB at 35 °C. In addition, the values of reaction rate constant k_{obs} were used for drawing of Arrhenius plot and Eyring plot given in Figure 49d and e, respectively; the activation energy $E_a^{app} = 62 \pm 2$ kJ/mol, the activation enthalpy $\Delta H^{\ddagger,app} = 61 \pm 2$ kJ/mol, and the activation entropy $\Delta S^{\ddagger,app} = -16 \pm 4$ J/mol.K.

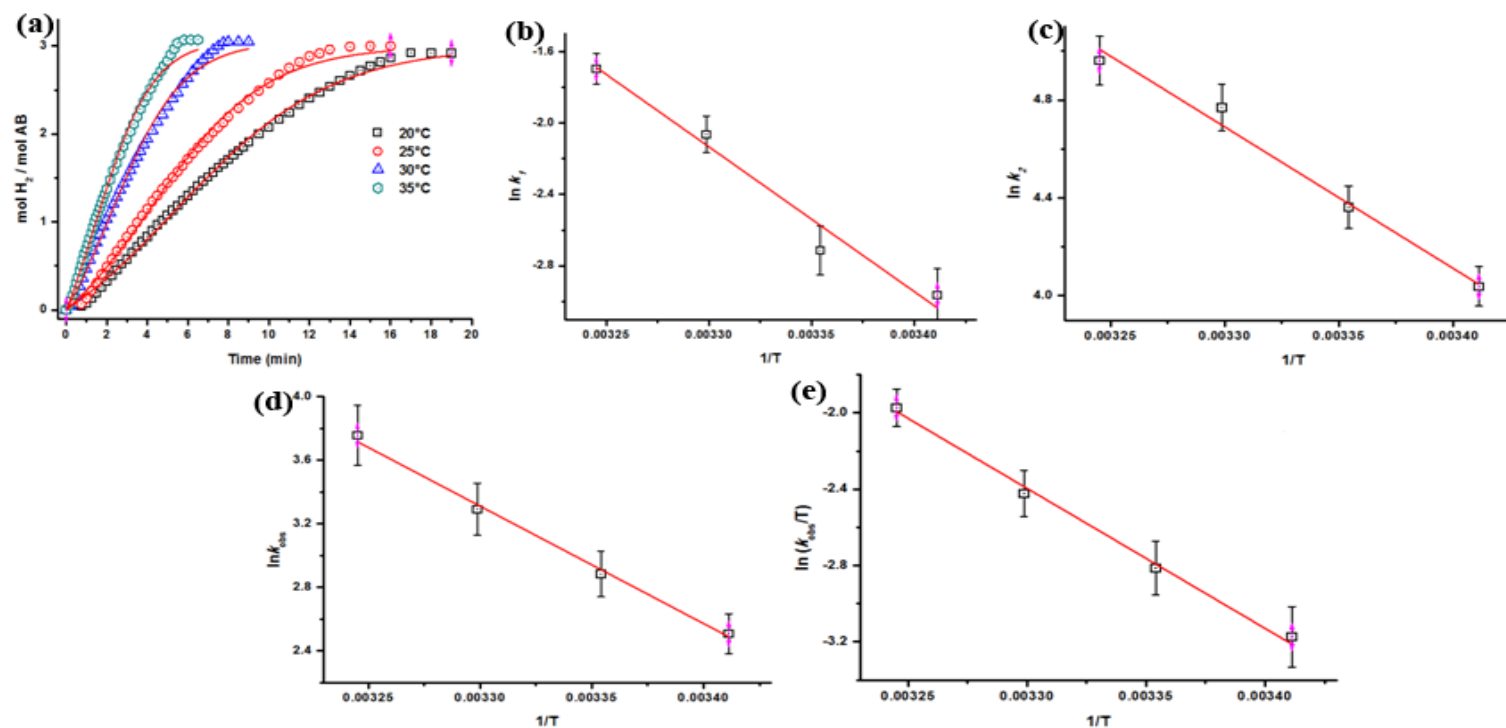


Figure 49. (a) Plots of mol H₂ evolved per mole of AB *versus* time for the catalytic methanolysis of AB at various temperatures in the range of 20 – 35 °C keeping the concentration of substrate at [AB] = 200 mM and rhodium at [Rh] = 0.24 mM (0.50 wt. % Rh, 50 mg Rh(0)/nanoAl₂O₃), (b) The Arrhenius plot for nucleation of rhodium(0) nanoparticles, (c) The Arrhenius plot for the autocatalytic surface growth of rhodium(0) nanoparticles, (d) The Arrhenius plot (e) The Eyring plot.

Table 4. The rate constants k_1 of the slow, continuous nucleation, $P \rightarrow Q$, and k_2 of the autocatalytic surface growth, $P + Q \rightarrow 2Q$, for the formation of rhodium(0) nanoparticles catalyst from the reduction of rhodium(II) ions during the methanolysis of AB, hydrogen generation rates, k_{obs} values, turnover frequency (TOF) values, and the TOF values corrected for the number of rhodium atoms on the surface of nanoparticles for the methanolysis of AB starting with $[AB] = 200$ mM and $[Rh] = 0.24$ mM at different temperatures.

Temperature (°C)	k_1 (min^{-1})	k_2 ($\text{M}^{-1} \text{min}^{-1}$)	k_2/k_1	H ₂ generation rate ($\text{mmol H}_2 \text{ min}^{-1}$)	k_{obs} ($\text{mol H}_2 \text{ molRh}^{-1} \text{ s}^{-1}$)	TOF (min^{-1})
20	$5.16 \times 10^{-2} \pm 1.36 \times 10^{-3}$	$56.7 \pm .17$	1.10×10^3	0.42	2.86	172
25	$6.63 \times 10^{-2} \pm 2.51 \times 10^{-3}$	78.4 ± 3.2	1.18×10^3	0.54	3.67	218
30	$1.27 \times 10^{-1} \pm 5.65 \times 10^{-3}$	117.9 ± 6.3	0.93×10^3	1.04	7.08	425
35	$1.83 \times 10^{-1} \pm 7.11 \times 10^{-3}$	142.7 ± 7.7	0.78×10^3	1.32	9.04	557

5.3.2.2. Catalytic Lifetime of Rhodium(0) Nanoparticles Supported on Nanoalumina in Hydrogen Generation From the Methanolysis of Ammonia Borane

A catalytic lifetime experiment was performed starting with 10 mL suspension containing 0.24 mM Rh (50.0 mg Rh(0)/nanoAl₂O₃, 0.5 wt.% Rh,) and 400 mM AB at 25.0 ± 0.5 °C (Figure 50). The reaction was sustained by adding a new batch of AB into reaction flask when the AB present in the solution was consumed in releasing H₂ gas. This procedure was continued until no more gas evolution was observed. The catalytic lifetime experiment reveals a minimum of 16,300 turnovers in hydrogen generation from the methanolysis of AB at 25.0 ± 0.5 °C before deactivation and provides the highest exceptional initial turnover frequency (TOF) value of 218 min⁻¹ in hydrogen generation from the methanolysis of AB at 25.0 ± 0.5 °C. The rate of hydrogen generation decreases as the reaction proceeds and finally reaches the zero, may be, due to the increasing viscosity of reaction solution or deactivation effect of tetramethoxyborate concentration. It should be noted that these TTO values can be considered as a lower limit unless the increase in the viscosity and the deactivation of catalyst surface are avoided by removal of tetramethoxyborate product from the reaction medium. Thus much higher TTO values for hydrogen generation from methanolysis of AB catalyzed by Rh(0)/ nanoAl₂O₃ might be expected.

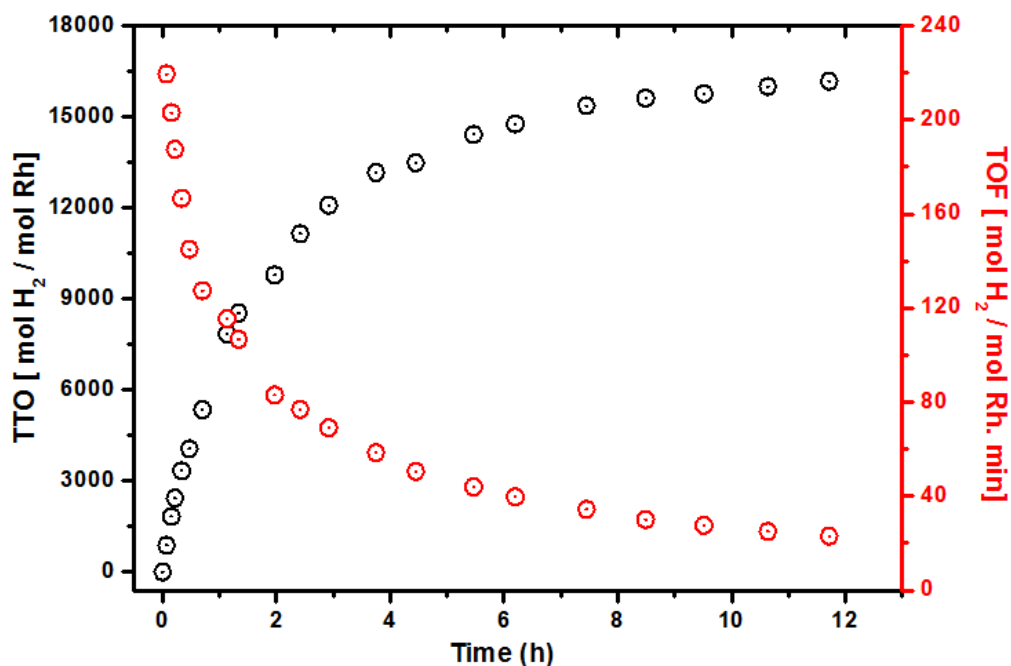


Figure 50. Plot of total turnover number (TTO) or turnover frequency *versus* time for the methanolysis of AB with 10 mL solution of 0.24 mM Rh (50.0 mg Rh(0)/nanoAl₂O₃, 0.50 wt.% Rh,) and 400 mM AB (for each run) at 25.0 ± 0.5 °C.

5.3.2.3. Leaching Test for Rhodium(0) Nanoparticles Supported on Nanoalumina in the Methanolysis of Ammonia Borane

When the rhodium(0) nanoparticles are not strongly anchored on the surface of support, rhodium can leach into the solution during the catalytic methanolysis of AB. This can be checked by performing the widely used leaching test for the catalytic methanolysis of AB. Such a control experiment was performed starting with 200 mM AB plus 50 mg Rh(II)/nanoAl₂O₃ (0.50 % wt. Rh, [Rh] = 0.24 mM) in 10 mL methanol at 25.0 ± 0.5 °C. After the liberation of 3.0 equivalents H₂ gas per mole of AB, the reaction was filtered to separate the solid Rh(0)/nanoAl₂O₃ phase from the solution under the inert nitrogen atmosphere. The filtrate solution was transferred into another reaction flask. A new batch of 200 mM AB was added to the solution and hydrogen generation was followed at 25.0 ± 0.5 °C. The filtrate solution was found to be

catalytically silent in the methanolysis of AB (Figure 51). The results of the leaching test provides a compelling evidence for the retaining of rhodium(0) nanoparticles within the nanoalumina matrix. In addition, the filtrate solution was also analyzed by ICP and no rhodium was detected in the solution. It is worth to mention that exact measurement of the catalytic activity of isolated solid materials in subsequent runs of methanolysis is not doable because of the noticeable materials loss during the isolation and redispersion processes. Therefore, a reliable reusability test could not be performed.

5.3.2.4. Carbon Disulfide (CS₂) Poisoning Heterogeneity Test for Rhodium(0) Nanoparticles Supported on Nanoalumina in the Methanolysis of Ammonia Borane

A CS₂ poisoning experiment was performed to check whether the catalytic methanolysis of AB is heterogeneous or homogeneous. When the active metal center is blocked by poison molecule, it won't be accessible by the substrate molecules and catalytic activity will be ceased [113,114]. After the formation of catalytically active rhodium(0) nanoparticles and liberation of 40% hydrogen from methanolysis of AB, 0.20 equivalent CS₂ per mole of rhodium was rapidly injected to reaction mixture containing 200 mM AB catalyzed by 0.24 mM Rh (0.50 wt.% Rh). The hydrogen evolution was stopped immediately (Figure 51). This observation indicates that the Rh(0)/nanoAl₂O₃ catalyst was poisoned by addition of 0.20 equivalent CS₂ per mole of rhodium. Taking the results of both poisoning and leaching tests together one can conclude that Rh(0)/nanoAl₂O₃ are kinetically competent catalysts and heterogeneous catalysis in the methanolysis of AB.

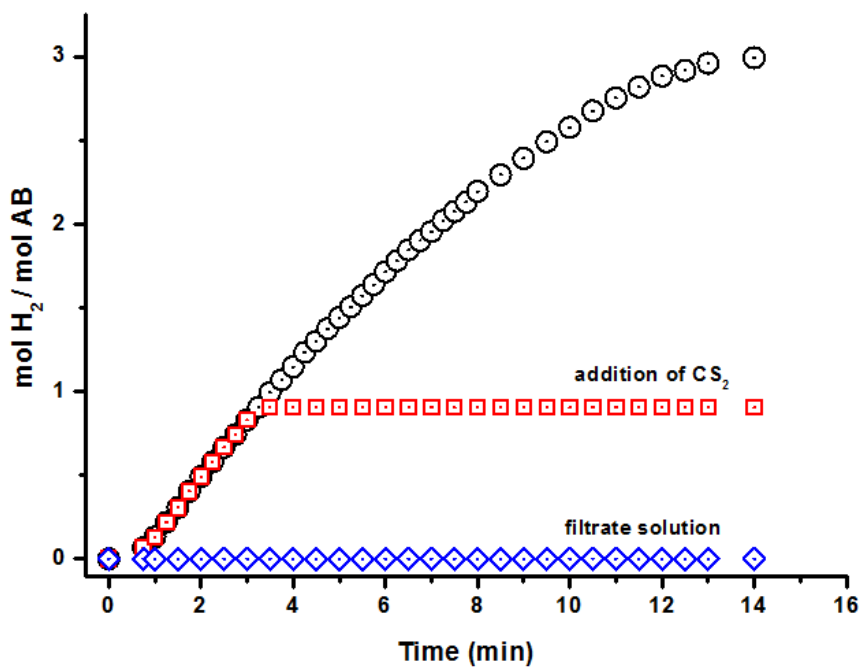


Figure 51. Plots of mol H₂ evolved per mole of AB *versus* time for the methanolysis of 200 mM AB catalyzed by Rh(0)/nanoAl₂O₃ (0.24 mM Rh, 0.50 wt. % Rh(0)/nanoAl₂O₃) with (square, □) and without (circle, ○) addition of 0.2 equiv. CS₂, and (triangle, Δ) the filtrate solution obtained from filtration of active catalyst after methanolysis of AB at 25.0 ± 0.5 °C.

5.4. Preparation and Characterization of Rhodium(0) Nanoparticles Supported on Nanoceria and Investigation of Their Catalytic Activities in Hydrogen Generation From the Methanolysis of Ammonia Borane

The last nanooxide crystalline supporting material investigated in this dissertation is nanoceria with an average particle diameter of 25 nm. There are many studies in the literature showing that the metals stabilized on ceria exhibit superior catalytic activities in various reactions [138]. As a reducible oxide, ceria contains cerium(III) defects which can easily be formed on the surface of cerium oxides due to the high positive standard potential of $\text{Ce}^{4+} \rightarrow \text{Ce}^{3+}$ (1.76 V in acidic solution) [139]. The presence of cerium(III) defects causes an excess negative charge accumulation on the oxide surface. The charge-balance on the oxide surface can be established by the coordination of metal(0) nanoparticles to oxide surface, which provides strong metal-support interaction, in particular, of the electron rich late transition metal nanoparticles [140,141,142]. Even today, many research groups have been still investigating the mechanism of the promoting effect of cerium oxides, however it has not been well explained yet. Notwithstanding, ceria supported metal nanoparticles have been studied extensively in the field of catalysis such as oxidation of organic compounds [143] and CO [144,145], hydrogenation of aromatics [146] and decomposition of N_2O and acetic acid [147,148], hydrogen generation from hydrolysis of AB [92,149,150,151], dehydrogenation of formic acid [152], ethanol steam reforming [153]. The formation of small clusters (such as Pt, Rh or Pd) on the surface of ceria has been widely elucidated in the literature. Nehasil and co-workers demonstrated, using a set of spectroscopic methods and DFT calculations, that there is a fast charge transfer from rhodium to ceria [154]. This charge transfer induces the formation of $\text{Rh}^{+\delta}$ and Ce^{3+} states that may enhance the catalytic activity [155]. In order to examine catalytic promoting effect of ceria, rhodium(0) nanoparticles supported on nanoceria were synthesized and their catalytic activities were investigated in the methanolysis of AB.

5.4.1. Preparation and Characterization of Rhodium(0) Nanoparticles Supported on Nanoceria

The same method mentioned in the preparation of Rh(0)/nanoAl₂O₃ in part 5.3.1 was applied to prepare Rh(0)/nanoCeO₂ catalyst. Both impregnation of Rh(II) ions on nanoceria (Rh(II)/nanoCeO₂) and *in situ* reduction of Rh(II) ions to

rhodium(0) nanoparticles on the surface of nanoceria to form rhodium(0) nanoparticles supported on nanoceria (Rh(0)/nanoCeO₂) during catalytic methanolysis of AB took place in the same flask without any additional preparation step. Shortly, a required amount of stock solution of rhodium(II) octanoate dimer was transferred into the suspension of nanoceria in methanol. After a stirring period of 1h, the suspension of rhodium(II) ions impregnated on nanoceria (Rh(II)/nanoCeO₂) with target rhodium concentration was prepared. Later on, AB solution was injected to the same reaction flask to start hydrogen generation from the catalytic methanolysis of AB. After a short induction time, the colour of reaction solution was changed from pale blue to black referring the reduction of Rh(II) ions to rhodium(0) nanoparticles and formation of Rh(0)/nanoCeO₂ in methanol and then, hydrogen generation from methanolysis of AB started rapidly. Rh(0)/nanoCeO₂ was highly active catalyst in hydrogen evolution from the methanolysis of AB. After the settling the powders, supernatant solution was taken out using a capillary syringe. The remaining powder was dried in vacuum at room temperature and characterized by a set of advanced analytical techniques.

Powder XRD was the first characterization technique to analyse changes in the framework lattice or crystallinity of nanoceria after the synthesis of Rh(0)/nanoCeO₂. Figure 52 depicts the XRD patterns of bare nanoceria and Rh(0)/nanoCeO₂. Both samples give the same XRD patterns showing the characteristic diffraction peaks of ceria at 28.5, 33.1, 47.5, 56.3 and 59.1 attributed to the (111), (200), (220), (311) and (222) reflections of ceria, respectively. Thus, it can be concluded that ceria preserves both crystallinity and the lattice after the impregnation of Rh(II) ions and their reduction to Rh(0) on nanoceria. It is noteworthy that no diffraction peaks are observable for rhodium(0) nanoparticles due to the low Rh concentration of Rh(0)/nanoCeO₂ sample.

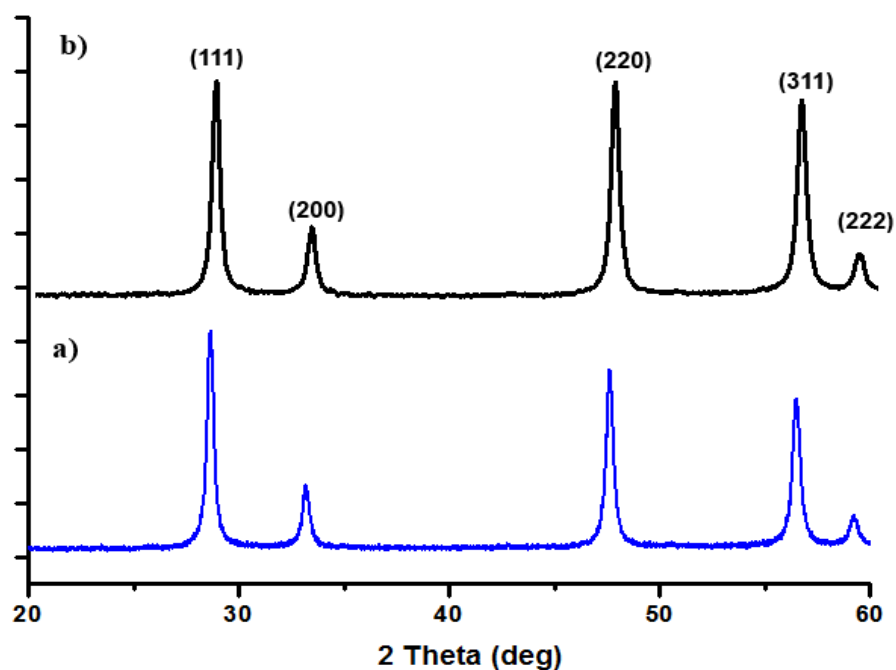


Figure 52. Powder X-Ray diffraction patterns of a) nanoCeO₂ b) Rh(0)/nanoCeO₂ with rhodium loading of 1.0 % wt. Rh.

TEM analysis of Rh(0)/nanoCeO₂ samples was also done to gather information about the morphology and particle size of rhodium(0) nanoparticles on the surface of nanoceria. Figure 53 shows TEM images and STEM-EDS mapping of Rh(0)/nanoCeO₂ sample with a rhodium loading of 1.0 % wt. Rh after the catalytic methanolysis of AB. STEM-EDS mapping (Figure 53d) reveals the uniform dispersion of rhodium(0) nanoparticles on the surface of nanoceria. The particle size of rhodium(0) nanoparticles can be determined from the TEM images in Figure 53a-b to be in the range 2.9 – 5.2 nm with an average size of 3.9 ± 0.6 nm as shown in the histogram (Figure 53c).

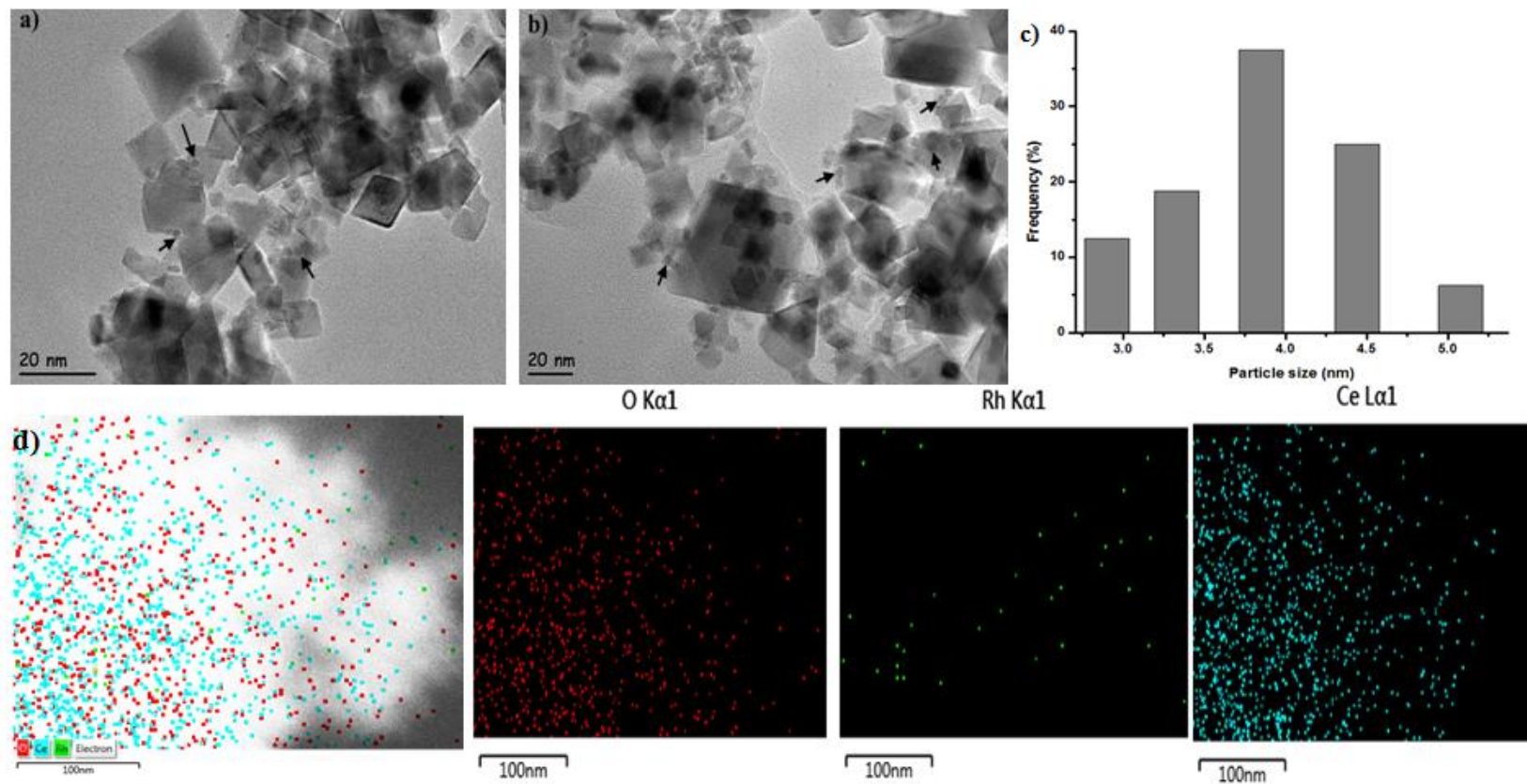


Figure 53. (a-b) TEM images of Rh(0)/nanoCeO₂ with a rhodium loading 1.0 wt. % Rh after catalytic methanolysis of 200 mM AB at 25.0 ± 0.5 °C. c) The corresponding histogram of rhodium(0) nanoparticle size distribution. d) STEM-EDS mapping of O, Rh and Ce.

Rh(0)/nanoCeO₂ sample was also examined by XPS to get information about chemical composition of sample and the oxidation state of rhodium and cerium. Figure 54a displays a survey scan XPS of Rh(0)/nanoCeO₂ sample with a rhodium loading of 1.0 %wt. Rh indicating the existence of rhodium in addition to the framework elements of ceria (Ce and O) in agreement with the SEM-EDX results (see later). The high resolution Rh 3d XPS scan of the same sample (Figure 54b) shows two prominent peaks at 306.4 and 311.5 eV, readily assigned to the Rh(0) 3d_{5/2} and 3d_{3/2}, respectively, by comparing to the values of metallic rhodium [102,156].

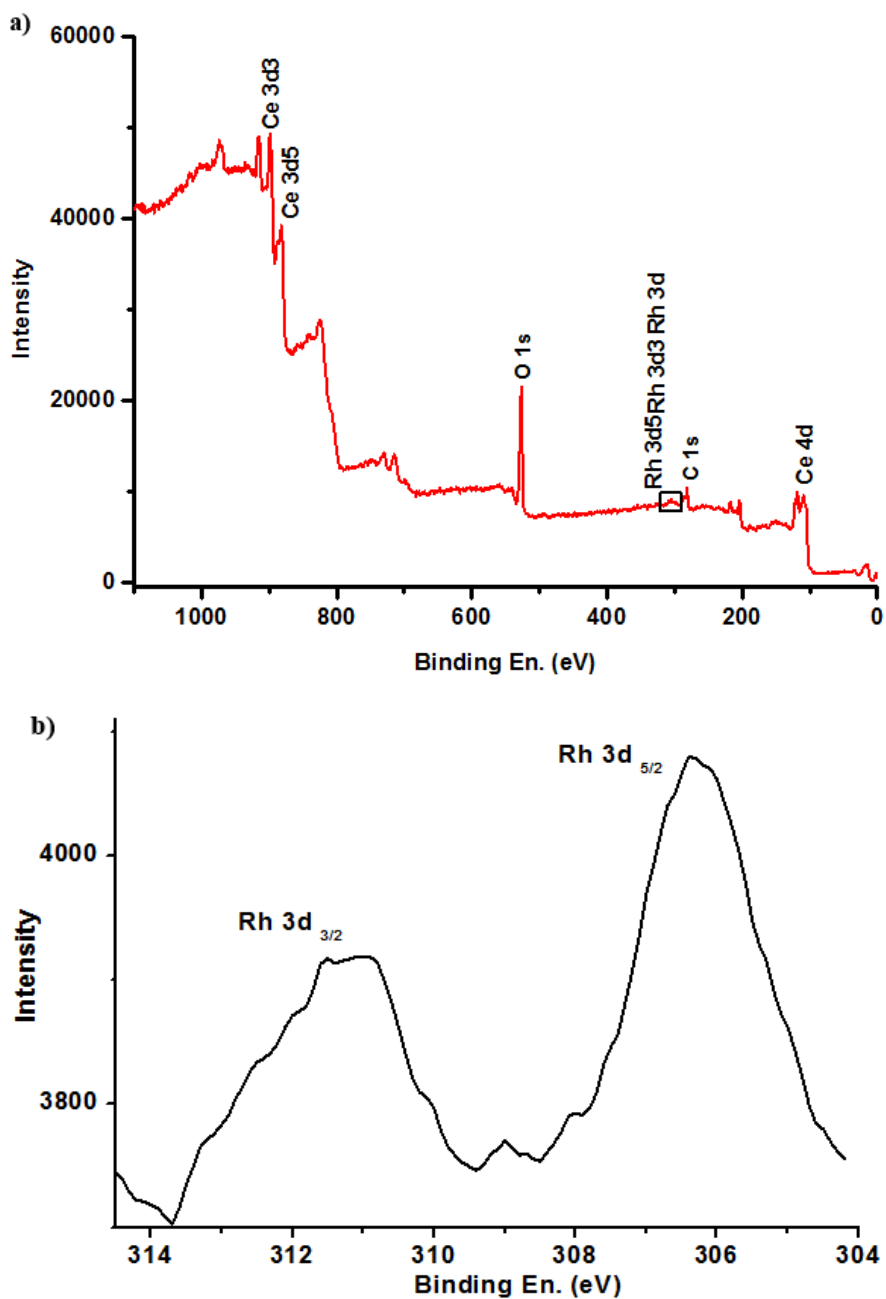


Figure 54. a) X-ray photoelectron (XPS) survey scan spectrum, b) high resolution Rh 3d XPS spectrum of Rh(0)/nanoCeO₂ with a rhodium loading of 1.0% wt. Rh.

Additionally, Figure 55 shows the high resolution Ce 3d XPS scan of various nanoceria samples which allows to investigate the surface composition of ceria in terms of relative concentration of Ce³⁺ and Ce⁴⁺ ions. Cerium(III) defects can easily

be formed on the surface of cerium oxides due to the high positive standard potential of $\text{Ce}^{4+} \rightarrow \text{Ce}^{3+}$ (1.76 eV in acidic solution) [139]. The catalytic reaction conditions can promote the interconversion of two oxidation states of cerium [157]. The high resolution Ce 3d XPS spectra in Figure 55 exhibit two prominent peaks at 885.0 and 879.0 eV for cerium(IV) ions and a characteristic peak at 883.0 eV assigned to cerium(III) ions for all the ceria samples, though in different relative intensities. The relative intensity of Ce^{3+} peak increases on passing from bare cerium oxide to the ceria treated with AB in methanol for 10 min or Rh(0)/nanoCeO₂ samples with different rhodium loading. This observation indicates that the concentration of Ce^{3+} ions on the ceria surface increases during the methanolysis reaction; that is, under catalytic conditions. The increase in Ce^{3+} concentration explains the consumption of AB for the reduction of Ce^{4+} to Ce^{3+} during the catalytic reaction. Therefore, the amount of H₂ gas collected during the catalytic methanolysis is slightly less than 3.0 equivalent H₂ per mole of AB (*vide infra*). It is noteworthy that the relative intensity of Ce^{3+} peak at 883.0 eV decreases as the rhodium loading is increased from 1.0 to 4.0 % wt. Rh (Figure 55c and d). This may be due the partial coverage of surface defects by the increasing rhodium(0) nanoparticles on the surface of nanoceria.

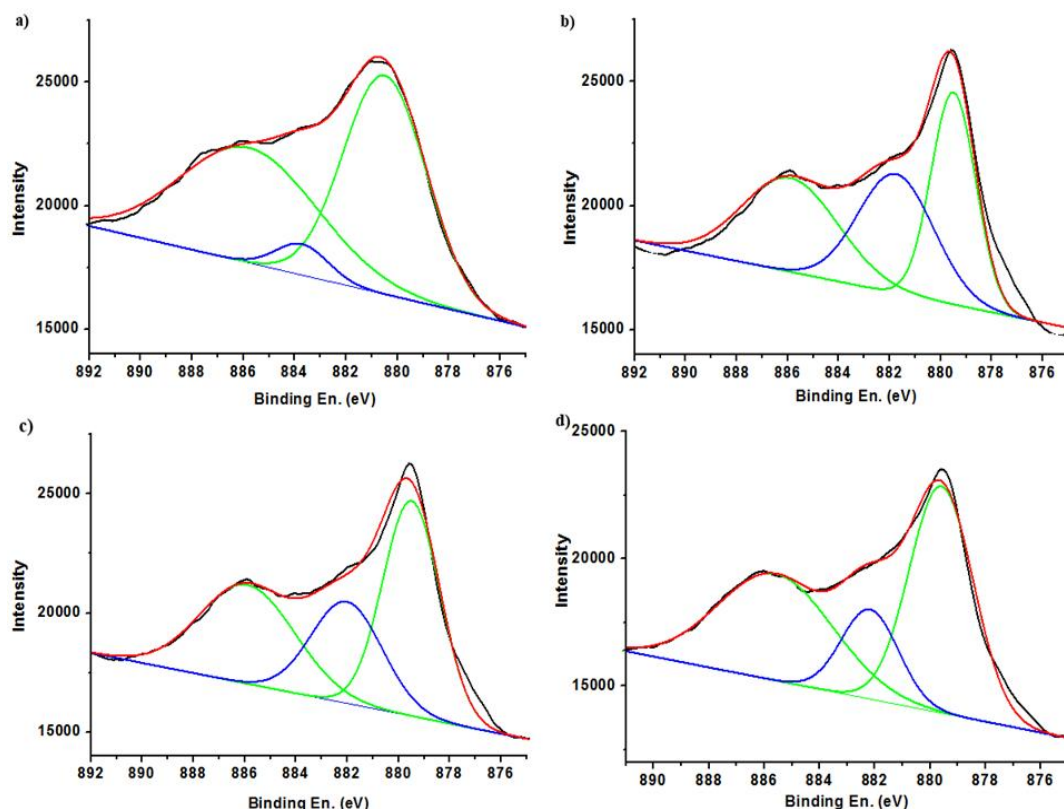


Figure 55. High resolution Ce 3d XPS spectrum of a) bare nanoceria, b) nanoceria treated with AB in methanol, and Rh(0)/nanoCeO₂ with a rhodium loading of c) 1.0% wt. Rh, and d) 4.0 % wt. Rh.wt.

Rh(0)/nanoCeO₂ sample was also analyzed by SEM technique in order to examine the surface morphologies of active catalyst. Figure 56a gives the SEM image of Rh(0)/nanoCeO₂ with a rhodium loading of 1.0 wt. % Rh. which shows no bulk rhodium metal formation in noticeable size on the surface of nanoceria. SEM-EDX spectrum in Figure 56b confirms the presence of rhodium in addition to the framework elements of ceria (Ce, O).

N₂-adsorption-desorption analysis was performed for both nanoceria and Rh(0)/nanoCeO₂ with a rhodium loading of 1.0 wt.% Rh and surface areas were determined to be 48.1 and 37.0 m²g⁻¹, respectively. The slight decrease in the surface area of nanoceria can be interpreted as supplementary evidence for the existence rhodium(0) nanoparticles on the surface of nanoceria [92].

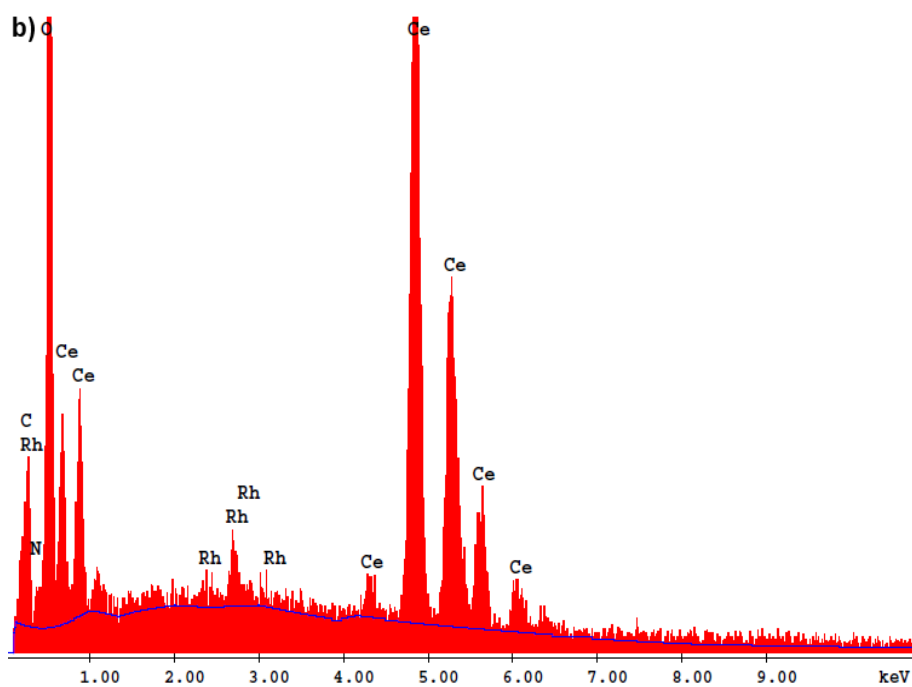
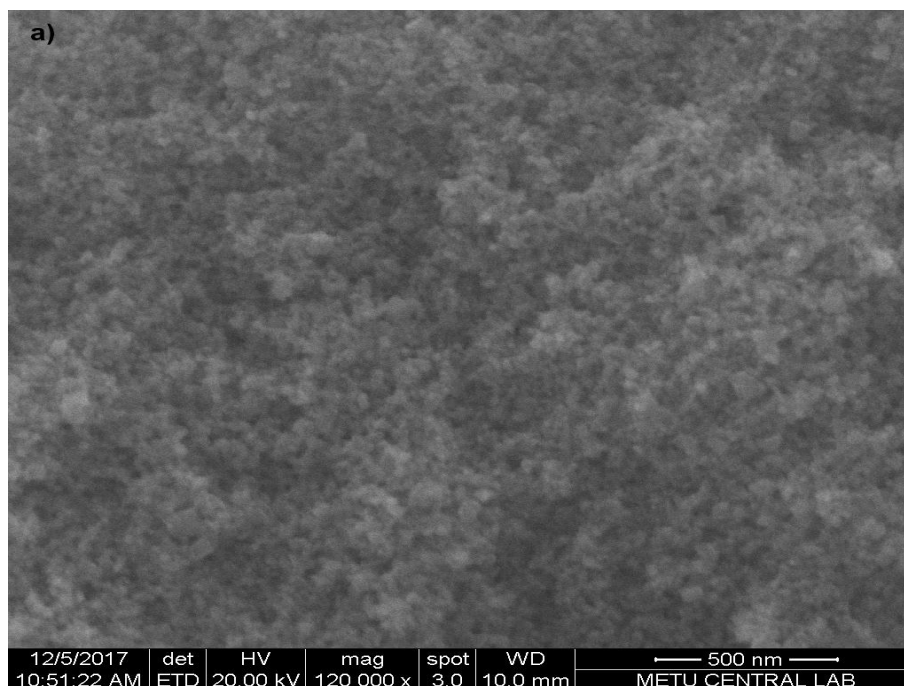


Figure 56. a) SEM image of Rh(0)/nanoCeO₂ b) SEM-EDX spectrum of Rh(0)/nanoCeO₂ with a rhodium loading of 1.0% wt. Rh.

5.4.2. The Catalytic Activities of Rhodium(0) Nanoparticles Supported on Nanoceria in Hydrogen Generation From the Methanolysis of Ammonia Borane

5.4.2.1. Kinetic Studies and Determination of Activation Parameters for the Methanolysis of Ammonia Borane Catalyzed by Rhodium(0) Nanoparticles Supported on Nanoceria

Rh(0)/nanoCeO₂ were *in situ* formed from the reduction of rhodium(II) ions impregnated on nanoceria during the methanolysis of AB. When AB solution is added to a suspension of Rh(II)/nanoCeO₂ in methanol, both reduction of rhodium(II) ions to rhodium(0) and H₂ gas evolution from the methanolysis of AB occur concomitantly. The progress of rhodium(0) nanoparticle formation and methanolysis of AB could be followed by monitoring the volume of H₂ gas, which was then converted into the equivalent H₂ per mole of AB, using the known 3:1 H₂/AB stoichiometry. Figure 57 depicts the graph of mol H₂ evolved per mole of AB *versus* time for the methanolysis of 200 mM AB catalyzed by 0.49 mM Rh (50 mg of Rh(II)/nanoCeO₂, 1.0 wt. % Rh) in 10 mL methanol at 25.0 ± 0.5 °C. H₂ evolution starts after a short induction time less than 1 min and proceeds almost linearly until the complete consumption of AB in the reaction flask. Note that the amount H₂ gas collected is slightly less than 3.0 equivalents per mole of AB because some amount of AB is consumed to reduce Ce⁴⁺ ions to Ce³⁺ on the surface of ceria (see the results of XPS). Then, the remaining AB undergoes the methanolysis to release H₂ gas in the presence of Rh(0)/nanoCeO₂. The initial pale blue color of reaction solution turned to black during the induction period. The color change and the sigmoidal shape of hydrogen generation curve indicate that the formation of rhodium(0) nanoparticles follows the Finke-Watzky (F-W) 2-step mechanism of slow, continuous nucleation and then, autocatalytic surface growth given in Scheme 1 (on page 63) [120,121]. Eqn. 4 (on page 63) can be used to fit the experimental data in Figure 57 to the F-W 2-step mechanism yielding the rate constants $k_1 = 9.6 \times 10^{-2} \text{ min}^{-1}$ and $k_2 = 3.8 \times 10^1 \text{ M}^{-1} \text{ min}^{-1}$ for slow, continuous nucleation and autocatalytic surface growth of rhodium(0) nanoparticles, respectively. The large value of k_2/k_1 ratio (5.6×10^2) implies on the high level of kinetic control of the nanoparticles formation [120].

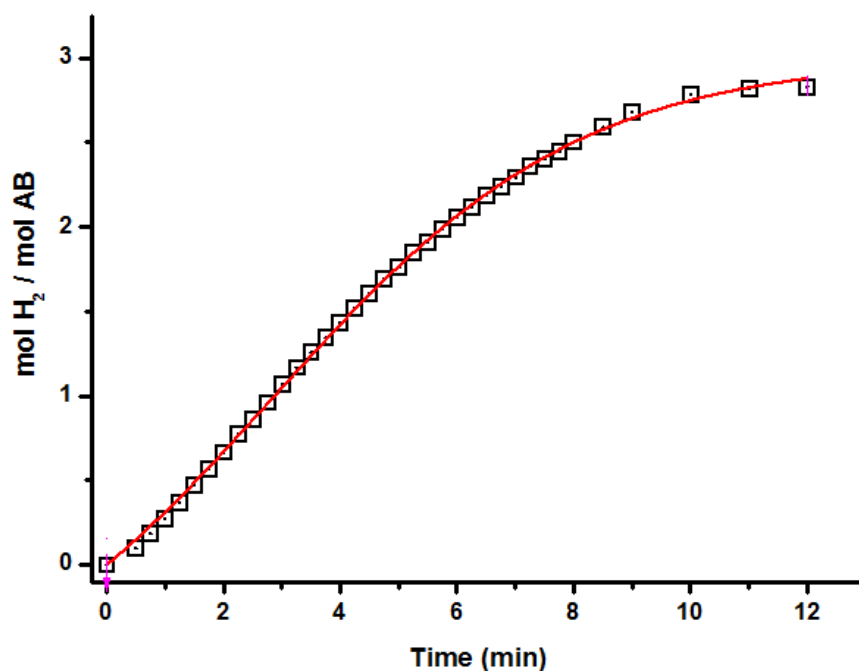


Figure 57. Plot of mol H₂ evolved per mole of AB *versus* time for the catalytic methanolysis of AB starting with 200 mM AB and 50 mg of Rh(II)/nanoCeO₂ (1.0 wt.% Rh, [Rh]= 0.49 mM) in 10 mL methanol at 25.0 ± 0.5 °C. The red curve shows the fit of data to the F-W 2-step mechanism of nanoparticle formation.

The catalytic performance of Rh(0)/nanoCeO₂ in hydrogen generation from the methanolysis of AB was extraordinary even in low rhodium concentration at 25.0 ± 0.5°C. In order to find out the effect of rhodium concentration on hydrogen generation rate, the catalytic methanolysis of AB was performed studying with 200 mM AB in different rhodium loading, thus in different rhodium concentration at 25.0 ± 0.5 °C. The related plots of mol H₂ evolved per mole of AB *versus* time during the catalytic methanolysis of 200 mM AB were given in Figure 58. In all cases, hydrogen generation launches after a short induction time and continues almost linearly until the complete consumption of AB present in the solution. Note that the linear portion of plots presents the constant hydrogen generation rate which indicates the structure insensitivity of methanolysis of AB catalyzed by Rh(0)/nanoCeO₂ as well as the presence of a zero order reaction with respect to the concentration of AB substrate. Kinetic data in Figure 58 fit well to F-W 2-step mechanism yielding the

rate constants k_1 and k_2 for the nucleation and autocatalytic growth of nanoparticle formation [120], which are listed in Table 5 together with the rate of hydrogen generation and turnover frequency values calculated from the plots in Figure 58. The comparison of initial TOF values shows that Rh(0)/nanoCeO₂ with rhodium concentration of 0.49 mM Rh (1.0 wt. % Rh) exhibits the highest catalytic activity with an initial TOF value of 144 min⁻¹ (496 min⁻¹ corrected for surface Rh atoms). Plotting the hydrogen generation rate *versus* the initial rhodium concentration, both in logarithmic scale, gives straight line with a slope of 0.95 \approx 1.0 (The inset of Figure 58) indicating that the methanolysis of AB catalyzed by Rh(0)/nanoCeO₂ is first order with respect to rhodium concentration.

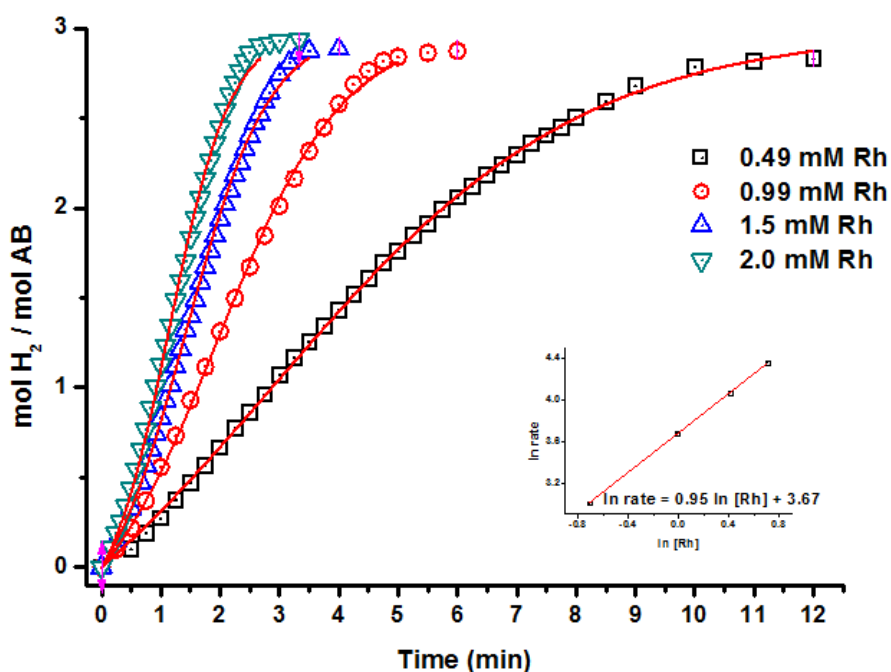


Figure 58 . Plots of mol H₂ evolved per mole of AB *versus* time for methanolysis of 200 mM AB in different metal concentrations ([Rh] = 0.49, 0.99, 1.5 and 2.0 mM, each prepared using metal loading of 1.0, 2.0, 3.0, 4.0% wt. Rh, respectively) at 25.0 \pm 0.5 $^{\circ}$ C. Inset: Plot of hydrogen generation rate *versus* the concentration of rhodium (both in logarithmic scale.).

Table 5. The rate constants k_1 of the slow, continuous nucleation, $P \rightarrow Q$, and k_2 of the autocatalytic surface growth, $P + Q \rightarrow 2Q$, for the formation of rhodium(0) nanoparticles catalyst from the reduction of rhodium(II) ions during the methanolysis of AB (200 mM) starting with Rh(II)/nanoCeO₂ having different rhodium loading, rhodium concentrations, hydrogen generation rates, turnover frequency (TOF) values at 25.0 ± 0.5 °C.

wt.%Rh	[Rh] (mM)	k_1 (min ⁻¹)	k_2 (M ⁻¹ min ⁻¹)	k_2 / k_1	H ₂ generation rate (mmol.min ⁻¹)	TOF (min ⁻¹)
1.0	0.49	$(9.58 \pm 0.14) \times 10^{-2}$	39.0 ± 0.8	407	0.75	144
2.0	0.99	$(12.9 \pm 0.54) \times 10^{-2}$	56.3 ± 1.9	436	1.47	134
3.0	1.5	$(16.6 \pm 0.44) \times 10^{-2}$	57.9 ± 1.1	349	2.18	128
4.0	2.0	$(18.8 \pm 0.76) \times 10^{-2}$	59.9 ± 1.6	317	2.76	122

Figure 59 shows the plots of mol H₂ evolved per mole of AB *versus* time for the methanolysis of AB starting with 200 mM AB plus 50.0 mg Rh(II)/nanoCeO₂ precatalyst in different rhodium loading (1.0, 2.0 and 3.0 wt. % Rh) at different temperatures (20, 25, 30 and 35 °C). The rate constants k_1 for the slow, continuous nucleation and k_2 for the autocatalytic surface growth could be obtained by fitting the kinetic data to the F-W 2-step mechanism (Eqn. 4) and listed in Table 6. From the temperature dependent rate constants one can calculate the activation energies for the individual nucleation and autocatalytic surface growth steps of rhodium(0) nanoparticle formation for each rhodium concentration by using the Arrhenius equation. The resulting activation energy values are also listed in Table 6. Inspection of the data listed in Table 6 ascertains the following points: (i) the rate constant k_1 value increases with increasing temperature for each rhodium loading and, parallel to this, the induction period decreases with increasing temperature as the induction period has been shown to be inversely proportional to the nucleation rate constant [120]. (ii) Similarly, the rate constant k_2 value increases with the increasing temperature for each rhodium loading. (iii) One observes a general trend of increasing k_1 and k_2 values with the increasing rhodium loading at each temperature. (iv) While a general trend of decreasing activation energy for the autocatalytic surface growth step is noted as the rhodium loading increases, no trend is noticeable in the activation energy for the nucleation step of nanoparticle formation.

Activation parameters for the methanolysis of AB catalyzed by Rh(0)/nanoCeO₂ can be determined from the temperature dependent kinetic data displayed in Figure 59 for each rhodium concentration. The reaction rate constant k_{obs} of the methanolysis can be obtained from the slope of the linear part of each hydrogen generation *versus* time plot at different temperatures. Activation energy obtained using Arrhenius equation is 75.0 ± 2.0 , 71.9 ± 2.0 and 64.6 ± 2.0 kJ.mol⁻¹ for the catalytic methanolysis reaction catalyzed by Rh(0)/nanoCeO₂ with the rhodium loading of 1.0, 2.0 and 3.0 % wt. Rh, respectively. The increase in rhodium concentration causes a noticeable decrease in the activation energy for the catalytic methanolysis of AB.

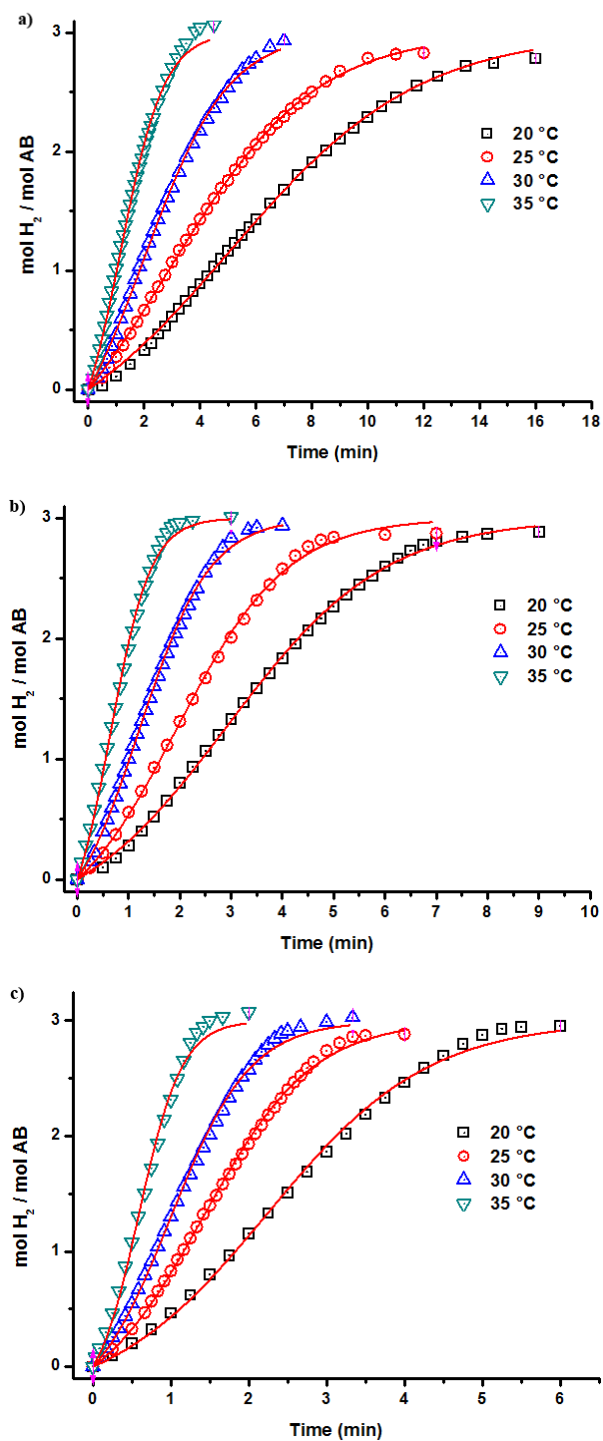


Figure 59. Plots of mol H₂ evolved per mole of AB *versus* time for the catalytic methanolsis of AB at various temperatures in the range of 20 – 35 °C keeping the concentration of substrate at [AB] = 200 mM and varying the concentration of rhodium a) 1.0 wt. % Rh, [Rh] = 0.49 mM b) 2.0 wt. % Rh, [Rh] = 0.99 mM c) 3.0 wt. % Rh, [Rh]= 1.5 mM, respectively.

Table 6. The rate constants k_1 of the slow, continuous nucleation, $P \rightarrow Q$, and k_2 of the autocatalytic surface growth, $P + Q \rightarrow 2Q$, for the formation of rhodium(0) nanoparticles catalyst from the reduction of rhodium(II) ions during the methanolysis of AB, k_{obs} values for the catalytic methanolysis reaction, activation energies for the nucleation and autocatalytic surface growth steps as well as the methanolysis of AB catalyzed by Rh(0)/nanoCeO₂ having different rhodium concentrations.

[Rh]	0.49 mM			0.99 mM			1.5 mM		
Temperature (K)	k_1	k_2	k_{obs}	k_1	k_2	k_{obs}	k_1	k_2	k_{obs}
293	$5.41 \times 10^{-2} \pm 1.11 \times 10^{-3}$	32.6 ± 0.8	1.50	$8.40 \times 10^{-2} \pm 1.99 \times 10^{-3}$	38.2 ± 0.7	1.49	$9.95 \times 10^{-2} \pm 5.41 \times 10^{-3}$	39.3 ± 1.4	1.28
298	$9.60 \times 10^{-2} \pm 1.44 \times 10^{-3}$	38.5 ± 0.8	2.24	$1.31 \times 10^{-1} \pm 5.36 \times 10^{-3}$	53.8 ± 1.8	2.05	$1.67 \times 10^{-1} \pm 4.22 \times 10^{-3}$	57.1 ± 1.1	1.98
303	$1.38 \times 10^{-1} \pm 3.40 \times 10^{-3}$	71.9 ± 2.0	3.78	$2.13 \times 10^{-1} \pm 5.03 \times 10^{-3}$	83.7 ± 1.7	3.35	$2.46 \times 10^{-1} \pm 9.87 \times 10^{-3}$	77.2 ± 2.4	2.82
308	$2.41 \times 10^{-1} \pm 9.11 \times 10^{-3}$	139.1 ± 5.6	6.69	$4.15 \times 10^{-1} \pm 1.98 \times 10^{-2}$	142.7 ± 6.1	6.26	$3.83 \times 10^{-1} \pm 3.34 \times 10^{-2}$	146 ± 8.9	4.95
Activ. En. (kJ/mol)	73.5	74.4	75.0	79.1	65.9	71.9	66.5	63.5	64.6

5.4.2.2. Catalytic Lifetime of Rhodium(0) Nanoparticles Supported on Nanoceria in Hydrogen Generation From the Methanolysis of Ammonia Borane

Total turnover number (TTO) of Rh(0)/nanoCeO₂ in the methanolysis of AB was determined in a catalytic lifetime experiment starting with 10 mL suspension of Rh(II)/nanoCeO₂ containing 0.49 mM Rh (50.0 mg Rh(0)/nanoCeO₂, 1.0 wt. %Rh) and 200 mM AB at 25.0 ± 0.5 °C (Figure 60). When hydrogen generation tends to stop, a new batch of AB was added into reaction flask. This procedure was continued until no more H₂ gas evolution was observed. Rh(0)/nanoCeO₂ provided a minimum of 5400 turnovers over 24 h before deactivation with an initial turnover frequency (TOF) value of 144 min⁻¹ in hydrogen generation from the methanolysis of AB 25.0 ± 0.5 °C [158]. As anticipated, the TOF value decreases in course of lifetime experiment and reaches the minimum, may be, owing to the viscose form of reaction solution due to the continuous addition of AB or deactivating effect of boron containing by products. Rh(0)/nanoCeO₂ provides the lower initial turnover frequency (TOF) value compared to our previously reported rhodium catalysts in the same reaction: Rh(0)/nanoHAP (TOF = 147 min⁻¹) [159], Rh(0)/nanoSiO₂ (TOF = 168 min⁻¹) [160] or Rh(0)/nanoAl₂O₃ (TOF = 218 min⁻¹) [161]. However, this value is still higher than TOFs of the other catalysts reported in literature for the same reaction: RhCl₃ (TOF = 100 min⁻¹) [29], zeolite confined rhodium(0) nanoparticles (TOF = 30 min⁻¹) [41] or the others such as MMT-immobilized ruthenium(0) nanoparticles (TOF = 90.9 min⁻¹) [42], graphene supported ruthenium(0) nanoparticles (TOF = 99.4 min⁻¹) [48].

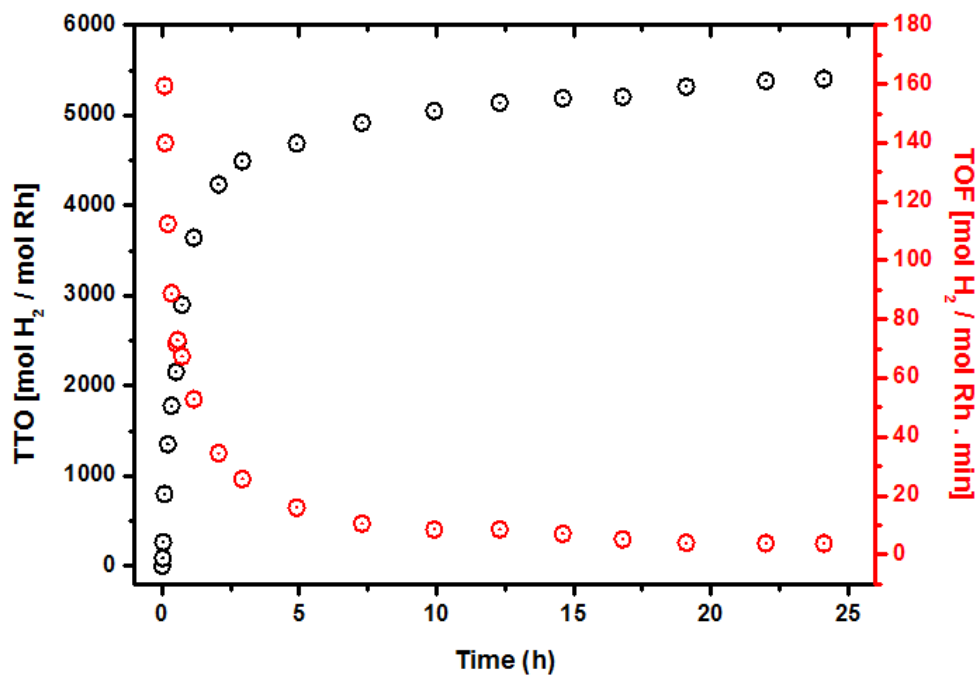


Figure 60. Plot of total turnover number (TTO) or turnover frequency *versus* time for the methanolysis of AB with 10 mL solution of 0.49 mM Rh (50.0 mg Rh(0)/nanoCeO₂, 1.0 wt.% Rh,) and 200 mM AB (for each run) at 25.0 ± 0.5 °C.

5.4.2.3. Leaching Test for Rhodium(0) Nanoparticles Supported on Nanoceria in the Methanolysis of Ammonia Borane

An important issue in working with the supported nanoparticle catalysts is to check whether the nanoparticles are chemically transferred from the support surface to the solution during the catalytic reaction, where they may continue to contribute to the catalysis. In the present study, the hydrogen generation from the methanolysis of AB is expected to be stopped by the removal of Rh(0)/nanoCeO₂ catalyst from the reaction medium if there is no leaching of rhodium from the ceria surface to the solution. Such a control experiment was performed starting with 200 mM AB plus 50 mg Rh(II)/nanoCeO₂ (1.0 % wt. Rh, [Rh] = 0.49 mM) in 10 mL methanol at 25.0 ± 0.5 °C. After the complete methanolysis of AB, solid Rh(0)/nanoCeO₂ was allowed to settle down then, supernatant solution was transferred *via* a gas tight syringe into another reaction flask under inert gas atmosphere. A new batch of solid AB was

added to supernatant solution and the solution was stirred for an hour at 25.0 ± 0.5 °C. During that period, no hydrogen gas evolution was observed indicating that rhodium(0) nanoparticles are well stabilized on the surface of nanoceria; thus no rhodium leaches from the surface of nanoceria into the reaction solution during methanolysis. The supernatant solution was also examined by ICP-OES analysis to detect rhodium present in the solution; the rhodium concentration in supernatant solution is found to be 0.008 mM which is negligible compared to the initial rhodium concentration of 0.491 mM in the reaction solution. Therefore, it can be concluded that Rh(0)/nanoCeO₂ is kinetically competent and heterogeneous catalyst in the methanolysis of AB.

CHAPTER 6

CONCLUSIONS

Ammonia borane (AB) has been considered as potential hydrogen storage materials because of its exceptional properties: AB is solid under ambient conditions due to short $\text{NH}\cdots\text{HB}$ intermolecular attraction that provides extra stability under inert atmosphere and at room temperature. Among the hydrogen production methods from AB, methanolysis appears to be an efficient way to release H_2 gas and also has outscored the other H_2 releasing ways because of the recyclability of reaction products and no ammonia gas evolution during reaction. However, methanolysis of AB needs an efficient catalyst to liberate hydrogen stored in it. The aim of this thesis was to develop highly active and stable rhodium(0) nanoparticle catalysts for hydrogen generation from the methanolysis of ammonia borane. Rhodium(0) nanoparticles were stabilized by supporting them on the surface of oxide nanopowders (Rh(0)/nanooxides); hydroxyapatite, silica, alumina or ceria, then characterized by using a combination of advance analytical techniques and their catalytic activities were examined in hydrogen generation from the methanolysis of AB.

The main finding and insights from our study of the preparation, characterization, and catalytic use of rhodium(0) nanoparticles supported on surface of oxide nanopowders for the methanolysis of AB can be summarized as follows:

- Rhodium(0) nanoparticles supported on the surface of oxide nanopowders were reproducibly prepared by a facile method comprising the impregnation of rhodium(II) or rhodium(III) ions on the surface of oxide nanopowders and then, *in situ* reduction by ammonia borane during the methanolysis reaction.

- Rhodium(0) nanoparticles supported on the surface of oxide nanopowders could be isolated from the reaction solution as powder and they are found to be catalytically active in hydrogen generation from the methanolysis of ammonia borane.
- The characterization of rhodium(0) nanoparticles supported on the surface of oxide nanopowders by using advanced analytical techniques reveals the formation of uniformly dispersed rhodium(0) nanoparticles on the surface of oxide nanopowders with narrow particle size distributions.
- The mean particle sizes of rhodium(0) nanoparticles on the surface of hydroxyapatite nanospheres and nanoceria were determined to be 4.7 ± 0.8 and 3.9 ± 0.6 nm, respectively, which are almost independent of metal concentration. In contrast to the nanohydroxyapatite and nanoceria supports, the particle size of rhodium(0) nanoparticles on the surface of nanosilica and nanoalumina show dependency on the initial concentration of rhodium precursor. The increase in rhodium concentration causes the formation of larger rhodium nanoparticles, thus the particle size of rhodium(0) nanoparticles can be tuned by changing the initial concentration of rhodium precursor.
- All the rhodium(0) nanoparticles supported on hydroxyapatite nanospheres, nanosilica, nanoalumina and nanoceria were highly active catalyst in hydrogen generation from the methanolysis of ammonia borane providing exceptional initial turnover frequencies of 147, 168, 218 and 144 min^{-1} and total turnover numbers of 26,000, 10,000, 16,300 and 5400 at 25.0 ± 0.5 °C, respectively. The small particle size of both rhodium(0) nanoparticles, less than 5.0 nm, and oxide support materials, less than 100 nm, providing more external surface area for the stabilization of rhodium(0) nanoparticles are the most important reasons for the high activity and long lifetime of four catalysts in hydrogen generation from the methanolysis of ammonia borane.

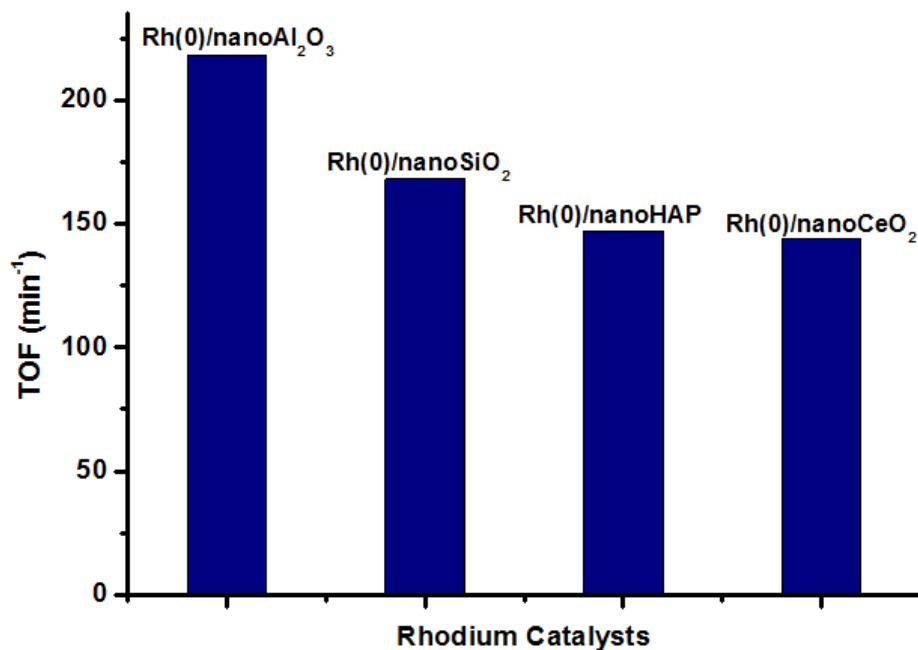


Figure 61. Comparison of catalytic activities of rhodium nanoparticles supported on nanooxide crytalline support materials in hydrogen generation from the methanolysis of ammonia borane at 25.0 ± 0.5 °C.

- The hydrogen generation graphs of AB methanolysis catalyzed by rhodium(0) nanoparticles supported on nanosilica, nanoalumina and nanoceria present sigmoidal kinetic curves which give valuable insights about the kinetics of nanoparticle formation explained by Finke-Watzky 2-step mechanism consisting of slow, continous nucleation (rate constant, k_1) and autocatalytic surface growth (rate constant, k_2). The sigmoidal shape of hydrogen production curve and its curve-fit to kinetics of Finke-Watzky 2-step mechanism are very strong evidence for the formation of rhodium(0) nanoparticles from the reduction of rhodium(II) ions in the presence of ammonia borane as reducing agent. The high values of k_2/k_1 ratio obtained in the experiments with different rhodium concentrations and at different temperatures are indicative of a high level kinetic control in the formation of rhodium(0) nanoparticles

from the reduction of rhodium(II) precursor impregnated on the surface of oxide nanopowders.

- Rhodium(0) nanoparticles supported on hydroxyapatite nanospheres, nanosilica and nanoalumina provide 3.0 equivalents H_2 per mole AB in all runs of the methanolysis reaction. However, the methanolysis of AB catalyzed by rhodium(0) nanoparticles supported on nanoceria liberates slightly less than 3.0 equivalents H_2 per mole of AB because of the consumption of some amount of ammonia borane initially added to the reaction medium for the reduction of Ce^{4+} to Ce^{3+} during the catalytic reaction.
- Of the four oxides used for supporting rhodium(0) nanoparticles in the present study, nanoceria is distinctly different from the other three, being a reducible oxide and, thus, forming Ce^{3+} defects on the surface under the catalytic reaction conditions. The reduction of Ce^{4+} ions to Ce^{3+} causes accumulation of an excess negative charge on the surface of ceria, which provides favourable interaction between rhodium(0) nanoparticles and ceria support, thus, metal(0) nanoparticles can strongly bind the surface of support. The formation of Ce^{3+} defects could be confirmed by the XPS analysis which shows the increase in Ce^{3+} concentration on the surface of nanoceria after the catalytic methanolysis of ammonia borane.
- All the methanolysis reactions catalyzed by the oxide supported rhodium(0) nanoparticles are found to be first order with respect to catalyst concentration and zero order in substrate concentration.
- The activation energies of methanolysis of ammonia borane catalyzed by rhodium(0) nanoparticles supported on hydroxyapatite nanospheres, nanosilica and nanoalumina were determined to be 56 ± 2 kJ/mol, 62 ± 2 kJ/mol, 62 ± 2 kJ/mol, respectively. The variation of activation energy for the methanolysis of ammonia borane catalyzed by rhodium(0) nanoparticles supported on nanoceria could be examined by doing a series experiments with different rhodium loading on nanoceria at different temperatures to understand the effects of rhodium loading on activation energy and kinetics of the reaction. There was a decreasing

trend in activation energy from 75 ± 2 to 65 ± 2 kJ/mol with increasing rhodium loading from 1.0 to 3.0 % wt. Rh.

- The results of both poisoning and leaching tests reveal that rhodium(0) nanoparticles supported on the surface of oxide nanopowders are kinetically competent catalyst in hydrogen generation from the methanolysis of ammonia borane and the catalytic methanolysis is a heterogeneous catalysis.
- In the literature, there are different proposed mechanisms for the catalytic hydrolysis of AB, however; the mechanism for hydrogen generation from the methanolysis of AB has not been discussed yet. The mechanism for the catalytic hydrolysis of AB suggested by Chandra et al. [162] and Chen et al. [163] could also be a plausible mechanism for the catalytic methanolysis of AB. It is reasonable to suggest that AB molecule interacts with metal nanoparticle surface to form an activated complex. The formed activated species is attacked by a CH_3OH molecule, which causes the concerted dissociation of B-N bond and methanolysis of the resultant BH_3 intermediate to produce $\text{B}(\text{OCH}_3)_4^-$ ion together with H_2 gas generation. Additionally, the large negative values of activation entropy calculated for the methanolysis of AB catalyzed by Rh(0)/nanooxides are also indicative of associative mechanism for the methanolysis of AB catalyzed by rhodium(0) nanoparticles.
- Table 7 summarizes the results of catalytic activities in TOF and catalyst lifetime of metal(0) catalysts used for the catalytic methanolysis of ammonia borane and activation energies of catalytic methanolysis of ammonia borane to make a better comparison for our prepared catalysts with the literature data.
- The comparison of catalytic activities of four rhodium(0) nanoparticle catalysts with the literature values reveals that rhodium(0) nanoparticles supported on the surface of nanoalumina is the second best catalyst with an excellent initial turnover frequency of 218 min^{-1} and 16,300 turnovers after the AgPd alloy ($\text{TOF}=366.4 \text{ min}^{-1}$) [49] and the rhodium(0) nanoparticles supported on nanosilica is the third best

catalyst with an initial turnover frequency of 168 min^{-1} and 10,000 turnovers in hydrogen generation from the methanolysis of ammonia borane.

- Up to now, many heterogeneous catalysts have been tested in hydrogen generation from the methanolysis of ammonia borane, the bimetallic AgPd alloy appears to have the highest catalytic activity in this hydrogen generation reaction. Bimetallic alloy nanoparticles provide better activities than those of either component alone due to the synergistic effects. For future work, bimetallic nanoparticles of rhodium can be *in situ* prepared in the presence of oxide nanopowders and then, their catalytic activities can be examined in hydrogen generation from the methanolysis of ammonia borane. The purpose of using bimetallic nanoparticles is to increase the catalytic activity because of synergistic effect and to reduce the cost of precious rhodium by diluting with a nonnoble metal such as nickel, cobalt or copper.

Table 7. Catalytic activities in terms of turnover frequency (TOF) and catalyst lifetime in terms of total turnover number (TTO) of transition metal(0) catalysts in hydrogen generation from the methanolysis of ammonia borane as well as the activation energies of the catalytic methanolysis of ammonia borane.

Catalyst	Size of NPs (nm)	TOF (min ⁻¹)	Activation energy, E _a (kJ.mol ⁻¹)	Total turnover numbers (TTO)	Ref.
RhCl ₃	-	100	-	-	[29]
RuCl ₃	-	150	-	-	[29]
CoCl ₂	-	3.7	-	-	[29]
NiCl ₂	-	2.9	-	-	[29]
PdCl ₂	-	1.5	-	-	[29]
Pd/C	-	1.9	-	-	[29]
Nano Cu ₂ O	7.1	0.2	-	-	[36]
Nano Cu@Cu ₂ O	7.7 ± 1.8	0.16	-	-	[36]
PVP-stabilized Ni	3.0 ± 0.7	12.1	62 ± 2	14500	[37]
PVP-stabilized Pd	3.2 ± 0.5	22.3	35 ± 2	23000	[38]
PVP-stabilized Ru	2.4 ± 1.2	47.7	58 ± 2	71500	[39]
Co-Co ₂ B	4.0 - 8.0	7.5	-	-	[40]
Ni-Ni ₃ B	4.0 - 8.0	5.0	-	-	[40]
Co-Ni-B	5.0 - 8.0	10.0	-	-	[40]
Zeolite confined Rh	-	30.0	40 ± 2	74300	[41]
MMT stabilized Ru	~5.0	90.9	23.8	-	[42]
Co ₄₈ Pd ₅₂ /C	7.0 ± 0.5	27.7	25.5	-	[43]
CuPd alloy	11.9 ± 0.8	53.2	-	-	[44]
mesoporous CuO	-	2.41	34.2 ± 1.2	-	[45]
Cu-Cu ₂ O-CuO/C	3.8 ± 1.7	24.0	67.9	-	[46]
b-CuO NA/CF	~100	13.3	34.7	-	[47]
Ru/graphene	1.57	99.4	54 ± 2	35600	[48]
AgPd alloy	6.2 ± 0.3	366.4	37.5	-	[49]
G-Cu ₃₆ Ni ₆₄	16.0 ± 0.1	49.1	24.4	-	[50]
Rh/CC3-R-homo	1.1 ± 0.2	215.3	-	-	[51]
Rh/CC3-R-hetero	-	65.5	-	-	[51]
Pd/GNS	3.68 ± 0.35	101 (254) ^a	46	-	[52]
Rh(0)/nanoHAP (2.09 wt. % Rh)	4.7 ± 0.8	147	56 ± 2	26000	This study
Rh(0)/nanoSiO ₂ (2.0 wt.% Rh)	4.4 ± 0.7	168 (652) ^a	62 ± 2	10000	This study
Rh(0)/nanoAl ₂ O ₃ (0.50 wt.% Rh)	3.6 ± 0.4	218 (692) ^a	62 ± 2	16300	This study
Rh(0)/nanoCeO ₂ (1.0 wt.% Rh)	3.9 ± 0.6	144	75 ± 2	5300	This study

^a the value corrected for the number of rhodium atom on the surface of nanoparticle.

REFERENCES

- [1] Rand D. A. J, Dell R. M., *Hydrogen Energy Challenges and Prospects*, RSC Publishing, Cambridge, **2008**.
- [2] Sahaym U. , Norton M. G., *J Mater Sci*, **2008**, 43, 5395.
- [3] Satyapal S., Petrovic J., Thomas G., *Sci. Am.* 2007, 296, 80.
- [4] Dresselhaus M.S., Thomas I.L., *Nature* 2001, 414, 332.
- [5] Gandia L. M., Arzamendi G., Dieguez P. D., *Renewable Hydrogen Technologies*, Elsevier, **2013**.
- [6] Balat, M., *Energy Sources Part A*, **2005**, 27, 569.
- [7] Armaroli N., Balzani V., *ChemSusChem*, **2001**, 4, 21.
- [8] Züttel A., Borgschulte A., Schlapbach L., *Hydrogen as a Future Energy Carrier*, Wiley-VCH, Weinheim, **2008**.
- [9] Schlapbach L., Züttel A., *Nature*, **2001**, 414, 353.
- [10] Jones R. H., Thomas, G., *J. Min. Met. Mats.*, **2007**, 59, 50.
- [11] Sutton A.D., Burrell A.K., Dixon D.A., Garner E.B., Gordon J.C., Nakagawa T., Ott K.C., Robinson J.P., Vasiliuet M., *Science*, **2011**, 331, 1426.
- [12] Hamilton C.W., Baker R.T., Staubitz A., Manners I., *Chem. Soc. Rev.*, **2009**, 38, 279.
- [13] Langmi H.W., McGrady G.S., *Coord. Chem. Rev.*, **2007**, 251, 925.
- [14] Züttel A., *Mater. Today*, **2003**, 6, 24.
- [15] Hausdorf S, Baitalow F, Wolff G, Mertens F., *Int. J. Hydrogen Energy*, **2008**, 33, 608.
- [16] (a) Custelcean, R., Dreger, Z. A., *J. Phys. Chem. B*, **2003**, 107, 9231. (b) Horvath, V., Kovacs A., Hargittai, I., *J. Phys. Chem. A*, **2003**, 107 1197.

- [17] (a) Richardson, T.B., de Gala, S., Crabtree, R.H., *J. Am. Chem. Soc.*, **1995**, 117, 12875. (b) Li, J., Zhao, F., Jing, F., *J. Chem. Phys.*, **2002**, 116, 25.
- [18] Umegaki T., Yan M., Zhang X. B., Shioyama H., Kuriyama N., Xu Q., *Int. J. Hydrogen Energy*, **2009**, 34, 2303.
- [19] Staubitz, A., Robertson, A.P.M., Sloan, M.E., Manners, I. *Chem. Rev.* **2010**, 110, 4023.
- [20] Demirci U.B., Bernard S., Chiriac R., Toche F., Miele P., *J Power Sources*, **2011**, 196, 279.
- [21] Kobayashi T., Gupta S., Caporini M. A., Pecharsky V. K., Pruski M., *J Phys Chem C*, **2014**, 118, 19548.
- [22] Wang P., *Dalton Trans*, **2012**, 41, 4296.
- [23] Jaska C. A., Temple K., Lough A. J., Manners I., *J. Am. Chem. Soc.*, **2003**, 125, 9424.
- [24] Ayvalı T., Zahmakıran M., Özkar S., *Dalton Trans*, **2011**, 40, 3584.
- [25] Yao Q., Lu Z. H., Jia Y., Chen X., Liu X., *Int. J. Hydrogen Energy*, **2015**, 40, 2207.
- [26] Marder T. B., *Angew. Chem Int .Ed.*, **2007**, 46, 8116.
- [27] Lu Z. H., Yao Q., Zhang Z., Yang Y., Chen X., *J. Nanomaterials*, **2014**, Article ID 729029
- [28] Li X., Zeng C., Fan G., *Int. J. Hydrogen Energy*, **2015**, 40, 3883.
- [29] Ramachandran P. V., Gagare P. D., *Inorg. Chem.*, **2007**, 46, 7810.
- [30] Staubitz A., Robertson A. P. M., Manners I., *Chem. Rev.*, **2010**, 110, 4079.
- [31] Zhan W. W., Zhu Q.L., Xu Q., *ACS Catal*, **2016**, 6, 6892.
- [32] Storozhenko P. A., Svitsyn R. A., Ketsko V. A., Buryak A. K., Ul'yanov A. V., *Russ. J. Inorg. Chem.*, **2005**, 50, 980.
- [33] Brockman A., Zheng Y., Gore J., *Int. J. Hydrogen Energy*, **2010**, 35, 7350.
- [34] Lo C. T. F., Karan K., Davis B. R., *Ind. Eng. Chem. Res.*, **2007**, 46, 5478.

- [35] Tan Y., Yu X., *RSC Advances*, **2013**, 3, 23879.
- [36] Kalidindi S. B., Sanyal U., Jagirdar B. R., *Phys. Chem. Chem. Phys.*, **2008**, 10, 5870.
- [37] Özhava D., Kiliçaslan N. Z., Özkar S., *Appl. Catal. B Environ.*, **2015**, 162, 573.
- [38] Erdoğan H., Metin Ö., Özkar S., *Phys. Chem. Chem. Phys.*, **2009**, 11, 10519.
- [39] Erdoğan H., Metin Ö., Özkar S., *Catal. Today*, **2011**, 170, 93.
- [40] Kalidindi S. B., Vernekar A. A., Jagirdar B. R., *Phys. Chem. Chem. Phys.*, **2009**, 11, 770.
- [41] Çalışkan S., Zahmakiran M., Özkar S., *Appl. Catal. B Environ.*, **2010**, 93, 387.
- [42] Bin Dai H., Kang X. D., Wang P., *Int. J. Hydrogen Energy*, **2010**, 35, 10317.
- [43] Sun D., Mazumder V., Metin Ö., Sun S., *ACS Catal.*, **2012**, 2, 1290.
- [44] Li P., Xiao Z., Liu Z., Huang J., Li Q., Sun D., *Nanotechnology*, **2014**, 26, 25401.
- [45] Yao Q., Huang M., Lu Z. H., Yang Y., Zhang Y., Chen X., Yang Z., *Dalt. Trans.*, **2015**, 44, 1070.
- [46] Yurderi M., Bulut A., Ertas I. E., Zahmakiran M., Kaya M., *Appl. Catal. B Environ.*, vol. **2015**, 165, 169.
- [47] Cui L., Cao X., Sun X., Yang W., Liu J., *ChemCatChem*, **2018**, 10, 1.
- [48] Peng S., Liu J., Zhang J., Wang F., *Int. J. Hydrogen Energy*, **2015**, 40, 10856.
- [49] Sun D., Li P., Yang B., Xu Y., Huang J., Li Q., *RSC Adv.*, **2016**, 6, 105940.
- [50] Yu C., Fu J., Muzzio M., Shen T., Su D., Zhu J., Sun S., *Chem. Mater.*, **2017**, 29, 1413.
- [51] Sun J.K., Zhan W.W., Akita T., Xu Q., *J. Am. Chem. Soc.* **2015**, 137, 7063.
- [52] Karataş Y., Gülcan M., Çelebi M., Zahmakiran M., *ChemistrySelect*, **2017**, 2, 9628.
- [53] El-Shall M.S., Abdelsayed V., Khder A.E.R.S., Hassan H.M., El-Kaderi H.M., Reich T.E., *J. Mater. Chem.*, **2009**, 19, 7625.

- [54] Zahmakıran M., Leshkov Y.R., Zhang Y., *Langmuir*, **2011**, 28, 60.
- [55] Rothenberg, G. *Catalysis: Concepts and Green Applications*, Wiley-VCH, Weinheim, **2008**.
- [56] Farnetti E., Monte R.D., Kaspar J., *Inorganic and Bio inorganic Chemistry-Volume 2*, EOLLS Publications, **2009**.
- [57]Chorkendorff I., Niemantsverdriet J. W., *Concepts of Modern Catalysis and Kinetics*, 3rd Edition, Weinheim, Wiley VCH, **2017**.
- [58] Emig, G., *Chemie in unserer Zeit.*, **1987**, 21, 128.
- [59] Cole-Hamilton D., *Science*, **2003**, 299 , 1702.
- [60] Ozin G. A., Arsenault A. C., Cademartiri L., editors. *Nanochemistry: A Chemical Approach to Nanomaterials*, 2nd Edition., Royal Society of Chemistry; **2008**.
- [61] Astruc D., *Nanoparticles and Catalysis*, Weinheim:Wiley-VCH; **2008**.
- [62] Polshettiwar V., Tewodros A., *Nanocatalysis: Synthesis and Applications*, First Edition. , John Wiley & Sons, **2013**.
- [63] Yan, N., Xiao, C., Kou, Y., *Coord. Chem. Rev.*, **2010**, 254, 1179.
- [64] Fahlman, B.D., *Materials Chemistry*, Springer: Mount Pleasant, MI, **2007**.
- [65] C. R. Henry, *Appl. Surf. Sci.*, **2000**, 164, 252.
- [66] Broer M., Heinz K., *Metal Clusters at Surfaces: Structure, Quantum Properties, Physical Chemistry*, Springer, p. 211, **2000**.
- [67] G. Schmid, *Chem. Rev.*, **1992**, 92, 1709.
- [68]Belyakova O. A., Slovokhotov Y.L., *Russ.Chem.Bull., Int.Ed.*, **2003**,. 52, 11.
- [69] Corain, B., Schmid, G., Toshima, N., *Metal Nanoclusters in Catalysis and Materials Science: The Issue of Size Control*, Elsevier B.V., Amsterdam, Netherlands, **2008**.
- [70]Ott L. S., Finke R. G., *Coordination Chemistry Reviews*, **2007**, 251,1075.
- [71] Ninham B. W., *Adv. Coll. Int. Sci.*, **1999**, 83, 1.

- [72] Roucoux A., Schulz J., Patin H., *Chem. Rev.* **2002**, 102, 3757.
- [73] Grubbs, R. B., *Polymer Reviews*, **2007**, 47, 197.
- [74] Pachon, L. D., Rothenberg G., *Appl. Organometal. Chem.*, **2008**, 22, 288.
- [75] Willner, I., Mandler, D., *J. Am. Chem. Soc.*, **1989**, 111, 1330.
- [76] Bönnehan, H., Richards, R. M., *Eur. J. Inorg. Chem.*, **2001**, 10, 2445.
- [77] Tano, T., Esumi, K., Meguro K., *J. Colloid Interface Sci.*, **1989**, 133, 530.
- [78] Esumi, K., Tano, T., Meguro, K., *Langmuir*, **1989**, 5, 268.
- [79] Dhas, N. A., Suslick, K. S., *J. Am. Chem. Soc.*, **2005**, 127, 2368.
- [80] Duteil, A., Queau, R., Chaudret, B., Mazel, R., Roucau, C., Bradley, J. S., *Chem. Mater.*, **1993**, 5, 341.
- [81] Klabunde, K. J., Habdas, J., Cardenas-Trivino, G., *Chem. Mater.*, **1989**, 1, 481.
- [82] (a) Reetz, M. T., Helbig, W., Quaiser, S. A., *In Active Metals: Preparation, Characterization, Applications*, VCH: New York, **1996**. (b) Reetz, M. T., Helbig, W., *J. Am. Chem. Soc.*, **1994**, 116, 7401.
- [83] George, S. M., *Chem. Rev.*, **2010**, 110, 111.
- [84] Martinez, A., Prieto, G., *Catal. Commun.*, **2007**, 8, 1479.
- [85] Cui, H., Zayat, M., Levy, D., *Chem. Mater.*, **2005**, 17, 5562.
- [86] Wang, C.-C., Ying, J. Y., *Chem. Mater.*, **1999**, 11, 3113.
- [87] Goldstein J., Newbury D.E., Joy D.C., Lyman C.E., Echlin P., Lifshin E., Sawyer L.C., Michael J.R., *Scanning Electron Microscopy and X-Ray Microanalysis* 3rd Edition, Kluwer Academic Publishers, New York, **2003**.
- [88] Tosheva L., Valtchev V. P., *Chem. Mater.*, **2005**; 17, 2494.
- [89] Castillejos E., Debouttire P. J., Roiban L., Solhy A., Martinez V., Kihn Y., Ersen O., Philippot K., Chaudret B., Serp P., *Angew. Chem. Int. Ed.*, **2009**, 48, 2529.
- [90] Çelik D., Karahan S., Zahmakıran M., Özkar S., *Int. J. Hydrogen Energy*, **2012**, 37, 5143.

- [91] Akbayrak S., Gençtürk S., Morkan İ., Özkar S., *RSC Advances*, **2014**, 4, 13742.
- [92] Akbayrak S., Tonbul Y., Özkar S., *Appl. Catal. B: Environ.*, **2016**, 198, 162–170.
- [93] Yamaguchi K., Mori K., Mizugaki T., Ebitani K., Kaneda K., *J. Am. Chem. Soc.*, **2000**, 122, 7144
- [94] Mori K., Miyawaki K., Yamashita H., *ACS Catal.*, **2016**, 6, 3128.
- [95] Zahmakıran, M., Özkar, S., *Langmuir*, **2009**, 25, 2667
- [96] Rakap, M., Özkar, S., *Appl. Catal. B: Environ.*, **2009**, 91, 21.
- [97] Kaneda K., Mizugaki T., *Energy Environ. Sci.*, **2009**, 2, 655.
- [98] Choi D., Marra K., Kumta P. N., *Materials Research Bulletin*, **2004**, 39, 417.
- [99] Weng W., Baptista J. L., *J. Mater. Sci. Mater. Med.*, **1998**, 9, 159.
- [100] Rakap M., Özkar S., *Catal. Today*, **2012**, 183, 17.
- [101] Baer Y., Heden P. F., Hedman J., Klasson M., Nordling C., Siegbahn K., *Phys Scripta*, **1970**, 1, 55.
- [102] Mevellec V., Nowicki A., Roucoux A., Dujardin C., Granger P., Payen E., Philippot K., *New J. Chem.*, **2006**, 30, 1214.
- [103] Storck S., Bretinger H., Maier W.F., *Appl. Catal. A: Gen.*, **1998**, 174, 137.
- [104] Özkar S., Finke R. G., *Coord. Chem. Rev.*, **2004**, 248, 135.
- [105] Özkar S., Finke R.G., *Langmuir*, **2003**, 19, 6247.
- [106] Metin Ö., Özkar S., *Int. J. Hydrogen Energy*, **2007**, 32, 1707.
- [107] Çalışkan S., Zahmakıran M., Durap F., Özkar S., *Dalt. Trans*, **2012**, 41, 4976.
- [108] Watzky M. A., Finke R. G., *J. Am. Chem. Soc.*, **1997**, 119, 10382.
- [109] Laidler K. J., In *Chemical kinetics*, 3rd ed.; Harper & Row Publishers: New York, **1987**.
- [110] Eyring H., *J. Chem. Phys.*, **1935**, 3, 107.
- [111] Clark T. J., Whittell G. R., Manners I., *Inorg. Chem.*, **2007**, 46, 7522.
- [112] Jaska C. A., Clark T. J., *J. Am. Chem. Soc.*, **2005**, 127, 5116.

- [113] Hornstein B. J., Aiken J.D., Finke R. G., *Inorg. Chem.*, **2002**, 41, 1625.
- [114] Vargaftik M. N., Zargorodnikov V. P., Stolarov I. P, Moiseev I. I, Kochubey D. I, Likholobov V. A., Chuvilin A. L., Zamaraev K.I., *J. Mol. Catal.*, **1989**, 53, 315.
- [115] Polshettiwar V., Len C., Fihri A., *Coord. Chem. Rev.*, **2009**, 253, 2599.
- [116] Richmond M. K., Scott S. L., Alper H., *J. Am. Chem. Soc.*, **2001**, 123, 10521.
- [117] Baer Y., Heden P.F., Hedman J., Klasson M., Nordling C., Siegbahn K., *Phys. Scripta*, **1970**, 1,55.
- [118] Barr T. L., *J. Phys. Chem.* **1978**, 82, 1801.
- [119] Peuckert M., *Surf. Sci.*, **1984**, 141, 500.
- [120] Watzky M. A., Finke R. G., *J. Am. Chem. Soc.*, **1997**, 119, 10382.
- [121] Widegren J.A., Aiken J. D., Özkar S., Finke R.G., *Chem. Mater.*, 2001, 13, 312.
- [122] Watzky M. A., Finke R. G., *Chem. Mater.*, **1997**, 9, 3083.
- [123] Umpierre P. A., De Jesus E., Dupont J., *ChemCatChem*, **2011**; 3,1413.
- [124] Lewis D. J., Day T. M., MacPherson J. V., Pikramenou Z., *Chem. Commun.*, **2006**, 13, 1433–1435
- [125] Boudart M., *Chem. Rev.*, **1995**, 95, 661.
- [126] Shmidt F. K., Nindakova L. O., Shainyan B. A., Saraev V. V., Chipanina N. N., Umanetz V. A., *J. Mol. Catal. A: Chem.*, **2005**, 235, 161.
- [127] Steinhoff B. A., Fix S. R., Stahl S. S., *J. Am. Chem. Soc.*, **2002**, 124, 766.
- [128] Sanchez-Delgado R. A., Andriollo A., Puga J., Martin G., *Inorg. Chem.*, **1987**, 26, 1867–1870.
- [129] Zhou X., Xu W., Liu G., Panda D., Chen P., *J. Am. Chem. Soc.*, **2010**, 132, 138.
- [130] M. A. Watzky, E. E. Finney, R. G. Finke, *J. Am. Chem. Soc.* 130 (2008) 11959–11969.
- [131] Notheisz F., Zsigmond,Á. Bartók M., Szegletes Z., Smith G. V., *App. Catal. A: Gen.*, **1994**, 120, 105.
- [132] Madon R. J., Boudart M., *Ind. Eng. Chem. Fundamen.*, **1982**, 21, 438.

- [133] Yu J., Bai H., Wang J., Li Z., Jiao C., Liu Q., Zhang M., Liu L., *New J. Chem.*, **2013**, 37, 366.
- [134] Lin S.J., Hong T.N., Tung J.Y., Chen J.H., *Inorg. Chem.*, **1997**, 36, 3886.
- [135] Deacon G.B., Phillips R.J., *Coord. Chem. Rev.*, **1980**, 33, 227.
- [136] Kakade B.A., Sahoo S., Halligudi S.B., Pillai V.K., *J. Phys. Chem. C*, **2008**, 112, 13317.
- [137] Sieh Z.W., Gronsky R., Bell A.T., *J. Catal.* **1997**, 170, 62.
- [138] Ciftci A., Eren S., Ligthart D.A.J.M., Hensen E.J.M., *ChemCatChem.*, **2014**, 6, 1260.
- [139] Bard A.J., Parsons R., Jordan J., *Standard Potentials in Aqueous Solution*, IUPAC, Marcel Dekker Inc., New York, **1985**.
- [140] Cargnello M., Doan-Nguyen V., Gordon T., Diaz R., Stach E., Gorte R. Fornasiero, P., Murray C., *Science*, **2013**, 341, 771.
- [141] Sun C., Li H., Chen L., *Energy Environ. Sci.*, **2012**, 5, 8475.
- [142] Zhang Z., Lu Z.-H., Tan H., Chen X., Yao Q., *J. Mater. Chem. A*, **2015**, 3, 23520.
- [143] Hosokawa S., Fujinami Y., Kanai H., *J. Mol. Catal. A:Chem.*, **2005**, 240, 49.
- [144] Sun C., Li H., Chen L., *J. Phys. Chem. Solids*, **2007**, 68, 1785.
- [145] Sun C., Chen L., *Eur. J. Inorg. Chem.* **2009**, 26, 3883.
- [146] Suppino R. S., Landers R., Cobo A. J. G., *Appl. Catal. A*, **2013**, 452, 9.
- [147] Hosokawa S., Nogawa S., Taniguchi M., Utani K., Kanai H., Imamura S., *Appl. Catal. A*, **2005**, 288, 67.
- [148] Hosokawa S., Kanai H., Utani K., Taniguchi Y., Saito Y., Imamura S., *Appl. Catal. B*, **2003**, 45, 181.
- [149] Akbayrak S., Taneroğlu O., Özkar S., *New J. Chem.*, **2017**, 41, 6546.
- [150] Tonbul Y., Akbayrak S., Özkar S., *Int. J. Hydrogen Energy*, **2016**, 41, 11154.
- [151] Akbayrak S., Tonbul Y., Özkar S., *Dalt. Trans.*, **2016**, 45, 10969.
- [152] Akbayrak S., Tonbul Y., Özkar S., *Appl. Catal. B: Environ*, **2017**, 206, 384.

- [153] Sun C., Sun J., Xiao G., Zhang H., Qiu X., Li H., Chen L., *J. Phys. Chem. B*, **2006**, 110, 13445.
- [154] Sevcikova K., Szabova L., Kettner M., Homola P., Tsud N., Fabris S., Matolin V., Nehasil V., *J. Phys. Chem. C*, **2016**, 120, 5468.
- [155] Derevyannikova E. A., Kardash T. Y., Kibis L. S., Slavinskaya E. M., Svetlichnyi V. A., Stonkus O. A., Ivanova A. S., Boronin A. I., *Phys. Chem. Chem. Phys.*, **2017**, 19, 31883.
- [156] Z.W. Sieh, R. Gronsky, A.T. Bell, *J. Catal.* 170 (1997) 62-74.
- [157] Lee S.S., Song W., Cho M., Puppala H.L., Nguyen P., Zhu H., Segatori L., Colvin V.L., *ACS Nano*, **2013**, 7, 9693.
- [158] Özhava D., Özkar S., *Appl. Catal. B: Environ.*, **2018**, 237, 1012.
- [159] Özhava D., Özkar S., *Int. J. Hydrogen Energy*, **2015**, 40, 10491.
- [160] Özhava D., Özkar S., *Appl. Catal. B: Environ.*, **2016**, 181, 716.
- [161] Özhava D., Özkar S., *Mol. Catal.*, **2017**, 439, 50.
- [162] Xu Q, Chandra M., *J. Power Sources*, **2006**, 163, 364.
- [163] Yang X, Cheng F, Tao Z, Chen J., *J. Power Sources*, **2011**, 196, 2785.

CIRRICULUM VITAE

PERSONAL INFORMATION

Surname, Name: Özhava Derya

Nationality: Turkish

Date and Place of Birth: 8 June 1986, Çorlu

Marital Status:Married

e-mail: cderya@metu.edu.tr

EDUCATION

2012- present.

- PhD in Inorganic Chemistry(CGPA : 3.86 / 4.00)
- Department of Chemistry, Middle East Technical University
- Thesis Title: Preparation and Characterization of Transition Metal(0) Nanoparticles Stabilized on Nanocrystalline Supporting Materials; The Catalytic Use in Hydrogen Generation From The Methanolysis of Ammonia Borane
- Supervisor: Prof. Dr. Saim ÖZKAR

September 2010- February 2012

- **M.S. in Inorganic Chemistry** (CGPA : 4.00 / 4.00)
- Department of Chemistry, Middle East Technical University
- Title of Thesis: Rhodium(0) Nanoparticles Supported On Hydroxyapatite: Preparation, Characterization And Catalytic Use In Hydrogen Generation From Hydrolysis Of Hydrazine Borane And Ammonia Borane
- Supervisor: Prof. Dr. Saim ÖZKAR

September 2004-June 2009

- **BSc. in Chemistry CGPA: 3.72/4.00**
- Department of Chemistry, Abant Izzet Baysal University

- High Honour Student

Work Experience:

- 2009-present : Research Assistant in Middle East Technical University, Department of Chemistry

Successes and Awards

- High Honor Student in Department of Chemistry, Bachelor Degree, Abant Izzet Baysal University, 2009.
- 3rd Highest Ranking Student in Faculty of Science, Bachelor Degree, Abant Izzet Baysal University, 2009.
- Highest Ranking Student in Department of Chemistry, Graduate Courses Performance Award, Master of Science, Middle East Technical University, 2012.
- TUBITAK National Scholarship Programme for Master of Science, Scholar.
- TUBITAK National Scholarship Programme for PhD, Scholar.
- 29. National Chemistry Congress, 2017 / Turkish Chemical Society Prof. Dr. Ali Rıza Berkem The Second Best Poster Award, Ankara.

Publications

1. Mehmet Zahmakıran, Tuğçe Ayvalı, Serdar Akbayrak, Salim Çalışkan, Derya Çelik, Saim Ozkar, Zeolite framework stabilized nickel(0) nanoparticles: Active and long-lived catalyst for hydrogen generation from the hydrolysis of ammonia-borane and sodium borohydride, *Catalysis Today*, 170 (2011) 76-84.
2. Izzet Amour Morkan, Derya Çelik, Ayşe Uztetik Morkan, Kutalmış Güven, Synthesis, crystal structure, spectroscopic investigations, thermal behavior and DFT calculations of pentacarbonyl(2-methylpyrazine)chromium(0), *Spectrochimica Acta Part A* 93 (2012) 47-52.
3. Derya Çelik, Senem Karahan, Mehmet Zahmakıran, Saim Özkar, Hydrogen generation from the hydrolysis of hydrazineborane catalyzed by rhodium(0) nanoparticles supported on hydroxyapatite, *International Journal of Hydrogen Energy*, 37 (2012) 5143-51.

4. Derya Özhava, Nihan Z. Kılıçaslan, Saim Özkar, PVP-stabilized Nickel(0) Nanoparticles as Catalyst in Hydrogen Generation from the Methanolysis of Hydrazine Borane or Ammonia Borane, Applied Catalysis B: Environmental, 162 (2015) 573-82 (DOI: 10.1016/j.apcatb.2014.07.033.)
5. Derya Özhava, Ahmet M. Önal, Saim Özkar, Electrochemical Behavior of Hydrazine Borane in Methanol Solution, Journal of Electrochemical Society, 161 (2014) F1171-75 (DOI: 10.1149/2.0211412jes.)
6. Derya Özhava, Saim Özkar, Rhodium(0) nanoparticles supported on hydroxyapatite nanospheres and further stabilized by dihydrogen phosphate ion: A highly active catalyst in hydrogen generation from the methanolysis of ammonia borane. International Journal of Hydrogen Energy, 40 (2015) 10491-10501.
7. Derya Özhava, Saim Özkar, Rhodium(0) nanoparticles supported on nanosilica: Highly active and long lived catalyst in hydrogen generation from the methanolysis of ammonia borane. Applied Catalysis B: Environmental, 181 (2016) 716-726.
8. Derya Özhava, Saim Özkar, Nanoalumina supported rhodium(0) nanoparticles as catalyst in hydrogen generation from the methanolysis of ammonia borane, Molecular Catalysis, 439 (2017) 50-59.
9. Derya Özhava, Saim Özkar, Nanoceria supported rhodium(0) nanoparticles as catalyst in hydrogen generation from the methanolysis of ammonia borane, Applied Catalysis B: Environmental, 237 (2018) 1012-1020.

Conferences Attended

- 24th National Chemistry Congress, 29 June-02 July 2010/ Zonguldak, Turkey / poster.
- 3rd National Inorganic Chemistry Congress, 19-22 May 2011 /Çanakkale, Turkey/ poster.
- 5th National Catalysis Congress, 23-26 April 2014 / Adana, Turkey/ poster.

- International Conference on Green Chemistry and Sustainable Engineering, 29-31 July 2014 / Barcelona, Spain / oral presentation.
- 29. National Chemistry Congress, 10-14 September 2017 / Ankara, Turkey / poster